ICFO - Institute of Photonic Sciences

PhD thesis

Levitodynamics on-a-chip: from planar Paul traps to near-field optical nanocavities

Author:
Irene Alda

Supervisor:
Prof. Romain Quidant
Co-supervisor:
Dr. Piergiacomo Z.G. Fonseca

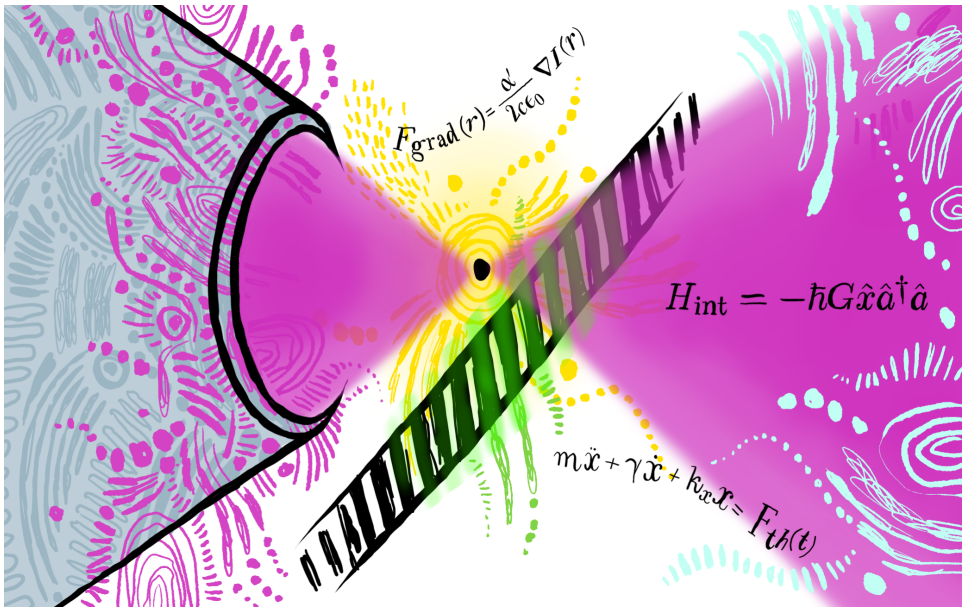

Claudia Sahuquillo, artist.

UNIVERSITAT POLITÈCNICA DE CATALUNYA BARCELONATECH

Levitodynamics on-a-chip: from planar Paul traps to near-field optical nanocavities

Irene Alda

Acknowledgements

"Thank you, thank you, thank you."

The very very first, I would like to thank my mom, Paz, for her e-t-e-r-n-a-l stubbornness. From the very first day and on, she said "Irene, have you started writing your thesis?". And, although she does get on my nerves; she's a constant to reminder to persevere in everything I do. Then, I'd like to thank my dad, Javier. He was the one who told me about ICFO, so, I would obviously not be here right now without him. Muchísimas gracias a los dos, por siempre estar ahí. Os quiero muchísimo. And of course, to Romain, my PhD advisor, for providing me the opportunity to be part of the PNO team, and to deepen and mature as both a scientist and a person during these years.

A big big thank you goes to the Optomechanics gang :) Feeling part of a team and being able to discuss with all of you has made all the difference. Giacomo, I'll always be grateful for passing on to me your good lab organization skills, and your constant patience in the writing of this thesis. You brought out all the confidence and tidiness within me (I really admire you for this). I've enjoyed very much to work side by side with you. Nadine, vielen Dank für dein Lächeln und deine Liebe und Unterstützung, immer. Und natürlich danke dafür, dass du mich nicht alleine gelassen hast beim "allein-reden-im-Büro". A mis compañeros de horas y horas de laboratorio a lo largo de estos años: Pau, Fran, Marc, Andrés (¡Buenos días Andrés!) y Pascal. Gracias por la música, por los chistes, por las conversaciones más o menos serias, y por vuestra predisposición a echarme siempre un cable. Jan, gracias por tu input en el experimento y por siempre aportar positividad al proyecto. Of course a huge thank you goes to Johann, thank you for sharing with me all your clean room expertise and good experimental tips. Another big big thank you goes to everyone who has come and gone in the experiment: Vincenzo, Raúl, and Andreas. Mil gracias a Marcos, Alex y a Jordi, por vuestros múltiples comentarios y ayuda para conseguir una simulación fiable en COMSOL. I, finalment, el Gerard. Gràcies pel teu afecte, per creure en mi quan jo no podia. I, per descomptat, per explicar-me tots el meus dubtes de matemàtiques, electrònica, i ajudar-me sempre. T'estimo.

I also feel very grateful for all the ICFO community or "ICFO family". Starting with the members of PNO that I've met during this time: I've learned and benefited from you very much (special thank you to Ignacio for making piranha and HF for me whenever I asked). And then, from Xavi in the mechanical workshop for always making the extra effort so I would get pieces when I really needed them, to the HR team who have made all the

paperwork always very easy. I'd also like to thank the clean room staff and technicians: Luis, Javi, and Johann. You've always been there for me to talk about all my clean room related questions and other too. Also, thank you to the electronic workshop team, for being patient and always helping me to find solutions. And although it could seem like small thing, to everyone that always offered a kind smile or a sincere "how is it going?".

To my ICFOnian friends, I'm still astounded by the amount of people I've met during my stay at ICFO! A huge and enormous hug goes to Lisa, for always being there with a smile each morning, making me vegan "no bullshit snickers" or everyday meals when things were difficult. I've loved having you next door. Lots of gratitude too to my former flatmates: Kavitha and Pamina. Thank you for the "at home" support and for sharing your PhD experience with me: it's always been comforting and caring to hear about others going through the same ups and downs in their own way. Sandra, mil gracias por haber estado siempre tan atenta y amable. La aventura de la docencia con la FPU no hubiese sido lo mismo sin ti. Y, Marcos, gracias por todo tu apoyo y las discusiones sobre cristales fotónicos y levitación. And of course, also a big thanks to all the ICFO yogis: I've had such a wonderful time sharing yoga with you!

Ahora, salgamos de la burbuja de ICFO. Primero, quiero dar las gracias a mi familia, que siempre me ha apoyado y se ha mostrado atenta conmigo. A mis amigos madrileños, gracias por haber estado ahí siempre para hablar, sentirse escuchado es TAN importante. También quiero agradecer a mi familia-yogi en Barcelona que siempre me ha transmitido fuerza, buen rollo y cariño: a mi vivea team, a mi queridísima glow gang ("Irene you've got this!") y a la Shanti-vida fam. También al grupo de Castelldefels Outdoor y al entrenador, José Miguel, por animarme siempre. Y también a las nuevas amistades que han brotado en Barcelona. A Eira, gracias por todas las aventuras, y sobre todo, por hacerme salir de la silla de escribir para ir a yoga contigo. Claudia, mil gracias por crear la mejor portada que podría haber soñado, ¡te admiro muchísimo! Y, por supuesto, a todo el grupo "garriguenc".

Oh, we are getting the end! My very last thank you goes to my dear yoga practice, which has always been there for me whether it was to stretch my back from long hours on the experiment or just feel grounded, confident, and empowered when frustration crept in.

And that's all folks! Now... let's get down to business and do some science ;)

Abstract

The field of levitation optomechanics—or levitodynamics—studies the manipulation and control of small trapped objects in an isolated environment, providing a gateway to answer fundamental questions in physics and expanding the range of applications at the nanoscale.

Levitation of particles can be achieved through different tools and techniques such as Paul traps and optical tweezers. Paul traps are created by alternating electric fields to levitate charged particles, while optical traps are based on optical forces that confine and manipulate nano-objects with high polarizability and low absorption. Both have the potential to be reduced to on-a-chip systems, enabling the miniaturization of the experiment, its interface with other photonic devices, and the expansion of trapping tools to on-a-chip technologies. In particular, a nanocavity coupled with a levitated particle is a promising platform to attain higher per-photon sensitivities than far-field detection schemes. The further study of on-a-chip levitated optomechanics systems will allow for new applications that enable sub-wavelength control and near-field detection in vacuum conditions.

In this thesis, we describe our work with two on-a-chip levitodynamics experiments. Firstly, we have designed and built a planar Paul trap to levitate nanoparticles. This integrated device allows to manipulate and interrogate the trapped specimen, even over long periods of time. We optimized the geometry of the trap to a confinement of $\sim 4\,\mu$m in each direction. This on-a-chip levitation tool has potential to become a clean loading mechanism to trap particles in vacuum, avoiding current techniques that are unsuitable for contamination-sensitive experiments. Secondly, we have also designed, fabricated and tested a 1D photonic crystal nanocavity suspended on a silicon nitride membrane to study near-field levitodynamics. We have approached a levitated nanoparticle by an optical tweezer to the near-field of the nanocavity and measured the dynamics of the nanoparticle through the nanocavity. From the output signal of the nanocavity, we have estimated the single-photon optomechanical strength g_0 along each axis. We have also characterized the thermal dynamics of the nanocavity. The power circulating inside the cavity increases the temperature of the device, inducing rich and tunable behavior in the transmission, such as bistability and self-induced oscillations. Control over these thermal effects is fundamental to create all-optical integrated circuits. This technology, exploited alongside the miniaturization of Paul traps and near-field schemes, could enable on-a-chip levitodynamical devices that are able to trap, manipulate, and detect nano-objects with unprecedented precision.

Resumen

El campo de la optomecánica de levitación—o levitodinámica—estudia la manipulación y el control de objetos pequeños atrapados, proporcionando un entorno aislado, para dar respuesta a preguntas fundamentales en física y para expandir las aplicaciones nanotecnológicas.

Se puede levitar partículas mediante diferentes técnicas, como por ejemplo, las trampas de Paul y las pinzas ópticas. Las trampas de Paul se generan mediante campos eléctricos variables en el tiempo y permiten levitar partículas cargadas. Por otro lado, las trampas ópticas se basan en fuerzas ópticas, que confinan nano-objetos con alta polarizabilidad y baja absorción. Ambas opciones ofrecen la posibilidad de convertirse en un sistema integrado: minituarizando el experimento, facilitando su interacción con otros sistemas fotónicos y expandiendo así las herramientas de levitación hacia una tecnología "on-a-chip". En particular, una nanocavidad acoplada a una nanopartícula levitada es una plataforma prometedora para alcanzar una alta sensitividad por fotón en comparación con técnicas de detección de campo lejano. El estudio de sistemas optomecánicos levitados permitirá el desarrollo de nuevas aplicaciones, control sub-λ y detección de campo cercano.

En esta tesis, describimos dos sistemas levitodinámicos "on-a-chip". Primero, hemos diseñado y construido una trampa de Paul plana para hacer levitar nanopartículas. Este sistema integrado permite manipular el espécimen atrapado durante largos periodos de tiempo. Hemos optimizado la geometría de la trampa hasta un confinamiento de $\sim 4\,\mu$m en cada dirección. Esta herramienta de levitación "on-a-chip" permitirá un procedimiento limpio para cargar partículas a una trampa óptica directamente en vacío, evitando técnicas inapropiadas para experimentos sensibles a contaminación. Segundo, hemos diseñado, fabricado y caracterizado una nanocavidad de cristal fotónico 1D en una membrana suspendida de nitruro de silicio para estudiar la levitodinámica de campo cercano. Hemos acercado una partícula levitada ópticamente al campo cercano de la nanocavidad y, a través de ella, hemos medido la dinámica de la nanopartícula. Mediante la señal de transmisión de la nanocavidad, hemos estimado la fuerza optomecánica por fotón g_0 para cada eje de movimiento. También hemos caracterizado el comportamiento térmico de la nanocavidad. La potencia que circula por ella aumenta su temperatura, dando lugar a biestabilidad y oscilaciones autoinducidas en su transmisión, elementos claves para crear circuitos de óptica integrada. Esta tecnología, junto a la minituarización de las trampas de Paul y sistemas de campo cercano darán lugar a sistemas levitodinámicos "on-a-chip" capaces de atrapar, manipular y detectar nano-objetos con una precisión sin precedentes.

Contents

Chapter 1

Introduction

Galileo was one of the first to propose that the laws of physics could be written in the language of mathematics. Through a series of experiments and a telescope of his own invention, he initiated the systematic study of the dynamics of free bodies. Today, he is sometimes referred to as the father of the scientific method.

The scientists that came after him continued to investigate the motion and dynamics of objects: from the gravitation of celestial bodies [1, 2], the shape of comets approaching the Sun [1], and the acceleration of objects in free fall [2], to the interaction of light with matter [3]. In the last decades, the interest in the dynamics of free bodies has been extended to the microscopic world: we've gone from being struck by a falling apple to controlling the motion [4, 5] and free fall of a levitated nanoparticle [6]. Thanks to advances in nanotechnology and computation, we are now able to precisely study physics at the micro- and nanoscale.

One of the demands in current research are tools to accurately and non-invasively manipulate objects at the nanolevel. Optical tweezers are a well-rounded option; they were pioneered by Ashkin [7], who was awarded the Nobel prize in Physics in 2018. An optical tweezer is created when a laser beam is tightly focused, to the extent that it can optically hold and move small objects. Optical levitation provides excellent isolation of the object from the environment, and precise control over it. Aside from optics [8] and atomic physics [9, 10], optical tweezers are very important instruments in life sciences [11]. They have allowed us to understand, for example, the dynamics of motor molecules [12], the motion of ribosomes during part of the process to generate new proteins [13], protein folding [14], and curvature-dependent interactions of a single DNA molecule [15]. Conventional optical tweezers have these manipulation capabilities for micrometer sized objects [16] and

neutral atoms [17, 18], but are inadequate for 1–100 nm size objects, mainly due to the strong decrease of the polarizability when the particle's radius is reduced; also, some particle materials have high absorption and suffer from heating problems [19]. This limits the choice of the nanoparticle's material, and typically only silica is used, since it has very low absorption at the common near-infrared trapping wavelengths and it is commercially available.

Two possible alternatives to the standard optical tweezers are Paul traps and near-field optical trapping schemes. Paul traps, whose invention was also awarded with the Nobel prize in 1989 [20], are capable of levitating charged objects within a large range of charge to mass ratios, by using varying electric fields. Unlike optical tweezers, they do not heat the trapped object and thus they broaden the range of materials of the levitated object. At the same time, near-field schemes—although so far limited to a liquid environment—offer a different alternative to optical tweezers. Near-field traps have been demonstrated with nanoplasmonics [21] and silicon photonics [22]. These approaches allow for stable trapping from the single protein level [23] up to nanoparticles of a few tens of nanometers [24, 25, 26], and even 3D manipulation of the trapped object [27]. Current efforts are being made to adapt this technology to vacuum to further expand the study of levitated particles, a fast growing field commonly referred to as levitation optomechanics or levitodynamics.

1.1 The growing field of levitodynamics

In the last decade, the study of levitated nanoparticles in vacuum has produced several new techniques that have allowed, for example, to accurately measure the mass of a levitated object [28] and control its charge [29]. We can now manipulate the trapped object with optical fiber traps [30], control its dynamics [31], and study particles with internal degrees of freedom, which—when coupled to their center-of-mass motion—offer a clear path towards the study of quantum phenomena at the macroscale [32]. Progress in the study of levitated particles with internal degrees of freedom has found the most success in experiments involving Paul traps [33, 34]. At the same time, optical traps have demonstrated attonewton force sensitivities [35], and even photon recoil detection [36]. Precisely in this regard as force and acceleration sensors, the recently approved European project IQLev (Inertial Sensing based on Quantum-Enhanced Levitation Systems) is aimed at developing an inertial sensing device based on levitated objects: high-performance accelerometers and gyroscopes based on optical, electrical, and magnetic levitation of microscopic and mesoscopic systems [37].

One of the ultimate goals in levitodynamics is the quantum control of the levitated object [38, 39]. To obtain this control, the first step is cooling the object's center-of-mass motion to the ground state. A common approach is the use of feedback cooling, for instance, with modulated laser beams [4, 5] or with electric fields [40, 41]. However, these schemes are still limited to a mean occupation number of the center-of-mass motion of 4 phonons [42]. A different route is to place an optical cavity around the levitated particle, enhancing the particle's interaction with light. This may provide new avenues for cooling the center-of-mass motion [43, 44, 45].

By positioning a levitated nanoparticle inside an optical cavity, we vary the optical path length of the cavity, due to a small change in the index of refraction along its propagation axis. This results in a shift of the cavity's resonance frequency ω_c, which depends on the particle's position. At the same time, the displacement of the particle is also affected by the cavity's optical field via scattering and gradient optical forces. Therefore, their dynamics are coupled, in such a way that besides monitoring the particle's displacements through the measurement of ω_c, it is also possible to optically control (cooling or heating) the oscillations of the levitated object [46]. This interaction is quantified by a fundamental parameter g_0, known as the single-photon optomechanical coupling strength, that measures the capacity of the mechanical oscillator's motion—in this case a levitated nanoparticle—to alter the optical cavity field. Several levitation optomechanics experiments have demonstrated side band cooling of the motion of levitated particles in a Fabry-Perot cavity, holding the particle in the cavity with Paul traps [47, 48] and optical tweezers [49, 50, 51]. Through a technique known as "coherent scattering", the ground state of the motion has been claimed for the first time with a levitated object [52]. This goal had been already accomplished with other optomechanical platforms in 2010 at cryogenic temperatures [53, 54, 55]. However, the high level of mechanical isolation offered by a levitated object has allowed to reach its ground state of motion directly at room temperature, and offers the chance to study quantum superposition states of massive objects [56].

Optomechanics experiments have been miniaturized in the last 15 years. Some examples of down-scaled cavities and mechanical oscillators include reflective micro-mechanical membranes [57], microtoroids [58], disks [59, 60], spheres [61], superconducting microwave circuits [62], and photonic crystal cavities [63]. The trend of aiming for lower masses and dimensions is not a mere coincidence: it is because of how the mass of the mechanical oscillator, and the cavity's mode volume, relate to the strength of the fundamental optomechanical interaction g_0. A size reduction of the optical cavity's mode volume V_c and its adaptation to vacuum conditions [64] would enhance the

optomechanical coupling g_0 and reduce losses in detection. Increasing g_0 allows us to obtain more information per photon from the oscillator's motion—in our case, an optically trapped particle—and from the forces that act upon it. Also, a high optical $Q = \frac{\omega_c}{\kappa}$ factor, equivalent to a small linewidth κ of the optical oscillator, makes the system more sensitive to variations in frequency ω_c. One option to achieve this high Q/V_c ratio is with photonic crystal nanocavities [65], which are prime examples of the previously mentioned near-field on-a-chip schemes.

One result of reducing the cavity's dimensions and working with micro- and nanocavities is the confinement of high optical powers into small volumes, which makes these devices susceptible to thermally induced nonlinearities. The system is forced to dissipate energy through a small surface area, giving rise to a thermal drift of the cavity resonance [66], also called thermal dispersion. More in general, recent studies have demonstrated that the most common mechanisms that affect micro- and nanocavities' resonance frequencies are: the nonlinear thermo-optic effect, the optical Kerr effect, two photon absorption, thermal expansion, and the thermo-mechanical effect [67]. They all affect the resonance of the cavity ω_c by either modifying the geometry of the cavity's structure or the refractive index of the cavity's material. In particular, the thermo-optic effect—which is typically dominant in micro- and nanocavities—relates a change in refractive index to a change in temperature.

Two behaviors that arise from thermal nonlinearities are bistability, which is a steady state phenomenon, and self-induced oscillations, which present time varying dynamics; both of them depend on the input power and wavelength. Optical bistability shows a hysteretic cavity transmission response with a high and low output state. Often, this characteristic is investigated in devices whose design is optimized such that bistability becomes visible at the lowest possible input powers [68, 69, 70]. This is relevant in the field of integrated photonic circuits to create energy efficient devices [71]. Self-induced oscillations are produced when two physical mechanisms shift the resonance of the cavity in opposite directions at different timescales. It has been observed experimentally in suspended silicon dioxide microspheres [72], silicon microdisks [73], silicon micro-ring structures [74] and silicon nanobeams [75]; their oscillation frequency depends on the material and geometry of the device. In silicon, the main drivers of these oscillations are a slow thermo-optic effect and a fast two photon absorption [76]. Alongside with bistability, these nonlinear effects can be used for self-pulsing [77], lasing [78, 79], and could enable optical analogs of electronic components such as optical switches or even more complex integrated photonic circuits.

Besides silicon, a typical platform for integrated photonics is silicon nitride. It has low absorption, offers good optical properties that allow for high Q optical resonators [80], and can also serve as a nanomechanics system in itself [81]. When compared with silicon, silicon nitride benefits from the absence of two photon absorption at telecom wavelengths [82], which induce extra waveguide losses at a few tens of mW. Bistability and self-induced oscillations in silicon nitride have been reported for constant intensity excitation [83], where self-induced oscillations are driven by a fast thermo-optic nonlinearity and a slow thermo-mechanic effect.

Control over these thermal effects is fundamental to create all-optical integrated circuits. This technology, exploited alongside the miniaturization of Paul traps and near-field schemes, could enable on-a-chip optomechanical devices that are able to trap, manipulate, and detect nano-objects with unprecedented precision. A good candidate for on-a-chip devices is the planar Paul trap, whose lithographed electrodes are already integrated in a single plane [84, 85, 86]. Its compatibility with printed circuit board technology makes fabrication simple and convenient [87, 88, 89, 90]. Besides a good trap confinement, the planar geometry allows for easy optical access and can be used to develop clean and precise loading techniques for optical traps in vacuum, improving the conditions for "on-a-chip" near-field devices for levitodynamics.

1.2 Thesis outline

In this thesis, we've worked with two different levitation-based platforms to explore new, compact, and integrated on-a-chip solutions. First, a planar Paul trap to levitate and control a levitated object; and second, an optical tweezer to trap a nanoparticle and bring it in close vicinity of a photonic crystal nanocavity, where it interacts with the near-field.

We will show the manipulation of 100 nm charged polystyrene particles with the planar Paul trap in air. It represents one of the first uses of Paul traps in levitodynamics, where we optimized the design to obtain a better confinement for the trapped object [91]. We also describe the details and techniques to optomechanically couple a levitated nanoparticle to an on-a-chip 1D Si_3N_4 photonic crystal nanocavity. We have designed, built, and tested this system experimentally, measuring its optomechanical coupling coefficient and showing the limitations of the technique. For high enough input powers, the nanocavity exhibits nonlinear thermal effects such as optical bistability and self-induced oscillations.

I have divided the thesis into 8 chapters and appendices:

1. **Chapter 1**: Introduction.
2. **Chapter 2**: Fundamentals of particle trapping with optical tweezers and Paul traps, and cavity optomechanics.
3. **Chapter 3**: Fundamentals of photonic crystals and thermal behavior in micro- and nano-cavities.
4. **Chapter 4**: Demonstration of the planar Paul trap experiment, which includes the experimental setup, design optimization, and published results [91].
5. **Chapter 5**: Description of the design, fabrication, and characterization of the photonic crystal nanocavities, along with the experimental setup to couple light into them and to trap the nanoparticle optically.
6. **Chapter 6**: Characterization of the thermal dynamics of the nanocavities. We show bistability and self-induced oscillations in the nanocavity's transmission ouput.
7. **Chapter 7**: Demonstration of a near-field on-a-chip levitodynamics experiment with two photonic crystal cavity designs and two measurement techniques. It also includes two proof-of-concept experiments where we read out the nanoparticle's motion through a fiber tip and a nanotaper.
8. **Chapter 8**: Conclusions and outlook.
9. **Declaration of contributions.**
10. **Appendix**:
    - Damage threshold of nanocavities.
    - Further bistabiliy measurements of the air mode nanocavity.
    - MATLAB code to draw nanocavities for electron beam lithography and to convert them into an .asc file.

Chapter 2

Particle levitation and optomechanics

In this chapter we present the fundamental concepts and the theoretical description for the two tools we use for nanoparticle levitation: an optical tweezer and a planar Paul trap. The optical tweezer allows us to bring a levitated nanoparticle into the near-field of a photonic cavity, through which we detect the nanoparticle's motion (see chapter 7). The other levitation technique, the Paul trap, can trap and manipulate small charged nanoparticles for long periods of time (see chapter 4).

In the following, we start with a description of the optical tweezer and the Paul trap. We continue by explaining the basics of optical cavities and mechanical resonators, and the optomechanical interaction between them mediated by optical forces.

2.1 Optical Tweezers

One of the key components of our experiment is the optical tweezer, that we use to trap silica nanoparticles. The main goal of this section is to describe the dynamics of such a levitated dielectric nanoparticle.

Optical tweezers are created by tightly focusing a laser beam. The nanoparticle is trapped at the focus by a 3D optical gradient force. This force may be attractive or repelling depending on the relative index of refraction between the particle and its surrounding medium. There are three different approaches to describe the trapping mechanism and the light-nanoparticle interaction, depending on the ratio between the size of the trapped object and the wavelength of the trapping beam:

1. Rayleigh scattering: the particle radius r is significantly smaller than the wavelength λ: $r \leq \frac{\lambda}{2\pi}$.

2. Ray optics: for particle's r is much greater than λ.

3. Mie theory: the particle's size is arbitrary, and hence, is the most general case.

We will restrict ourselves to the first case, Rayleigh scattering, because our nanoparticle's size, $r = 115$ nm, satisfies $r \leq \frac{\lambda}{2\pi}$, where $\lambda = 1064$ nm. Further reading on different tweezer regimes can be found on [92]. Hereafter, we will consider the nanoparticle as a point dipole at a position $\boldsymbol{r_0}$, polarized by an electric field $\boldsymbol{E}(\boldsymbol{r})$ that propagates along the z axis as shown in Fig. 2.1. If we use the Gaussian beam approximation and cylindrical coordinates, the field can be described as:

$$\boldsymbol{E}(\boldsymbol{r}) = E_0 \sqrt{\frac{w_0}{w(z)}} e^{-\frac{\rho^2}{w^2(z)}} e^{-i\phi(\rho,z)} \hat{\boldsymbol{e}}_x, \tag{2.1}$$

where E_0 is the electric field's amplitude, $w(z)$ is the beam width and describes how the Gaussian width evolves along the propagation direction z that reaches a minimum value of w_0. $\phi(\rho, z)$ is related to the local propagation wavevector $\phi(\rho, z) = \frac{2\pi}{\lambda} \frac{\rho^2}{2R(z)} + k_z z$, where $R(z)$ is the radius of curvature of the spherical wavefront that accompanies the beam. This expression of the electric field is exemplified with a linear polarization along the x axis given by the unitary vector $\hat{\boldsymbol{e}}_x$.

The electric field in equation (2.1) induces a dipole moment $\boldsymbol{p} = \alpha(\omega)\boldsymbol{E}(\boldsymbol{r_0})$ to the particle, where $\alpha(\omega)$ is the polarizability of the particle for monochromatic light at frequency ω. This exerts a force to its center of mass that can be described by three terms: gradient, scattering, and spin-curl forces (the latter is related to polarization gradients and we may neglect it because it is much smaller than the first two) [92]. Therefore, the forces that the particle experiences are:

$$\boldsymbol{F}_{\text{grad}}(\boldsymbol{r}) = \frac{\alpha'}{2c\epsilon_0} \nabla I(\boldsymbol{r}), \tag{2.2}$$

$$\boldsymbol{F}_{\text{scatt}}(\boldsymbol{r}) = \frac{\alpha''}{2} I(\boldsymbol{r}) \nabla \phi(\boldsymbol{r}), \tag{2.3}$$

where c is the speed of light, α' and α'' are the real and imaginary part of the polarizability of the nanoparticle (shown below), $I(\boldsymbol{r}) = c\epsilon_0 |\boldsymbol{E}(\boldsymbol{r})|^2/2$ and $\phi(\boldsymbol{r})$ are the intensity and phase distributions at the trapping region, and ϵ_0 is the electric permittivity in vacuum.

The two forces described by equations (2.2) and (2.3) give rise to an attractive force along the three directions towards the center of the trap and to a displacement from the center of the trap along the propagation direction, respectively. Taking a first order Taylor expansion of the force, the optical gradient takes the form of Hooke's law $F_{\text{grad},x} = -k_x x$ (see Fig. 2.1), where k_x is the stiffness and x stands for any of the three spatial directions x, y, z [92].

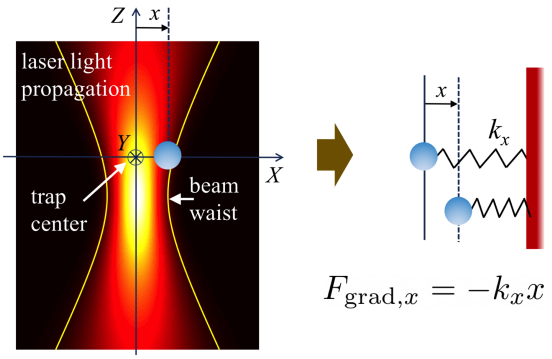

Figure 2.1: Schematics of a trapped dielectric object which is attracted to the center of the beam. The beam shown is a calculation of Gaussian beam's intensity as it propagates [93]. The trapping beam propagates along the z direction. On the right, we exemplify how the gradient force can be described, to first order approximation, by Hooke's law $F_{\text{grad},x} = -k_x x$.

For the description of the polarizability at a constant frequency ω, we consider that our particle has a volume V and relative permittivity constant ϵ_{p}:

$$\alpha_0(\omega) = 3V\epsilon_0 \frac{\epsilon_{\text{p}} - 1}{\epsilon_{\text{p}} + 2}. \tag{2.4}$$

Importantly, the particle's response depends on the external field applied and the field scattered by the particle itself. This leads us to define [94]:

$$\alpha(\omega) = \alpha_0 \left[1 - i\frac{k^3}{6\pi\epsilon_0}\alpha_0\right], \tag{2.5}$$
$$\text{where } \alpha' = \alpha_0 \text{ and } \alpha'' = -i\frac{k^3}{6\pi\epsilon_0}\alpha_0^2,$$

and where $k = \frac{2\pi}{\lambda}$ is the wavenumber.

2.1.1 Underdamped regime

With these considerations, we can describe the levitated particle with mass m as a simple harmonic oscillator both damped and forced. Damping is due to the interaction with residual gas molecules in the environment, and is modeled as a viscous drag γ. The driving is due to a stochastic force $F_{\mathrm{th}}(t)$ provided by the surrounding thermal bath. These two variables are related by the fluctuation-dissipation theorem: $F_{\mathrm{th}}(t) = \sqrt{2k_{\mathrm{B}}T\gamma} \cdot \eta(t)$, where $\eta(t)$ is a standard white noise [95]. Therefore, the equation of motion in this underdamped regime can be written as:

$$m\ddot{x} + \gamma\dot{x} + k_x x = F_{\mathrm{th}}(t). \tag{2.6}$$

If we divide (2.6) by the mass m,

$$\ddot{x} + \Gamma\dot{x} + \omega_{\mathrm{m}}^2 x = \frac{F_{\mathrm{th}}(t)}{m}, \tag{2.7}$$

where $\Gamma = \gamma/m$ is the damping rate and $\omega_{\mathrm{m}} = 2\pi f_{\mathrm{m}}$ is the mechanical oscillation frequency, related to the stiffness by $\omega_{\mathrm{m}} = \sqrt{k_x/m}$.

We can find the variance of x of equation (2.7) with the equipartition theorem [96]. However, in practice, experimental signals will include contributions from sources other than the motion of the mechanical oscillator, and these noise sources need to be filtered out. We can do so with Parseval's therorem, integrating the power spectral density (PSD) in the frequency domain [92]:

$$\langle x^2(t)\rangle = \frac{1}{2\pi}\int_{-\infty}^{\infty} S_x(\omega)\mathrm{d}\omega, \tag{2.8}$$

Hence, Fourier transforming and taking the modulus squared of equation (2.7), we obtain:

$$|\tilde{x}(\omega)|^2 = \frac{1}{m^2\left[(\omega_{\mathrm{m}}^2 - \omega^2)^2 + \Gamma^2\omega^2\right]} \mid \tilde{F}_{\mathrm{th}}(\omega) \mid^2, \tag{2.9}$$

where $\tilde{x}(\omega)$ and $\tilde{F}_{\mathrm{th}}(\omega)$ represent the position x and thermal driving F_{th} in the frequency domain. Finally, taking the expected value of equation (2.9) and applying the fluctuation-dissipation theorem[1], we obtain the PSD of a stochastically driven harmonic oscillator (see Fig. 2.2):

$$S_x(\omega) = \frac{2k_{\mathrm{B}}T\Gamma}{m\left[(\omega_{\mathrm{m}}^2 - \omega^2)^2 + \Gamma^2\omega^2\right]}. \tag{2.10}$$

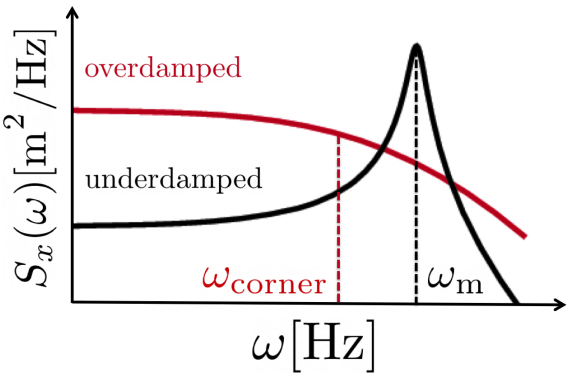

Figure 2.2: Log-log scale representation of $S_x(\omega)$ for both the overdamped and the underdamped regimes. The mechanical frequency ω_{m} and the corner frequency ω_{corner} are marked.

These expressions provide a reasonably good description of the nanoparticle's motion in an optical trap, and provide a model for analyzing and calibrating experimental data from a signal in volts to units of distance.

2.1.2 Overdamped regime

When the inertial term, proportional to acceleration, is negligible compared to viscous and trap forces, we obtain a heavily overdamped oscillator. This is the case, for instance, for trapped nanoparticles in air. Then, one may discard the second order term of the stochastic differential equation (2.7):

$$\Gamma\dot{x} + \omega_{\mathrm{m}}^2 x = \frac{F_{\mathrm{th}}(t)}{m}. \tag{2.11}$$

Thus, applying the same analysis of the previous section, we obtain a new expression for the PSD:

$$S_x(\omega) = \frac{2k_{\mathrm{B}}T\Gamma/m}{\omega_{\mathrm{m}}^4 + \Gamma^2\omega^2}. \tag{2.12}$$

It can be seen that for large Γ, equation (2.10) converges to equation (2.12). In Fig. 2.2, the overdamped PSD has two clear different regimes: at low frequencies, the ω_{m}^4 term in the denominator dominates and the spectrum is almost flat. For large $\Gamma^2\omega^2$, ω_{m}^4 is negligible and the other term dominates. The frequency at which the behavior changes is known as the corner frequency, $\omega_{\mathrm{corner}} = \frac{\omega_{\mathrm{m}}^2}{\Gamma}$, and is a fitted parameter when calibrating the motion

[1] As we've seen before, the fluctuation-dissipation theorem relates the damping with the stochastic driving force via the equipartition theorem.

in the overdamped regime. As before, the integral of the PSD is

$$\langle x^2 \rangle = \frac{1}{2\pi} \int_{-\infty}^{\infty} S(\omega) d\omega = \frac{1}{2\pi} \int_{-\infty}^{\infty} \frac{2k_{\mathrm{B}}T\Gamma/m}{\omega_{\mathrm{m}}^4 + \Gamma^2\omega^2} d\omega = \frac{k_{\mathrm{B}}T}{m\omega_{\mathrm{m}}^2}, \tag{2.13}$$

where we also recover the value expected by the equipartition theorem.

2.2 Paul traps

Optical levitation is limited to objects made of materials with low absorption, because objects made of materials with high absorption suffer from heating problems [19]. This narrows the choice of the nanoparticle's material, and typically only silica is used because it has very low absorption at the common near-infrared trapping wavelengths. Quadrupole ion traps can help fill in this gap: they can trap charged objects as long as they have a sufficiently high enough charge-to-mass ratio, and the mass is small enough for the trapping potential to compensate for gravity. A quadrupole ion trap uses dynamic electric fields to trap charged particles [20]. Sometimes they are referred to as radio frequency traps or Paul traps in honor of their inventor Wolfgang Paul, who obtained the Nobel prize in Physics in 1989 for his work [97].

The dynamic electric fields are a workaround to Earnshaw's theorem, which states that a collection of point charges cannot be maintained in a stable stationary equilibrium configuration just by the electrostatic interaction of charges. These dynamical electric fields give rise to a pseudo-potential that creates a trap.

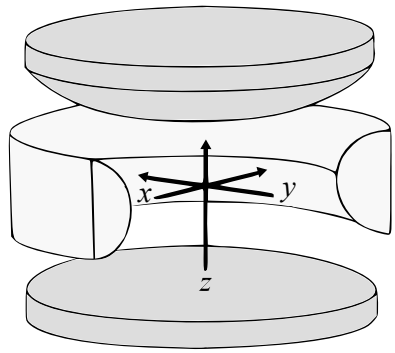

Figure 2.3: Example of a Paul trap with rotational symmetry: two end cap electrodes at the top and bottom with a ring electrode between them. Image by G. P. Conangla.

The ideal Paul trap with rotational symmetry (see Fig. 2.3) creates a

potential of the form

$$\Phi(x,y,z) = \frac{U_0 + V_0 \cos \omega t}{2d^2}(2z^2 - x^2 - y^2), \qquad d = \sqrt{\frac{r_0^2}{2} + z_0^2},$$

where z_0 and r_0 are the distances from the center to the inner (upper and lower) end caps and ring, respectively (see Fig. 2.3). For a particle of charge Q and mass m this potential gives rise to the following equations of motion, obtained by applying Newton's second law and the Lorentz force:

$$\ddot{u}_{x,y} - \frac{Q}{md^2}(U_0 + V_0 \cos \Omega t)u_{x,y} = 0, \tag{2.14}$$

$$\ddot{z} + \frac{2Q}{md^2}(U_0 + V_0 \cos \Omega t)z = 0, \tag{2.15}$$

where u_i represents the different spatial coordinates such that $i = x, y,$ or z. With the following variable changes

$$\alpha_x = \alpha_y = \frac{-4QU_0}{md^2\Omega^2}, \quad \alpha_z = \frac{8QU_0}{md^2\Omega^2},$$

and

$$q_x = q_y = \frac{2QV_0}{md^2\Omega^2}, \text{ and } \quad q_z = \frac{-4QV_0}{md^2\Omega^2} \quad \tau = \frac{\Omega}{2}t,$$

equations (2.14) and (2.15) can be written in the form of the classical Mathieu equations:

$$\frac{\partial^2 u_i}{\partial \tau^2} + (\alpha_i - 2q_i \cos 2\tau)u_i = 0. \tag{2.16}$$

By taking equation (2.16) for each axis, we obtain a set of ordinary differential equations (ODEs), which have stable solutions—particle stays trapped—under certain values of α_i and q_i. Equation (2.16) can also be expressed as

$$\frac{\partial^2 u_i}{\partial t^2} + \frac{\Omega^2}{4}\left(\alpha_i - 2q_i \cos \Omega t\right) u_i = 0. \tag{2.17}$$

In the typical case where $\mid q_i \mid \ll 1$ and $\mid \alpha_i \mid \ll 1$, the first order solution to equation (2.17) is [98]:

$$u_i(t) = K_i \cos\left(\omega_i t + \phi_{\text{in}}\right)\left[1 + \frac{q_i}{2}\cos \Omega t\right], \tag{2.18}$$

where

$$\omega_i \approx \frac{1}{2}\Omega\sqrt{\alpha_i + \frac{1}{2}q_i^2}, \tag{2.19}$$

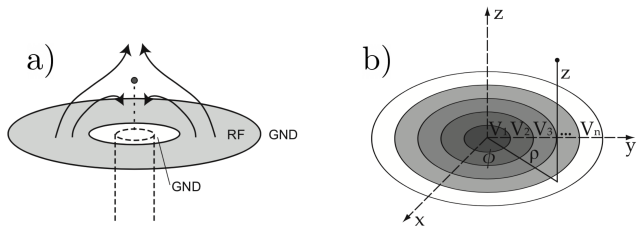

Figure 2.4: a) The planar Paul trap confines a single charged particle with a ring-shaped electrode. b) Generic definition of the planar Paul trap with concentric annular electrodes [87].

and ϕ_{in} is a phase given by the initial conditions of the trapped specimen's position and velocity. We define the secular motion or macromotion as the harmonic oscillation at frequency ω_i and amplitude K_i. The motion that corresponds to the $\cos(\Omega t)$ term is driven by the applied AC field, and is called micromotion [99].

Another Paul trap geometry with rotational symmetry is the planar or surface trap (which we will further discuss in Chapter 4) shown in Fig. 2.4 [87]. For the geometry of a planar Paul trap (PPT) shown in Fig. 2.4 a), its azimutal symmetry allows us to define the Laplace equation in charge-free space in cylindrical coordinates as in [100]:

$$\Phi(z,\rho) = \int_0^\infty J_0(k\rho)e^{-kz}A_0(k)dk, \tag{2.20}$$

where $J_0(\kappa\rho)$ is the first Bessel function, ρ is the radial direction, z is the out-of-plane direction, and $A_0(k)$ is $A_0(k) = \sum_i^n A_i(k)$ where

$$A_i(k) = k\int_{a_i}^{b_i} \rho J_0(k\rho)V_i(\rho)d\rho. \tag{2.21}$$

The geometry of the trap is defined by A_0 as a sum of n coefficients, each of which represent an annular electrode i with inner radius a_i, outer radius b_i, and a constant voltage V_i (see Fig. 2.4b).

We can solve equation (2.21) by using the identity of Bessel functions:

$$\int_0^u vJ_0(v)dv = uJ_1(u), \tag{2.22}$$

to obtain

$$A_i(k) = V_i\left[b_iJ_1(kb_i) - a_iJ_1(ka_i)\right]. \tag{2.23}$$

For now, we will consider the simple geometry of only one electrode of inner radius a and outer radius b:

$$\Phi(z=0,\rho)=\begin{cases}0, & \text{for } 0<\rho<a,\\ V\cos(\Omega t), & \text{for } a\leq\rho\leq b,\\ 0, & \text{for } b<\rho<\infty,\end{cases} \tag{2.24}$$

where V is the amplitude of the voltage applied and Ω its frequency. This results in

$$\Phi(z,\rho,t)=V\cos(\Omega t)\kappa(z,\rho), \tag{2.25}$$

where

$$\kappa(z,\rho)=\int_0^\infty \left[bJ_1(kb)-aJ_1(ka)\right]e^{-\kappa z}J_0(k\rho)dk. \tag{2.26}$$

Equation (2.26) is typically solved numerically. However, for the case of $\rho=0$, position at which the nanoparticle would be trapped, and considering $z>0$, the expression simplifies to an analytical form:

$$\kappa(z,0)=\frac{1}{\sqrt{1+\left(\frac{a}{z}\right)^2}}-\frac{1}{\sqrt{1+\left(\frac{b}{z}\right)^2}}. \tag{2.27}$$

If we expand $\Phi(z,\rho=0,t)$ around $z=z_0>0$, we can find the equation of motion along the z-axis for a particle of mass m and charge Q in the form of the previously introduced Mathieu equation [101]:

$$\ddot{\tilde{z}}(\tau)=2q\cos(2\tau)\tilde{z}(\tau), \tag{2.28}$$

where $\tilde{z}=z-z_0$ and $\tau=\Omega t/2$. The Mathieu q parameter, which determines the stability of the trap $\mid q\mid\ll 1$, is given by

$$q=\frac{2QV}{m\Omega^2}d(a,b), \tag{2.29}$$

where $d(a,b)$ is a geometrical factor in units of $[\text{length}]^{-2}$ that only depends on a and b (radii of the inner and outer electrodes considering Fig. 2.4):

$$d(a,b)=\sqrt{\frac{9(b^{\frac{2}{3}}-a^{\frac{2}{3}})^2(b^{\frac{2}{3}}+a^{\frac{2}{3}})^6}{b^{\frac{4}{3}}a^{\frac{4}{3}}(b^{\frac{4}{3}}+b^{\frac{2}{3}}a^{\frac{2}{3}}+a^{\frac{4}{3}})^5}} \tag{2.30}$$

This derivation suffices to understand the geometry of the PPT we have worked with. In chapter 4, we will study the changes in the trapping performance when a second electrode is introduced.

2.3 Cavity Optomechanics

Here, we give a brief overview of cavity optomechanics [46], a field of physics that studies the interaction between the electromagnetic field in an optical cavity and the motion of a mechanical oscillator. To describe their evolution, the common approach is the use of the optomechanics Hamiltonian, a formalism that can be applied to a wide variety of systems. In the following sections, we will introduce the different parts of this Hamiltonian: we start by describing the optical cavity, we continue with the mechanical oscillator's contribution, and we finish with the interaction term that quantifies the coupling between them.

2.3.1 Optical oscillators

To begin, we define the standard Fabry-Perot cavity model. It is formed by two highly reflective mirrors separated by a distance L. Light enters the cavity through one of the mirrors and travels back and forth multiple times. This creates interference, and depending on the cavity length L, intensity maxima appear at certain optical frequencies, also called resonances:

$$\omega_{\mathrm{c}} = m\frac{\pi c}{L}, \tag{2.31}$$

where m is an integer. The first resonance appears for $m = 1$, the fundamental mode, with $L = \lambda/2$.

In an optical cavity, the efficiency for both transmission and reflection of the mirrors can never be 100%, since, if the mirrors had 100% reflection efficiency, it would be impossible for light to exit the cavity; if the transmission was 100 %, there would be no cavity at all. Therefore, losses are an important parameter that make a cavity possible, and are represented by the decay constant κ. For instance, if the power input into the cavity is turned off, the intensity of the light circulating inside will decay by leaking out of the mirrors. This decay in intensity can be considered exponential: $I(t) = e^{-\kappa t}$, where $\tau = \kappa^{-1}$ is the photon lifetime inside the cavity. This κ is equivalent to the full width half maximum (FWHM) of the cavity resonance, which also defines the cavity's Q-factor:

$$Q = \frac{\omega_{\mathrm{c}}}{\kappa}. \tag{2.32}$$

The Q-factor is proportional to the ratio of the energy stored to energy lost in each cycle (one round trip of the light in the cavity).

A cavity optomechanical system can be modeled as a Fabry-Perot cavity where one of the mirrors is free to move—which will be set into motion by

radiation pressure from the intra-cavity light—and the other is fixed (see Fig. 2.5) [46]. The intra-cavity optical field (represented by operator $\hat{a}$) couples to the moving mirror (described by operator $\hat{b}$) via the interaction Hamiltonian H_{int}, which will be explained in detail in the following.

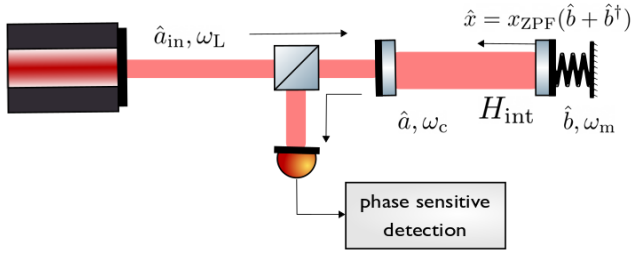

Figure 2.5: Fabry-Perot cavity with two mirrors: one fixed and one moveable. The intra-cavity optical field (represented with operator $\hat{a}$) couples to the mechanical oscillator (represented by operator $\hat{b}$)—the moving mirror—via the interaction Hamiltonian H_{int}. The change in the length of the cavity L varies the cavity's frequency ω_{c}, which translates into a phase-shift of the light reflected by the moving cavity mirror. This phase variation is due to the mechanical oscillation ω_{m} of the moving mirror, which can be measured by looking at the power spectral density of the reflected signal, with a phase-sensitive detection system. The light we measure is due to mirror losses, represented by κ, meaning that some light exits the cavity.

From equation (2.31) we see that, if the length of the cavity L varies due to a small displacement of the moveable mirror, it will induce a frequency change in ω_{c}, which will create a phase-shift in the electric field. With a cavity, we are very sensitive to phase variations due to the multiple reflections provided by the mirrors. In the case of an optomechanical cavity system, if the mirror oscillates at a mechanical frequency ω_{m}, we can extract the mechanical frequency ω_{m} by looking at the PSD of the cavity field that contains phase information (as shown in Fig. 2.5)

In cavity optomechanics, it is common to describe a cavity coupled to an external electromagnetic field with a formalism known as input-output theory [102, 103]. We use the Heisenberg equation of motion to express the evolution of the field amplitude operator (or photon annihilation operator) $\hat{a}$, where $\hat{a}^{\dagger}\hat{a}$ is proportional to the number of photons. The evolution of the optical system is given by the cavity's Hamiltonian:

$$H_{\text{c}} = \hbar\omega_{\text{c}}\left(\hat{a}^{\dagger}\hat{a} + \frac{1}{2}\right), \tag{2.33}$$

and the laser field Hamiltonian:

$$H_{\mathrm{L}} = \hbar E_0 \left(\hat{a} e^{i\omega_{\mathrm{L}} t} + \hat{a}^\dagger e^{-i\omega_{\mathrm{L}} t} \right), \tag{2.34}$$

where ω_{L} is the laser's frequency, and E_0 the amplitude of the laser's electric field. If we now consider H_{L} as part of the driving term of H_{c}, the equation of motion describing the evolution of light inside the cavity becomes

$$\begin{aligned} \partial_t \hat{a} &= -\frac{i}{\hbar}[\hat{a}, H_{\mathrm{c}}] \\ &= -i\omega_{\mathrm{c}} \hat{a} - \frac{\kappa}{2}\hat{a} + \sqrt{\kappa}\hat{a}_{\mathrm{in}}, \end{aligned} \tag{2.35}$$

where the laser contribution is considered within $\hat{a}_{\mathrm{in}} \to \hat{a}_{\mathrm{in}} + \frac{iE_0}{\sqrt{\kappa}}$ [102]. Equation (2.35) is sometimes referred to as the quantum Langevin equation [102]. Note that we introduced a decay channel of rate $\frac{\kappa}{2}$, which is halved because we are dealing with field amplitudes instead of intensities.

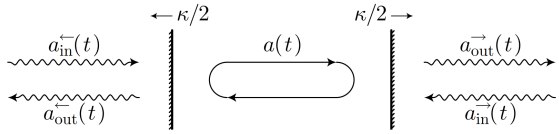

Figure 2.6: Two-sided cavity schematics in the input-output formalism, with decay rate $\kappa/2$ for each mirror, and thus a total decay rate of κ. Image taken from [102].

Defining the unitary rotating-frame operator $a(t) = \hat{a}(t)e^{i\omega_{\mathrm{L}} t}$ and applying it to the variables of equation (2.35), we obtain:

$$\partial_t a = (\partial_t \hat{a}) e^{i\omega_{\mathrm{L}} t} + i\omega_{\mathrm{L}} a \tag{2.36}$$

$$= i(\omega_{\mathrm{L}} - \omega_{\mathrm{c}})a - \frac{\kappa}{2}a + \sqrt{\kappa}a_{\mathrm{in}}, \tag{2.37}$$

and if we define the laser detuning as $\Delta = \omega_{\mathrm{L}} - \omega_{\mathrm{c}}$:

$$\partial_t a = i\Delta a - \frac{\kappa}{2}a + \sqrt{\kappa}a_{\mathrm{in}}. \tag{2.38}$$

We can also re-write the Hamiltonian as:

$$H_{\mathrm{c}} = \hbar \Delta \hat{a}^\dagger \hat{a}, \tag{2.39}$$

where the $1/2$ term is neglected since it will just shift the energy by a constant value and does not affect the dynamics.

The input, output, and intra-cavity electromagnetic fields satisfy the input-output relation [102]:

$$a_{\text{out}} - a_{\text{in}} = -\sqrt{\kappa}a, \tag{2.40}$$

which will be satisfied by every port of a cavity.

We can obtain the classical version of equation (2.38) by taking expected values $\langle a \rangle$. The $\frac{\kappa}{2}a$ term leads to an exponential decay, and the detuning term to a periodic modulation of the field's amplitude inside the cavity with angular frequency Δ. The input-output relation from equation (2.40) allows us to derive the steady state amplitude relations, such as the reflection or transmission transfer functions, by moving to the frequency domain. For the case of the two sided cavity described in Fig. 2.6, the transfer functions—in terms of the input $a_{\text{in}}(\omega)$—for the intra-cavity field are:

$$\mathcal{H}_{\text{in}}(\omega) = \frac{\sqrt{\kappa/2}}{-i\Delta + \kappa/2} \tag{2.41}$$

and for the transmitted field

$$\mathcal{H}_{\text{tr}}(\omega) = \frac{\kappa/2}{-i\Delta + \kappa/2}. \tag{2.42}$$

In both cases, $\Delta = \omega - \omega_{\text{c}}$, where ω is the frequency variable. Note these two expressions are only an approximation for the case of high Q and for only one cavity resonance.

Taking the modulus squared of equation (2.41), we obtain the power transfer function of the intra-cavity field. Multiplying it by the number of input photons, we obtain the steady state cavity population $n_{\text{c}} = \langle a^\dagger a \rangle$:

$$n_{\text{c}} = |\langle a \rangle|^2 = \frac{\kappa/2}{\Delta^2 + (\kappa/2)^2} \frac{P}{\hbar\omega_{\text{L}}}, \tag{2.43}$$

where $P = \hbar\omega_{\text{L}}|\langle a_{\text{in}} \rangle|^2$ is the input power launched into the cavity.

2.3.2 Mechanical oscillators

So far, we have assumed that our levitated nanoparticle's evolution in time is described by a linear equation of motion (see section 2.1.1). Here, we will still assume that the mechanical oscillator satisfies the equation of a harmonic oscillator (see equation (2.7) in section 2.1.1). However, we will apply a quantum mechanical treatment, obtaining the following Hamiltonian of the oscillator [46]:

$$H_{\text{m}} = \hbar\omega_m \left(\hat{b}^\dagger \hat{b} + \frac{1}{2} \right), \tag{2.44}$$

where $\hat{b}^\dagger$ and $\hat{b}$ are the phonon creation and annihilation operators. The position and momentum are defined as:

$$\hat{x} = x_{\mathrm{ZPF}}(\hat{b}^\dagger + \hat{b}), \quad \hat{p} = -im\omega_{\mathrm{m}} x_{\mathrm{ZPF}}(\hat{b}^\dagger - \hat{b}),$$

and

$$x_{\mathrm{ZPF}} = \sqrt{\frac{\hbar}{2m\omega_{\mathrm{m}}}},$$

is the zero-point fluctuation amplitude of the oscillator in the ground state $|0\rangle$, such that $\langle 0|\hat{x}^2|0\rangle = x_{\mathrm{ZPF}}^2$. In the following, we ignore the constant term of the Hamiltonian, $\frac{1}{2}\hbar\omega_{\mathrm{m}}$ because it doesn't affect the oscillator dynamics.

2.3.3 Optomechanical coupling: Hamiltonian formulation

In one of the main experiments in this manuscript, we couple a mechanical oscillator—a levitated nanoparticle—to an optical oscillator—a photonic crystal nanocavity. The interaction between the two can be characterized with the figure of merit g_0: the single photon optomechanical coupling strength. This parameter is defined by the interaction between a mechanical oscillator and an optical oscillator, so we need to add a coupling term H_{int} to the Hamiltonian $H = H_{\mathrm{c}} + H_{\mathrm{m}}$ we've described so far in equations (2.44) and (2.33). The interaction term introduces a nonlinearity to the equations. However, since the interaction between oscillators is usually small, it is common practice to linearize it. The expressions obtained are known as linearized quantum Langevin equations [104].

The intuition behind this interaction is that the mechanical mode changes the effective cavity length (defined in equation (2.31)). This modifies ω_{c}, and therefore the light within the cavity acts back on the mechanical oscillator by optical forces. This type of coupling is usually known as dispersive. So, if we expand ω_{c} for small values of x:

$$\omega_{\mathrm{c}}(x) = \omega_{\mathrm{c}} + \frac{\partial\omega_{\mathrm{c}}}{\partial x}x + \ldots,$$

where

$$G = \frac{\partial\omega_{\mathrm{c}}}{\partial x} \approx \frac{\omega_{\mathrm{c}}}{L}, \tag{2.45}$$

is the optomechanical coupling for the case of the optical cavity described in section 2.3.1. We can also define, g_0, the single photon optomechanical coupling strength as the optical frequency shift due to the zero point motion of the mechanical oscillator:

$$g_0 = G_x x_{\mathrm{ZPF}} = \frac{\partial\omega_{\mathrm{c}}(x)}{\partial x}\sqrt{\frac{\hbar}{2m\omega_{\mathrm{m}}}}. \tag{2.46}$$

We will later see in section 3.2 that, for our system, g_0 grows for small cavity mode volumes and a large overlap between the nanoparticle and the near-field of the nanocavity.

The optomechanical Hamiltonian will be the sum of H_m and H_c, described in the previous sections, plus an interaction term $H_\mathrm{int} = -\hbar G\hat{x}\hat{a}^\dagger\hat{a}$ [46]:

$$\begin{aligned} H &= H_\mathrm{c} + H_\mathrm{m} + H_\mathrm{int} \\ &= \hbar\Delta\hat{a}^\dagger\hat{a} + \hbar\omega_\mathrm{m}\hat{b}^\dagger\hat{b} - \hbar G\hat{x}\hat{a}^\dagger\hat{a} \\ &= \hbar\left(\Delta - G\hat{x}\right)\hat{a}^\dagger\hat{a} + \hbar\omega_\mathrm{m}\hat{b}^\dagger\hat{b}, \end{aligned} \tag{2.47}$$

by using the change of variables $\hat{x} = x_\mathrm{ZPF}(\hat{b}^\dagger + \hat{b})$, and $g_0 = Gx_\mathrm{ZPF}$,

$$H = \hbar\Delta\hat{a}^\dagger\hat{a} + \hbar\omega_\mathrm{m}\hat{b}^\dagger\hat{b} - \hbar g_0\hat{a}^\dagger\hat{a}(\hat{b}^\dagger + \hat{b}). \tag{2.48}$$

The last term is known as the interaction part of the Hamiltonian, H_int, and describes the coupled oscillator dynamics. For small fluctuations of the cavity's field, we can linearize H by approximating $\hat{a}$ as

$$\hat{a} = \langle\hat{a}\rangle + \delta\hat{a}, \tag{2.49}$$

where $\langle\hat{a}\rangle = \sqrt{\langle n_\mathrm{c}\rangle} \in \mathbb{R}^+$ is the average coherent amplitude and $\delta\hat{a}$ the fluctuating part. If we substitute (2.49) in the interaction Hamiltonian:

$$H_\mathrm{int} = -\hbar g_0(\langle\hat{a}\rangle + \delta\hat{a})^\dagger(\langle\hat{a}\rangle + \delta\hat{a})(\hat{b}^\dagger + \hat{b}). \tag{2.50}$$

We now expand H_int and dissect the powers of $\langle\hat{a}\rangle$: we discard the $\langle\hat{a}\rangle^2$ because it will just shift the origin of the mechanical oscillator, and also the term with $\delta\hat{a}^\dagger\delta\hat{a}$ for being small. Therefore, considering $\langle\hat{a}\rangle^\dagger = \langle\hat{a}\rangle = \sqrt{\langle n_\mathrm{c}\rangle}$, the linear H_int is

$$H_\mathrm{int} = -\hbar g_0\sqrt{\langle n_\mathrm{c}\rangle}(\delta\hat{a}^\dagger + \delta\hat{a})(\hat{b}^\dagger + \hat{b}). \tag{2.51}$$

If we perform the same expansion using equation (2.49) for the cavity Hamiltonian term, we obtain the complete linear Hamiltonian:

$$H = \hbar\Delta\delta\hat{a}^\dagger\delta\hat{a} + \hbar\omega_\mathrm{m}\hat{b}^\dagger\hat{b} - \hbar g_0\sqrt{\langle n_\mathrm{c}\rangle}(\delta\hat{a}^\dagger + \delta\hat{a})(\hat{b}^\dagger + \hat{b}). \tag{2.52}$$

The linearized Quantum Langevin Equations (QLEs) that we have obtained have an analytical solution [104]. They predict the mechanical and optical response to the interaction and can be used to describe cavity cooling or displacement detection [105]:

$$\begin{aligned} \dot{\hat{x}} &= \omega_\mathrm{m}\hat{p} \\ \dot{\hat{p}} &= -\omega_\mathrm{m}\hat{x} + \Gamma\hat{p} + G\sqrt{\langle n_\mathrm{c}\rangle}(\delta\hat{a}^\dagger + \delta\hat{a}) \\ \delta\dot{\hat{a}} &= \left(i\Delta - \frac{\kappa}{2}\right)\delta\hat{a} + iG\sqrt{\langle n_\mathrm{c}\rangle}\hat{x} + \sqrt{\kappa}\hat{a}_\mathrm{in}. \end{aligned} \tag{2.53}$$

In our experiment, the nanocavity provides the optical field and the levitated object the dispersive coupling. Both oscillators interact via a coupling factor: the single photon optomechanical coupling parameter g_0.

Chapter 3

Nanocavities for levitodynamics

In this chapter we describe the basic theory behind photonic crystal nanocavities, followed by their use in levitodynamics experiments. We finish by discussing their nonlinear thermal behavior: bistability and self-induced oscillations in the nanocavity's transmission.

3.1 Photonic crystals theory

If we go back to the fundamentals of solid state physics, we will find many similarities between photonic crystals and semiconductors: bands, dispersion diagrams, etc. In this section, we aim to provide the basics of photonic crystals. For an in depth review of the topic, see [106].

Photonic crystals (PhCs) are naturally-occurring on Earth: they can be found in opals and on the wings of a butterfly. They are similar to crystalline solids: they are formed by a periodic variation in space of the index of refraction. The periodicity selects the electromagnetic waves that are allowed to propagate through the crystal. With the right periodicity, we can have destructive interference, giving rise to band gaps: frequency regions where light can't propagate in the structure.

Depending on how many directions in space the index of refraction varies, we can classify PhCs as 1D, 2D, and 3D. The device that we have developed in this work is a 1D PhC, case that we will study in detail.

The simplest form of a 1D PhC consists in a multilayer film with period a (see Fig.3.1). Since we only consider materials that are linear, lossless, istrotopic, and periodic along z (wave vectors k_z and $\mathbf{k}_{xy}$), we can describe

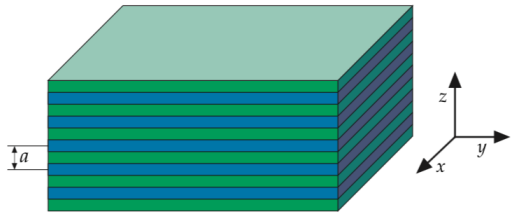

Figure 3.1: Diagram of a 1D PhC: a multilayer film with two materials of dielectric constant ϵ_1 and ϵ_2 and with a period a [106].

the electric field in the Bloch form:

$$\mathbf{H}_{n,k_z,\,\mathbf{k}_{xy}}(\,\mathbf{r}) = e^{i\,\mathbf{k}_{xy}\cdot\rho} e^{ik_z z}\;\mathbf{u}_{n,k_z,\,\mathbf{k}_{xy}}(z), \tag{3.1}$$

where $\mathbf{u}(z) = \mathbf{u}(z+R)$ and R is an integer multiple of the spatial period a of the multilayer, and n is the band number. From the symmetry of the problem, $\mathbf{k}_{xy}$ can assume any value. If we consider the periodic boundary conditions imposed on $\mathbf{u}(z)$, we can restrict the eigenvalue problem to a single unit cell of the crystal, which results on a discrete spectrum of eigenfrequencies for any given wavevector k_z. Moreover, due to the symmetries of the lattice [107], we can just consider the reciprocal lattice, also known as the irreducible one-dimensional Brillouin zone[1] of $-\pi/a < k_z < \pi/a$.

If we consider that light propagates just along the z direction, we can set $\mathbf{k}_{xy} = 0$. Hence, from now on, k_z wil be referred to as k for simplicity. The modes that are able to propagate within the photonic crystal lie along the light line:

$$\omega(k) = \frac{ck}{\sqrt{\epsilon}}. \tag{3.2}$$

By the condition in equation (3.1), k must repeat itself outside the Brillouin zone. Comparing the band diagram of a completely homogeneous material to that of a multilayer material, there will be a band gap between the top and lower band for the latter (see Fig. 3.2). This is called the photonic band gap, and in these frequencies light is not allowed to propagate.

In general, the greater the contrast between the index of refraction (or dielectric constants ϵ) of the layers, the wider the band gap (see Fig. 3.2 b) and c)). Thus, in an actual design, our choice of materials and geometry will affect the band gap.

[1]The Brillouin zone is defined as the primitive cell of the reciprocal lattice in the frequency domain [108], which allows us to describe wave propagation in a periodic medium by using the Bloch form.

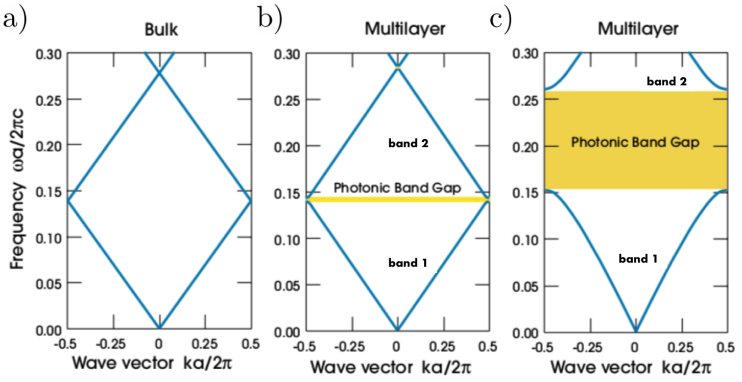

Figure 3.2: Three band diagrams: 1) bulk material, 2) multilayer with layers of $\epsilon = 12$ and 13, and 3) multilayer with layers of $\epsilon = 1$ and 13 [106]. Band 1 contains the dielectric modes and band 2 contains the air modes.

There are two ways for the electric mode to propagate (see Fig. 3.3): through the low-ϵ layers (band 1: dielectric mode), or through the high-ϵ layers (band 2: air mode). If we consider the local energy density for both of these cases, we see that the mode just under the gap—the dielectric mode—concentrates the electric field's energy in the higher-ϵ region (see Fig. 3.3 a) and c)), and the mode just above the gap—the air mode—concentrates the electric field's energy in the lower-ϵ region (see Fig. 3.3 b) and d)). These two modes, air and dielectric, are equivalent to the conduction and valence bands in semiconductors, respectively.

After considering a perfectly periodic system, we can introduce a defect by breaking the translational symmetry. In Fig. 3.4 we have created a defect by doubling a single layer of the lower ϵ material. Although "breaking" the periodicity prevents us from describing the modes with a vector k, we can still exploit band structures to determine whether a certain frequency will be allowed to propagate inside the crystal.

Ultimately, a defect allows localized modes to exist at frequencies that are inside the photonic band gap. This means that, in essence, by creating a defect we are building a cavity: the localized mode exponentially decays once it enters the crystal, and the multilayer films at both sides of the defect behave like mirrors (i.e. trapping the light to travel back and forth between them). Depending on how the defect is created, we can "pull" modes down into the photonic band gap from the air (higher) band or "raise" modes up into the gap from the dielectric (lower) band. But, importantly, by the linearity of the equations, once we have a design for a given material, we can scale everything (thickness, width, sizes, etc) and keep the same band

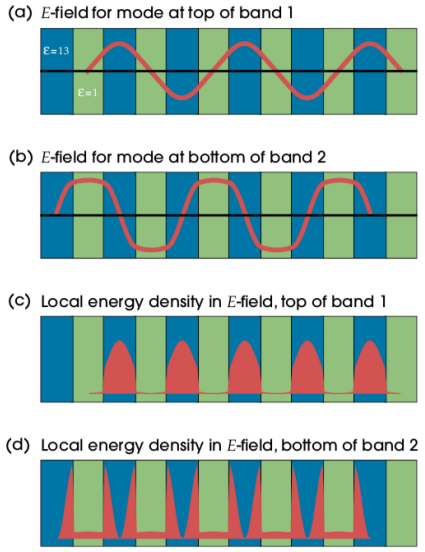

Figure 3.3: Electric field for the dielectric mode (top of band 1) is shown in (a) and air mode (bottom of band 2) in (b) for the case of the multilayer film with layers with an ϵ of 13 and 1 in green and blue, respectively. The local energy density for the dielectric mode is shown in (c) and for the air mode in (d) [106].

structure with scaled frequencies and mode profiles as long as the indices of refraction remains the same.

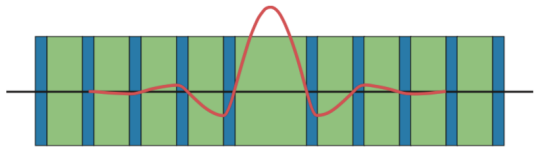

Figure 3.4: Defect in a multilayer film. The defect is formed by doubling the thickness of a single low-ϵ layer. The red curve shows the electric field strength of the defect for on-axis propagation [106].

Experimentally, we can create a defect that allows either the air mode or the delectric mode mode to propage. In the case of the air mode, the nanocavity's resonance is close to the blue-side of the bandgap: we "pull" the mode down into the gap from the air (higher) band as we see in Fig. 3.5 a). For the dielectric mode, the nanocavity's resonance is close to the red-side of the bandgap: we "raise" modes up into the gap from the dielectric (lower) band as we show in Fig. 3.5 b).

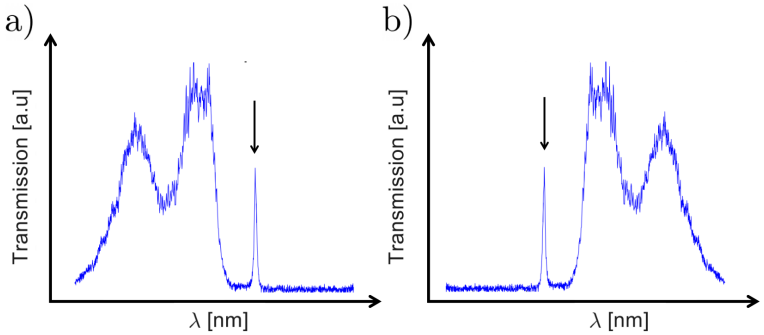

Figure 3.5: Transmission spectrum for: a) an air mode nanocavity and b) for a dielectric mode nanocavity. The resonance peak is indicated with an arrow in both cases.

3.2 Nanocavities for optomechanics

In section 2.3, we introduced the basics of cavity optomechanics with the example of a cavity where one of the mirrors is on a spring. However, the theory can be applied to any system where the mechanical motion of an object is coupled to the frequency of a cavity. In the last 15 years, this formalism has been used to describe systems as diverse as reflective micromechanical membranes [57], microtoroids, disks, rings, spheres [58, 59, 60, 61], superconducting microwave circuits [62], and cold atoms trapped in an optical cavity [109]. In these works, besides aiming for higher optical and mechanical Q-factors, their size is also miniaturized. This trend for lower masses and dimensions is not a mere coincidence: it is because of how the mass of the mechanical oscillator and the volume of the cavity relates to the strength of the fundamental optomechanical interaction, parametrized with the g_0 coefficient.

Let's go back to the description of a cavity optomechanics experiment (see section 2.3.1). We've shown in equations (2.45) and (2.46) that the optomechanical coupling rate g_0 is $\propto \frac{1}{L}$, where L is the length of the cavity, and $\propto \frac{1}{m}$, where m is the mass of the movable mirror; this last dependence comes from $x_{\mathrm{ZPF}} = \sqrt{\frac{\hbar}{2m\omega_{\mathrm{m}}}}$.

Since we aim for a large optomechanical interaction, from the expressions above, it is clear that a system with both a short cavity length and a mechanical oscillator with a small mass will provide a large g_0. For example, the g_0 of a system made of an atom and an optical cavity is $\propto \frac{1}{V_{\mathrm{c}}}$, where V_{c} is the effective volume of the cavity [110]. For this reason, lithographically fabricated microresonators allowed the first observation of strong coupling for single atoms with photons [111]. Other common devices are nanotapers: they have also enabled efficient coupling of atomic fluorescence to a guided mode [112]. Nanotapers can also trap and cool neutral atoms with a 1D optical lattice created by a two-color evanescent field [113]. A photonic crystals cavity is another platform where a single trapped atom can couple to, and also probe, the cavity's near-field [114]. More recently, scientists have observed cooperative atom-atom interactions with a photonic crystal waveguide [115].

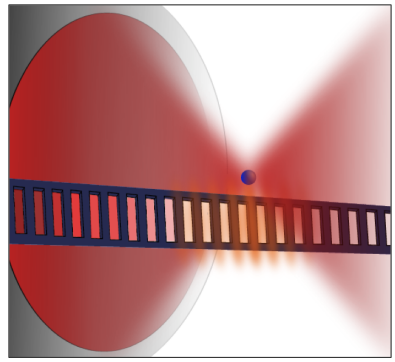

Figure 3.6: Diagram of our optomechanical system: a levitated nanoparticle coupled to a photonic crystal nanocavity. Image by P.Z.G. Fonseca.

Just like for atoms, a small volume is also important for our system of a levitated nanoparticle and a photonic crystal nanocavity (see Fig. 3.6): $g_0 \propto \frac{V_\mathrm{p}}{V_\mathrm{c}}$, where V_p is the volume of the nanoparticle [116]. Notice, however, that although reducing the cavity volume V_c is important, it is also key to keep a low optical decay rate (κ) or, equivalently, a high optical quality factor $Q = \frac{\omega_\mathrm{c}}{\kappa}$. In other words, we would like to maximize the ratio Q/V_c.

Our strategy to reduce the volume of the cavity is to use a PhC nanocavity, which concentrates light in very small volumes, down to the theoretical minimum value of $\left(\frac{\lambda}{2n}\right)^3$, where n is the index of refraction of the cavity's material [117]. These devices have demonstrated Q-factors of $\sim 10^6$ in the telecom wavelength range ($\lambda = 1300$ nm – 1600 nm) with Si and GaAs [118, 119]. Because of this decrease in volume, a nanocavity can increase g_0 by 3 orders of magnitude when compared to macrocavities [120], resulting in better displacement sensitivity with smaller number of photons. Regarding the mechanical oscillator, levitated nanoparticles in vacuum have high mechanical Q-factors (10^7 at $P = 10^{-5}$ mbar, and 10^{11} at $P = 10^{-9}$ mbar) [121] and a femtogram (10^{-15} g) mass [28].

For the optomechanical interaction to occur, the nanoparticle must be within the nanocavity's near-field. This near-field is given by the evanescent wave at the boundary between the nanobeam and air. The evanescent wave corresponds to the non-propagating term of the electromagnetic field, and its energy is concentrated in the vicinity of its source and decays exponentially away from it [94, 122, 123, 124]. The oscillating nanoparticle alters the near-field of the photonic structure. This affects the nanocavity's spectral distribution of the field propagating through the photonic structure that consequently influences the near-field interaction with the nanoparticle [125].

It is commonly accepted that a distance beyond 2λ away from the structure, this evanescent field is negligible. Therefore, our levitodynamics near-field experiment happens in the very close proximity of the nanocavity.

3.3 Thermal dynamics of the nanocavities

Heating and its effects need to be considered when substantial optical powers are delivered to small volumes. As we've just seen, for our optomechanics experiment we strive for a high Q and low V_c. At the same time, the optical power density in a cavity scales with Q/V_c [126, 127]. Hence, a large Q/V_c will result in an increase of temperature of the structure.

When a cavity heats up, λ_{res} shifts because of a temperature increase: $\lambda_{res}(T)$ [66]. As we will show in this work, our 1D PhC nanocavity exhibits thermal effects: its spectral response is strongly dependent on its temperature. Moreover, it shows bistability and excitability behavior[2], such as self-induced oscillations in the output transmission for a fixed input power and detuning from the cavity's resonance.

All these effects are due to nonlinearities in the cavity's evolution equations and, originally, were undesired; however, we've explored them to understand and benefit from them as much as possible. Outside the field of optomechanics, heating effects are exploited in micro- and nanocavities for self-pulsing [77], lasing [78], and bistable devices [68, 69, 70].

One of the main motivations to pursue bistable nanosystems is to create analogs of electronic components, and enable all-optical systems that are fast and work at low optical power; key characteristics for on-a-chip integrated photonic circuits. Integrated photonic devices would have an advantage over optical-to-electrical converters, since their performance is more energy efficient [71]. Micro- and nanocavities provide a low bistability threshold: their high Q/V_c allows for the high heat density in small volumes [68] that could facilitate such technology.

A bistable optical system provides two co-existing stable states for transmission or reflection for the same input parameters, and it is a steady state effect. Yet, these thermal nonlinearities in resonators can also give rise to rich time-varying phenomena like excitability, which underlies spiking behavior to an external stimulus [76]. For instance, excitability is studied in neuroscience with the Hodgkin-Huxley model because it explains the firing

[2]Excitability is a nonlinear dynamics mechanism underlying pulse-like responses to a small perturbation in a system possessing one stable state [76].

of neurons [128]. A simpler model, the FitzHugh-Nagumo model [129, 130], is often used to describe excitability phenomena in optical devices [131, 132].

In a system that presents excitability, self-induced oscillations can occur under certain conditions of wavelength and optical power of the input radiation. To create this excitable behavior, we need two competing mechanisms at different timescales: one that shifts the resonance in one direction and another in the opposite direction. In many Si bistable devices, self-induced oscillations are a combination of the thermo-optic effect (shifts to the red, slow) and two photon absorption (shifts to the blue, fast) [75, 77, 132]. In Si_3N_4 there is no two photon absorption due to a wide band gap [133]. Hence, two phenomena that drive these oscillations in Si_3N_4 are the thermo-mechanic effect (blue-shift, slow) and the thermo-optic effect (red-shift, fast) [83].

3.3.1 Thermo-optic effect and thermal expansion

In silicon nitride there are two main effects that red-shift the cavity's resonance λ_{res} due to the material's properties: a) the thermo-optic effect, and b) thermal expansion. We can describe this variation of the resonance with temperature as [66]:

$$\lambda_{\text{res}}(\Delta T) = \lambda_0 \left[1 + \left(\epsilon + \frac{dn}{dTn_0}\right)\Delta T\right], \tag{3.3}$$

where λ_{res} is the new resonance, λ_0 is the cold cavity resonance, ϵ is the thermal expansion coefficient, $\frac{dn}{dTn_0}$ is the normalized thermo-optic coefficient, n_0 is the cold index of refraction of the cavity's material, and ΔT is the induced change of temperature.

In silicon nitride, the $\frac{dn}{dTn_0}$ term dominates over ϵ because the dn/dT reported in literature is $\sim 2.5 \cdot 10^{-5}$ K^{-1} [134, 135]), whereas the value of the expansion coefficient ϵ is an order of magnitude smaller $\sim 3 \cdot 10^{-6}$ K^{-1} [136].

Our Si_3N_4 nanocavities show bistability behavior due to the aforementioned thermo-optic effect. As we've described here, this nonlinear effect makes λ_{res} shift to the red.

3.3.2 Bistability

Bistability in an optical system appears when combining a resonance that localizes light in the spectral domain and a nonlinearity that alters the spectral response as a function of light intensity. This translates into two co-existing stable states for transmission or reflection for the same input parameters. Optical bistability was first demonstrated theoretically [137] and later on,

experimentally [138]. Many nanocavities and microcavities exhibit this behavior.

To understand this effect, let us consider equation (2.37), which describes the evolution of light inside the cavity (for field intensities):

$$\partial_t a = i(\omega_\mathrm{L} - \omega_\mathrm{c})a - \kappa a + \sqrt{\kappa} a_\mathrm{in}. \tag{3.4}$$

If we now consider that our ω_c term undergoes a nonlinear resonance frequency shift $\omega_\mathrm{c} \pm \frac{|a|^2\kappa^2}{P_0}$, where P_0 is the characteristic or threshold nonlinear power of the cavity, the modified equation will be able to describe the aforementioned optical bistability. In the following, we will consider a negative frequency shift, i.e. blue-shift:

$$\partial_t a = i\left(\omega_\mathrm{L} - \omega_\mathrm{c} + \frac{|a|^2\kappa^2}{P_0}\right)a - \kappa a + \sqrt{\kappa} a_\mathrm{in}. \tag{3.5}$$

We consider the steady states for equation (3.5), with $\partial_t a = 0$, divide all terms by κ, and define $\Delta' = \Delta/\kappa = (\omega_\mathrm{L} - \omega_\mathrm{c})/\kappa$:

$$0 = i\left(\Delta' + \frac{|a|^2\kappa}{P_0}\right)a - a + \frac{a_\mathrm{in}}{\sqrt{\kappa}}, \tag{3.6}$$

which we can re-write to calculate the modulus squared:

$$\frac{|a_\mathrm{in}|^2}{\kappa} = \left[\Delta'^2 + \left(\frac{|a|^2\kappa}{P_0}\right)^2 + 2\Delta'\frac{|a|^2\kappa}{P_0} + 1\right]|a|^2. \tag{3.7}$$

We define $|a_\mathrm{in}|^2 = P_\mathrm{in}$, $|a|^2 = \frac{P_0 A}{\kappa}$ and $A = \frac{|a|^2\kappa}{P_0} = P_\mathrm{out}/P_0$, such that

$$\frac{P_\mathrm{in}}{\kappa} = \left[\Delta'^2 + A^2 + 2\Delta' A + 1\right]\frac{P_0 A}{\kappa}, \tag{3.8}$$

and multiplying everything by κ we obtain

$$P_\mathrm{in} = \left[\left(\Delta' + A\right)^2 + 1\right]P_0 A. \tag{3.9}$$

Therefore,

$$\frac{P_\mathrm{in}}{P_0} = \left[\left(\Delta' + A\right)^2 + 1\right]A = \left[\left(\Delta' + \frac{P_\mathrm{out}}{P_0}\right)^2 + 1\right]\frac{P_\mathrm{out}}{P_0}. \tag{3.10}$$

We can re-write equation (3.10), as

$$\frac{P_\mathrm{out}}{P_0} = \frac{P_\mathrm{in}/P_0}{\left(\Delta' + \frac{P_\mathrm{out}}{P_0}\right)^2 + 1}, \tag{3.11}$$

and we can define the detuning, for a blue-shift, as

$$\Delta' = -\frac{P_{\text{out}}}{P_0} \pm \sqrt{\frac{P_{\text{in}}}{P_0} - 1}. \tag{3.12}$$

For bistability to exist, we require a $|\Delta'| > \sqrt{3}/2$ [77], which corresponds to the case where the curve in Fig. 3.7 a) has two critical points at P_{down} and P_{up}. Moreover, if we take a look at Fig. 3.7, for a given power threshold P_0 and a fixed excitation wavelength, there is a minimum power P_{up} such that the cavity jumps to the high transmission branch. From the high transmission state, the cavity jumps back to the low transmission state for powers below P_{down}. The power difference between P_{up} and P_{down} is what creates this hysteresis cycle. In a similar way, for a fixed input power P_{in}, there is a detuning Δ_{up} that allows us to follow the deformed resonance shape (see Fig. 3.7 b)), until we jump to a spectral region of low transmission at detuning Δ_{down}.

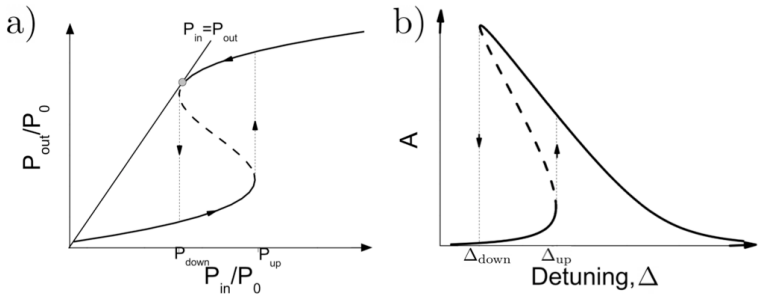

Figure 3.7: a) Transmitted power as a function of P_{in} showing the characteristic features of a bistable optical system. The solid line shows stable states while the dashed line shows unstable states. The arrows show the direction of the hysteresis cycle. The solid line corresponds to $P_{\text{in}} = P_{\text{out}}$. The gray dot shows the bistability threshold where $P_{\text{in}} = P_{\text{out}}$ and the curve intersect. b) Bending of the resonance due to a blue-shift. Transmitted signal for different detuning for a fixed P_{in}. Image adapted from [76].

In the case of a red-shift, the cavity resonance would be $\omega_c + \frac{|a|^2\kappa^2}{P_0}$, and we would reach similar expressions to equations (3.11) and (3.12):

$$\frac{P_{\text{out}}}{P_0} = \frac{P_{\text{in}}/P_0}{\left(\Delta' - \frac{P_{\text{out}}}{P_0}\right)^2 + 1}, \tag{3.13}$$

where we have re-defined the detuning, for a red-shift, as

$$\Delta' = \frac{P_{\text{out}}}{P_0} \pm \sqrt{\frac{P_{\text{in}}}{P_0} - 1}. \tag{3.14}$$

3.3.3 Self-induced oscillations

As we have seen in the previous section, bistability is a steady state effect. However, nonlinearities in resonators can also give rise to complex time-varying phenomena. Bistability is known as the building block of all-optical memories, switching and logic gates [139]; and, excitability explains spiking behavior in transmission or reflection to an external stimuli. For instance, excitability is studied in neuroscience because it explains the firing mechanism of neurons [128]. It can be described as a small perturbation from a single stable point that results in a large and lasting excursion away from it before the systems comes back to equilibrium.

In optics, this was first demonstrated on a semiconductor laser with optical feedback [140], and more recently in microphotonics and nanophotonics with photonic crystals [141], and in optomechanics [142].

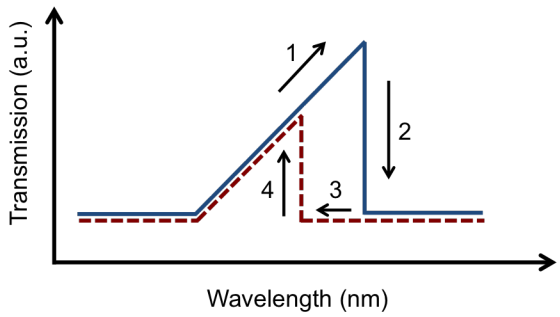

Figure 3.8: Simple diagram of one cycle of the nanocavity's transmission for the self-induced oscillation regime. The time scale of the oscillations are determined by the recovery process, which is a slow thermo-mechanical effect. 1) We begin with a blue-detuned laser line λ_L, which is kept fixed with respect to the already thermo-optically distorted cavity resonance. The nanocavity's temperature increases and its resonance blue-shifts towards λ_L, so the transmission of the nanocavity increases. 2) Once the cavity's resonance reaches λ_L, the nanocavity resonance shifts further blue and the transmitted signal drops to a minimum. 3) Since the nanocavity is out of resonance with respect to λ_L, it begins to cool, slowly red-shifting back. 4) At this point the nanocavity jumps back into resonance with the laser and the transmission through it begins to increase. The cycle begins again starting from point 1).

Different types of excitability exist [143]. Our system corresponds to type II excitability, where self-induced oscillations are generated when a stable fix point is destabilized by going through a Hopf bifurcation[3]. A cycle of the

[3]Critical point where a system's stability switches and a periodic solution arises [143]

self-induced oscillations is shown in Fig.3.8.

Depending on the design and size of the resonator, the self-induced oscillation's period can range from ms to ns [69, 73, 75, 144]. In the scientific literature, works with silicon nitride ring resonators have reported bistability and self-induced oscillations of much slower time scales (see Fig. 3.9) due to the thermo-optic effect (is fast and induces a red shift) and a thermo-mechanical effect (is slow and induces a blue shift) [83, 145].

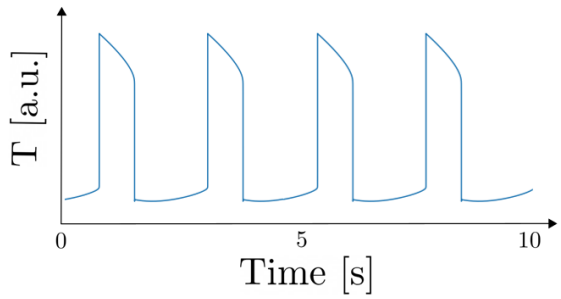

Figure 3.9: Plot of the transmission for self-induced oscillations in a whispering gallery mode resonator from the model and experiment shown in [83].

In our nanocavities, we also observe self-induced oscillations (similar to those shown in Fig. 3.9). A simple way to describe this behavior is by adapting the theoretical model from [83] to our nanocavity.

In this model [83], we define the cold resonance of the cavity as λ_0, and the linewidth $\Delta\lambda$. We consider that the resonance of the nanocavity λ_{res} varies with temperature. More precisely, λ_{res} depends on three temperatures: T_0 temperature of the environment, T_1 temperature of the nanocavity, and T_2 temperature of the rest of the nanobeam (see Fig. 3.10). In this way:

$$\lambda_{\text{res}} = \lambda_0 + \frac{\partial\lambda_{\text{res}}}{\partial T_1}(T_1 - T_0) + \frac{\partial\lambda_{\text{res}}}{\partial T_2}(T_2 - T_0). \tag{3.15}$$

We can also describe the normalized transmission through the nanobeam as:

$$\mathcal{T}(\lambda_{\text{L}}, T_1, T_2) = \frac{1}{1 + \left(\frac{\lambda_{\text{L}} - \lambda_{\text{res}}(T_1, T_2)}{\Delta\lambda/2}\right)^2}. \tag{3.16}$$

The change of temperature in the nanocavity itself is described by:

$$\dot{T}_1 = \frac{P_{\text{abs}}}{m_1 C}\mathcal{T}(T_1, T_2) - \frac{G_{1,2}}{m_1 C}(T_1 - T_2). \tag{3.17}$$

The temperature dynamics of the nanocavity depends on the power absorbed P_{abs}, the mass m_1 of the cavity and the heat capacity C of Si_3N_4. It also depends on the thermal conductance $G_{1,2}$ from the nanocavity to the rest of the nanobeam:

$$\dot{T}_2 = \frac{G_{1,2}}{m_2 C}(T_1 - T_2) - \frac{G_2}{m_2 C}(T_2 - T_0)\,, \tag{3.18}$$

where G_2 expresses how heat diffuses from the nanobeam (of mass m_2) to the environment at temperature T_0.

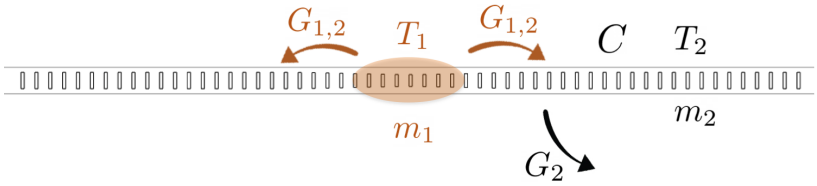

Figure 3.10: Schematics of the model for self-induced oscillations in the nanocavity's transmission.

Chapter 4

Trapping and manipulation with a planar Paul trap

4.1 Introduction

One of the motivations to work with a Planar Paul Trap (PPT) is to levitate objects that would otherwise burn in an optical tweezer as well as to explore a possible controlled nanoparticle loading mechanism to the optical tweezer. For instance, a charged particle could be transferred from the PPT to an optical tweezer (see Fig. 4.1) and then brought close to a photonic crystal nanocavity. The most common particle loading method in levitodynamic's experiments are nebulizers: they create a mist of nanoparticles in an ethanol suspension. This mechanism forces us to open the vacuum chamber each time one needs to load a particle. However, by directly loading nanoparticles in vacuum, we would avoid also contamination from other nebulized particles that are not trapped.

Some work in this direction has been recently accomplished: loading particles in vacuum into a Paul trap has been proven [146], and also in hybrid traps made of Paul traps and optical fields [47, 48]. In general, it is easier to load into a Paul trap than into an optical trap because the confinement volume of a Paul trap is much larger (e.g. roughly 4× in our work) and the potential is 100× deeper. Moreover, the transfer to an optical field can be done afterwards [105].

For this transfer to be possible, one needs a geometry with optical access and good confinement, such as the planar geometry of the PPT. Also, the nanoparticle's charge [28, 29, 41] can be useful for approaching a PhC nanocavity: it would provide a handle for driving its motion electrically, or for applying a DC voltage to our sample to either attract or repel it from

its surface. Furthermore, a PPT can be an economical and useful trapping

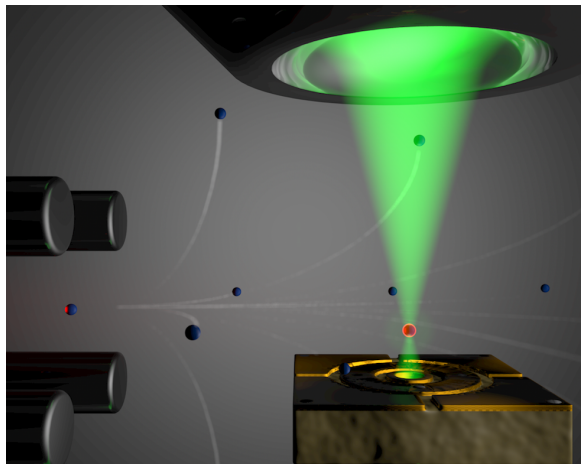

Figure 4.1: Image of the planar Paul trap experiment. A 4 metallic rod linear Paul trap loads charged 100 nm nanoparticles to a planar Paul trap that is interrogated with a 532 nm laser.

tool for charged specimens for optical interrogation, manipulation in different directions—if the PPT is placed on a xyz stage—and levitation over long periods of time.

We have developed a PPT for 3D manipulation of single charged polystyrene nanoparticles under ambient and atmospheric conditions. The trap enables stable confinement of the nanoparticle for days, it can be rotated throughout the full 360°, and we can also modify the trapping distance of the nanoparticle to the surface of the PPT. The main achievements and results of this work were published in APL, 2016 [91].

4.2 Experimental setup

Our PPT is made on a PCB (Printed Circuit Board) and is formed by two concentric electrodes with radii a (inner electrode) and b (outer electrode), and four corner compensation DC electrodes as shown in Fig. 4.2 a). This design features an empty central hole, providing optical access to the trapped specimen [147]. The electrical connections are made from the backside of the PCB. Both sides are connected via vertical conducting holes filled with alloy, keeping the topside clear for manipulation.

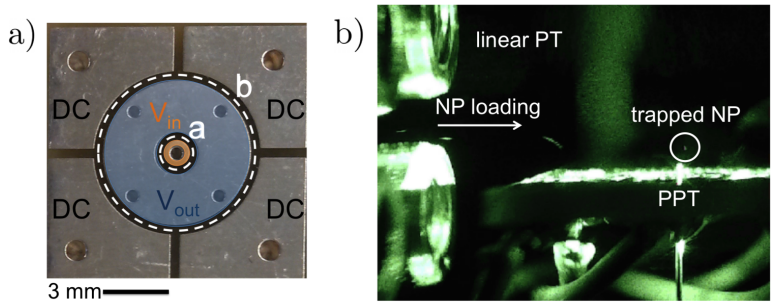

Figure 4.2: a) Description of the parts of the PPT on a PCB. The radii of the inner and outer electrodes is a and b, respectively. V_{in} and V_{out} corresponds to the voltage applied to the inner and outer electrodes. Our design includes compensation DC electrodes on the corners. All connections are on the backside of the PCB. b) Side view image of charged nanoparticles loading mechanism into the PPT from a linear Paul trap (four rods on the left of the picture).

To start with, we use a similar design to the one presented in ref. [87] with dimensions $a = 1.07$ mm and $b = 3.62$ mm (labeled as PPT_1 in the following). We used a suspension of 100 nm diameter polymer spheres dispersed in ethanol. The particles are charged with a homemade electrospray [148]. It is formed by a needle and a circular plaque with a hole where the needle is centered at. The nanoparticles are guided to the PPT with a linear Paul trap (see Fig. 4.2 b)) at an amplitude of 1000 V and a frequency of 800 Hz [87, 149].

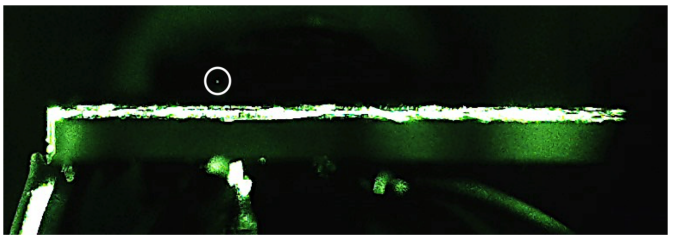

Figure 4.3: Side view of a PPT with a nanoparticle trapped circled in white. The nanoparticle is not centered because in each PCB there are 4 PPTs printed on the board but only one is connected.

The PPT is powered by two wave function generators (Tabor Electronics) and two high voltage amplifiers (Falco systems DC-5MHZ 50x and Trek 63B). In the simplest operation mode, only the outer electrode is driven by the RF signal (amplitude V_{out} of 340 V, frequency of 4 kHz) while, for now, keeping the inner electrode grounded. Figure 4.3 shows a side view scattering

picture from a single particle levitating in the PPT. The nanoparticle does not appear centered because there are 4 PPTs printed on the PCB but only one is connected. A four axis stage (x, y, z and θ), built with Arduino controlled motors and makeblock (robotic hardware), moves the PCB, and a 532 nm laser interrogates the trapped object. This light is focused to a 1.23 μm diameter spot size using a long working distance 50× (Olympus LMPLFLN) objective with NA= 0.5 placed above the PPT. The collected backscattered light propagates through a 45:55 beam splitter and is focused onto a CCD camera (see Fig. 4.4).

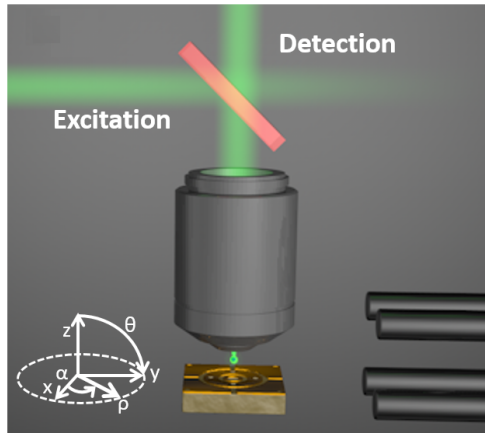

Figure 4.4: Schematics of the setup to measure the PPT's confinement. A 532 nm laser is focused through a 50x objective (0.5 NA). The scattered light is collected by the same objective for monitoring the nanoparticle's motion. We also show the linear Paul trap that allows us to load the PPT with charged nanoparticles.

The PPT compactness, along with its high trapping stability, enables unique manipulation capabilities that could not be achieved with optical tweezers. For instance, we demonstrate in Fig. 4.5 a) that the nanoparticle is kept trapped while rotating the PPT around its x axis. Further control over the trap features can be reached by applying an additional RF signal V_{in} of the same frequency (4 kHz) to the inner circular electrode. By varying $\epsilon = V_{\text{in}}/V_{\text{out}}$ [87] we are able to adjust the trapping height (see Eq. 4.3) [87, 150].

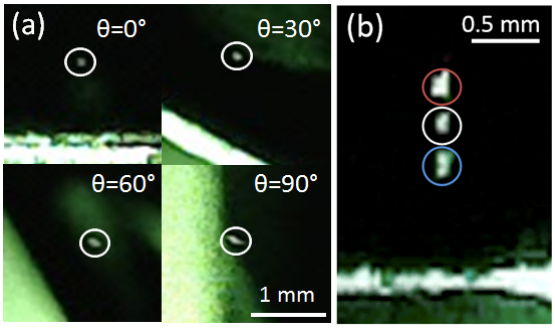

Figure 4.5: a) Mosaic of images taken from the side showing the manipulation of a single trapped nanoparticle with the PPT (0° to 90°). We can also rotated it throughout the full 360°. b) Superimposed images for three different ϵ values: $\epsilon = 0$ in white, $\epsilon > 0$ in blue, and $\epsilon < 0$ in red (see text).

Depending on the sign of ϵ, which is related to the phase difference between the two driving fields (this was controlled manually with the signal generators), the trapping height decreases ($\epsilon > 0$) or increases ($\epsilon < 0$) as shown in Fig. 4.5 b) and Fig. 4.6. The particle height depends on ϵ, which is plotted in graph Fig. 4.6 for two PPT designs. We show how much the height can be varied. The values of the height z_0 where taken directly from video images as ϵ was varied.

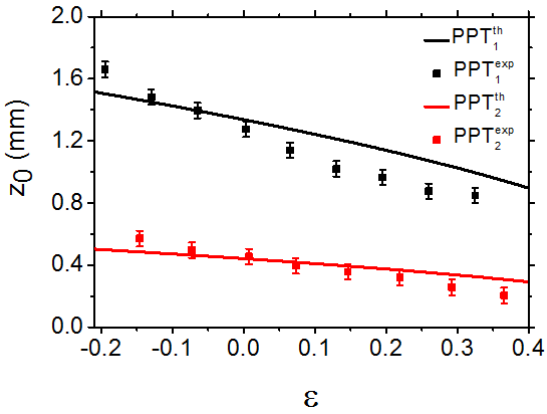

Figure 4.6: Experimental data for z_0 for different values of ϵ for both PCBs (points) and the corresponding theoretical predictions (solid lines) using equation (4.3). PPT_2 is the optimized design shown in section 4.3.

4.3 Planar Paul trap design optimization

The studied PPT geometry can be theoretically described using the model by Kim et al. [87], introduced in section 2.2. We now consider the general case where the inner and outer electrodes are powered with two AC fields of the same frequency. Using this model, we have optimized the trapping potential parameters in order to achieve both high confinement while maintaining PCB fabrication compatibility (smallest feature down to 0.125 mm). Given the cylindrical symmetry of our design, the electric potential created by our PPT can be properly described in cylindrical coordinates $\alpha = \tan^{-1}(y/x)$, $\rho = \sqrt{x^2 + y^2}$, and z. Trapping occurs at $\rho = 0$, resulting in the potential depending only on z. For a single trapped particle, its motion is typically described by a pseudopotential Ψ that accounts for the macromotion (slower oscillation that is not present in the overdamped regime [151]). In the absence of defects in the trap or a DC bias it is expressed as [87]:

$$\Psi(z, \rho, \epsilon) = A \mid \nabla\kappa(z, \rho, \epsilon) \mid^2, \tag{4.1}$$

where $A = \frac{Q^2 V_{\text{out}}^2}{4m\Omega^2}$, m and Q are the mass and charge of the particle, and V_{out} and $\Omega = 2\pi f$ correspond to the amplitude and angular frequency of the AC field applied to the outer electrode, respectively. All the parameters of the trapped object and the signal applied to the PPT are contained in A, except for V_{in}, which determines the trapping position along z. Therefore, we can define a normalized pseudopotential $\bar{\Psi} = \Psi/A$. The spatial dependence of the pseudopotential is given by $\kappa(z, \rho, \epsilon)$, containing Bessel functions, and simplifies to $\kappa(z, \epsilon)$ at $\rho = 0$, where the trapping occurs (similar to equation (2.27) but for two ring electrodes):

$$\kappa(z, \epsilon) = \frac{1 - \epsilon}{\sqrt{1 + \left(\frac{a}{z}\right)^2}} - \frac{1}{\sqrt{1 + \left(\frac{b}{z}\right)^2}} + \epsilon. \tag{4.2}$$

In vacuum, stable solutions to the equation of motion of the trapped object exist if the condition $\mid q \mid \leq 0.9$ is satisfied [64]. In the presence of damping, like in our ambient pressure experiments, stable trapping typically occurs at higher q values [152, 153]. The pseudopotential's critical points are the minimum z_0 and the turning-point $z_{\max}$:

$$z_0 = \sqrt{\frac{b^2 a^{4/3}(1-\epsilon)^{2/3} - a^2 b^{4/3}}{b^{4/3} - a^{4/3}(1-\epsilon)^{2/3}}}, \tag{4.3}$$

$$z_{\max} = \sqrt{\frac{b^2 a^{4/5}(1-\epsilon)^{2/5} - a^2 b^{4/5}}{b^{4/5} - a^{4/5}(1-\epsilon)^{2/5}}}, \tag{4.4}$$

which only depend on the geometry of the PCB, and in particular are independent of the damping. The trap depth is defined as $D = \Psi(z_{\max}) - \Psi(z_0)$.

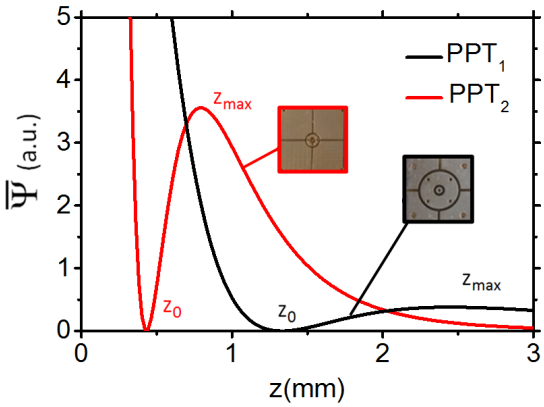

Figure 4.7: Theoretical calculation of the pseudopotential $\bar{\Psi}(z)$ for both PCBs. We found $z_{0,1} = 1.33$ mm, $z_{\max,1} = 2.45$ mm, $z_{0,2} = 0.44$ mm, and $z_{\max,2} = 0.78$ mm.

To attain a higher trap confinement, we numerically determined the optimum geometrical parameters that yield to a maximum pseudopotential depth D while accounting for the manufacturing limits (imposing $a > 300$ μm). From equations (4.1) and (4.2), we simulated the pseudopotential for different values of a and b, with $a < b$. Under these constraints, the most confined pseudopotential is obtained for $a = 0.36$ mm and $b = 1.17$ mm (labeled as PPT_2 in the following). The simulated pseudopotentials and their dependence on z for both geometries are presented in Fig. 4.7. Using equations (4.3) and (4.4) we determined the depth of the trap $\bar{D} = \bar{\Psi}(z_{\max}) - \bar{\Psi}(z_0)$ in arbitrary units. From Fig. 4.7, we see that PPT_2 has a trap depth $10\times$ greater than PPT_1.

4.4 Results

Based on the theoretical calculation from the previous section, we tested experimentally the optimized design (PPT_2) and compared it to the original one (PPT_1). We recorded, through the optical objective, videos of the trapped particle (acquisition area 30 μm $\times$ 30 μm at a rate of 15 frames/s) that were converted into an image sequence for analysis. Although the integration time of the camera is longer than the oscillation period of the nanoparticle, and therefore it is not possible to exactly determine its spacial confinement within the trap, a time average of a video with $\sim$ 400 frames confirms that PPT_2 features much better confinement (Fig. 4.8 a) and b)),

in agreement with the predictions shown in Fig. 4.7 . The image acquired from PPT_1 demonstrates that the particle explores a large region away from the focal spot, with scattering from the particle covering the full field of view (note that the background color is different from zero). On the contrary, the image obtained with PPT_2 shows the nanoparticle strongly confined to a region of few microns.

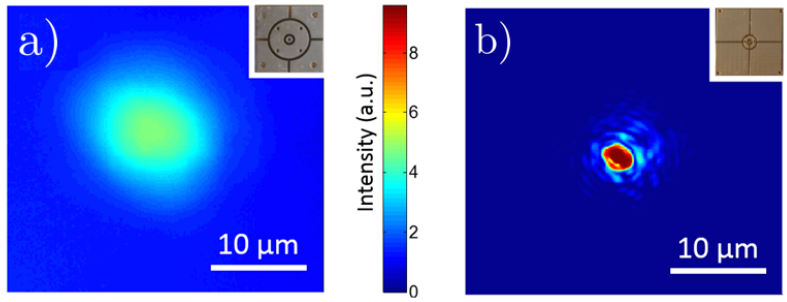

Figure 4.8: Temporal averaging of 372 frames for PPT_1 and PPT_2 in a) and b), respectively. The scale bar represents 10 μm and the color bar is the same for both images. The resolution of the camera is 0.1 μm/px.

To get further insight in the dynamics of the particle in PPT_2, we implemented a position detection scheme similar to those routinely used in optical tweezers [121]. The trapped nanoparticle was illuminated with a 10× objective (NA= 0.25) leading to a spot size $\simeq$ 2.6 μm of 20 mW, to ensure that we observe the full trajectory of the trapped nanoparticle. The backscattering signal from the nanoparticle was measured through the same objective and sent to a quadrant photodetector (QPD). From the time trace for each axis, we extracted the particle position histograms shown in Fig. 4.9 a). The two outer maxima indicate a driven oscillation of the particle. The corresponding power spectral density (PSD) shows a dominating peak at 4 kHz—driving frequency of the PPT—as well as higher harmonics (see Fig. 4.9 b)). Higher harmonics indicate a quasi-harmonic behavior of the particle inside the trap. We estimated the confinement by fitting the low frequency part (up to 1 kHz) of the PSDs to an overdamped Lorentzian, similar to what is done in optical tweezers [154]. Assuming the validity of the equipartition theorem of the nanoparticle in the pseudopotential, we obtain the calibration factor from volts to nanometers for each axis. Our estimated confinement is consistent with the observations in Fig. 4.9 a), where the particle's trajectory is about 4 μm in all directions.

The measurements that are shown in Fig. 4.9 were very challenging since

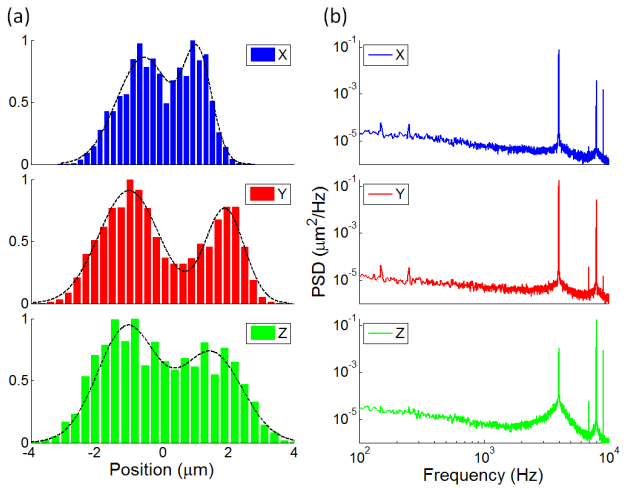

Figure 4.9: a) Normalized position histogram of nanoparticle in PPT_2. The two maxima indicate a driven harmonic motion. Black lines are a guide to the eye. b) Power spectral density. We observe the driving frequency at 4 kHz and higher harmonics.

the optical forces modify the nanoparticle's trajectory even with low powers, creating a dimple potential [155]. This is why we selected a low NA objective and conducted the measurements at low optical powers. We observed a clear trapping effect with 1064 nm light on the nanoparticle's trajectory at 42 mW with the 50× objective (0.5 NA): the two-sided histogram of Fig. 4.9 starts to look asymmetric as shown in Fig. 4.10. This asymmetry increases for higher optical power, probably because of a misalignment between the center of the Paul trap and the laser beam's focus.

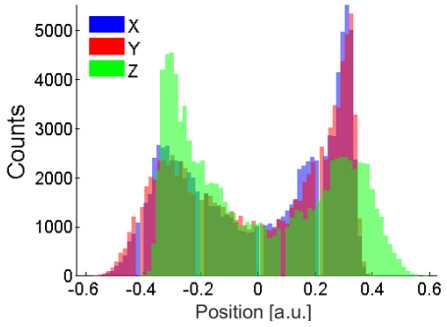

Figure 4.10: Example of asymmetry appearing in the nanoparticle's dynamics for 42 mW of a 1064 nm laser probe.

4.5 Conclusions and outlook

One of the main motivations to work with a Planar Paul Trap (PPT) is to levitate objects that would otherwise burn in optical tweezers, as well as to explore a possible controlled nanoparticle loading mechanism to the optical tweezer. For instance, a charged particle could be transferred from the PPT to an optical tweezer and then brought close to a photonic crystal nanocavity. The most common particle loading method in levitodynamic's experiments are nebulizers, mechanism which forces us to open the vacuum chamber each time one needs to load a particle.

To achieve this transfer, one needs a geometry with optical access, such as the planar geometry of the PPT. Also, the nanoparticles' charge [28, 29, 41] can be a useful handle when approaching a device or surface with a given voltage difference. Furthermore, a PPT can be an economical and useful trapping tool for charged specimens for optical interrogation, manipulation in different directions—if the PPT is placed on a xyz stage—and levitation over long periods of time.

We have developed a PPT for 3D manipulation of single charged polystyrene nanoparticles under ambient conditions. The trap enables stable particle confinement $\sim 4\mu$m along each axis, it can be rotated throughout the full 360°, and we can even modify the trapping distance of the nanoparticle to the surface of the PPT. We have also shown, that if the optical power for detection is increased, it also affects the dynamics of the trapped specimen. This integrated and adaptable system provides a tool for contamination sensitive "on-a-chip" levitodynamical experiments.

Chapter 5

Design, fabrication, and characterization of the photonic crystal nanocavity

In this chapter we describe the different building blocks of the nanocavity's experimental setup. We will start with the design and fabrication of the photonic crystal (PhC) nanocavity, and then discuss how it interacts with the nanoparticle. Finally, we will explain the optical trapping scheme, and the techniques to excite the nanocavity and detect the levitated nanoparticle through it.

5.1 Introduction

In the last 15 years, optical cavities in optomechanical systems have been miniaturized. The trend of aiming for lower masses and dimensions is not a mere coincidence: it is because of how the cavity mode volume V_c relates to the strength of the fundamental optomechanical interaction $g_0 \propto \frac{1}{V_c}$. An increase in g_0 allows to obtain more information per photon from the oscillator's motion and from the forces that act upon it. Also, a high optical $Q = \frac{\omega_c}{\kappa}$ factor, equivalent to a small linewidth κ of the optical oscillator, makes the system more sensitive to variations in frequency ω_c. One option to achieve this high Q/V_c is with photonic crystal nanocavities, like the ones presented in this work.

5.2 Nanocavity design and simulation

In this section, we will go through the design of the grating couplers and the PhC nanocavity. Also, we will discuss the different PhC designs and their corresponding simulations. Finally, we will outline the main optical characteristics of the PhC and describe its expected optomechanical performance in the context of levitodynamics.

5.2.1 Grating couplers

Up until now, we have only introduced theoretically the two main protagonists of the experiment: a levitated nanoparticle and a 1D photonic crystal cavity. For an optomechanical interaction to exist between them, first of all, the nanocavity must have light propagating through it, so that its near-field can interact with the levitated object. Therefore, we need to couple light into—and also out from—the device. One option for coupling light is end-fire coupling, where radiation coming from an optical fiber propagates into one of the facets of a photonic waveguide. Although the efficiency can be very high (from a predicted 90% to 96% including embedded v-grooves on a waveguide [156, 157]), it has very poor tolerance to misalignment. A similar option is a nanotaper coupler (85% efficiency [158]), where a very narrow taper is created at the facet of the waveguide that spatially extends the propagating mode; prism couplers also offer high efficiencies (over 90% [159]). Other works [120] glued a fiber tip to the photonic structure (32% efficiency), but it is also possible to directly couple light into the waveguide from free-space with a grating coupler.

A grating coupler consists of a periodically modified or etched material, that creates a diffraction grating to provide constructive interference of light in an out-of-plane direction. In this work, we have used this technique to couple free-space light into an on-a-chip photonic waveguide because it is easy to implement and fabricate [160, 161]. In the following, we will provide an intuitive ray optics explanation of how grating couplers work. A more detailed description can be found in [162].

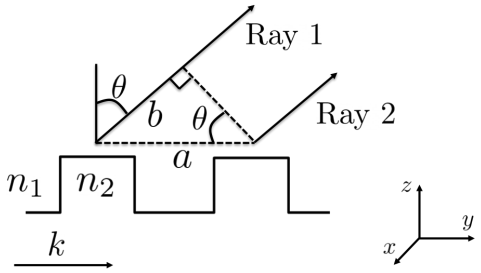

Figure 5.1: Two rays reflected off adjacent periods (distance a) at angle θ: Ray 1 and Ray 2. The difference in path between the two rays is b. The grating is built in a material with index of refraction n_2 surrounded by air (n_1). The propagation vector of light is given by k.

Let us consider light of wavelength λ traveling through a waveguide that reaches the grating, where light exits at a certain angle θ (see Fig. 5.1). The grating has rectangular grooves of period a on an etched material of index of refraction n_2, surrounded by air (index of refraction n_1). Our goal is to choose a so the electric field constructively interferes for a given angle θ. Therefore, we must find the dependency between both parameters.

In Fig. 5.1, we have two exiting rays, ray 1 and ray 2, at wavelength λ, that constructively interfere at θ. We also define a distance b, which is the difference in length between the path of the two rays. For constructive interference to happen, we need the phase difference of ray 1 and ray 2 to be $2\pi m$, where m is an integer number:

$$
\begin{aligned}
k_2 a - k_1 b &= 2\pi m \text{ for } \; m = 0, \pm 1, \pm 2, \\
\frac{2\pi}{\lambda} n_{\text{eff}} a - \frac{2\pi}{\lambda} n_1 b &= 2\pi m, \\
n_{\text{eff}} a - n_1 b &= m\lambda, \\
n_{\text{eff}} a - n_1 a \sin(\theta) &= m\lambda, \\
\sin(\theta) &= \frac{m\lambda - n_{\text{eff}} a}{-n_1 a},
\end{aligned}
\tag{5.1}
$$

where $k = \frac{2\pi}{\lambda} n$ is the propagation vector, n_{eff} lies between n_1 and n_2 and quantifies the phase delay per unit length in the waveguide, relative to the phase delay in vacuum. In the special case of $\theta = 0$, and considering $m = 1$, we obtain $a = \lambda / n_{\text{eff}}$. Then, a good initial guess for a target wavelength λ would be $a = a_{n_1} + a_{n_2}$, where $a_{n_1} = \lambda / 2n_1$ and $a_{n_2} = \lambda / 2n_2$ [163].

Our grating couplers' design is inspired by [160, 161] (see Fig. 5.2), which demonstrated out-coupling efficiencies of 50 % and 53% where the

design includes a reflecting substrate underneath. In contrast, the input coupling efficiency into the allowed propagation mode of the waveguide was $\sim$ 16% [161]. This geometry has the advantage of being compatible with fabrication on a membrane with just one lithographic step. The coupler, pictured in Fig. 5.2, has 3 periods and a semi-circular shape; more periods do not significantly increase the coupling efficiency [161], and the semi-circular shape reduces losses in a compact way [164]. Because of the symmetry in the design, the vertical scattering of light is identical for both $+z$ and $-z$ directions.

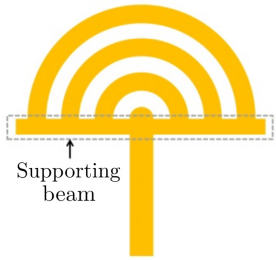

Figure 5.2: Design from [161] with 3 periods and semicircular shape.

In our experiment, we use two identical couplers for the nanocavity's input and output, where the filling factor and periodicity have been optimized to efficiently couple light throughout the full range of our tunable 1550 nm laser (1515-1575 nm). We measured an output coupling efficiency of $\sim$ 15%. We have drawn the couplers into the sample with the same procedure that we follow for the photonic crystal cavity (see Appendix C).

5.2.2 Initial nanocavity design

The first design for the PhC nanocavities was developed by M. López from Darrick Chang's group at ICFO. It was obtained through finite-difference time-domain (FDTD) simulations in Lumerical, a simulation software designed for photonics. These simulations provided, for a target resonance wavelength of 1550 nm, the initial geometrical parameters of the 1D photonic crystal cavity: waveguide thickness t, width w, period Λ, smallest defect period Λ_0, rectangular width h_x and length h_y (see Fig. 5.3). From there, except for the thickness—fixed by the characteristics of our samples—we tuned the other parameters and optimized the structure. Our goal was to obtain a cavity mode within the range of wavelengths compatible with our excitation laser, and maximize Q while, at the same time, enough evanescent

field would leak out of the cavity, for the optomechanical interaction with the particle to take place.

The design (see Fig. 5.3) has 2 different sections:

1. Mirror section: series of unit cells with constant periodicity Λ. They create the band gap.
2. Defect section: series of unit cells with a quadratic variation in the periodicity, which allows to localize light of a specific wavelength at the center of the structure. Such wavelength will set the resonance of the PhC nanocavity.

These sections are ordered as mirror cells, defect cells, and mirror cells again as shown in Fig. 5.3.

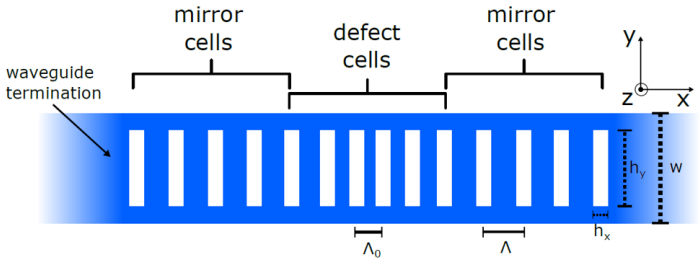

Figure 5.3: PhC nanocavity design with smallest period Λ_0, mirror cell period Λ, waveguide width w, rectangle width h_x and length h_y.

We place 20 mirror cells at each side to ensure a high Q-factor, and, for the defect, a quadratic decrease in the period, from Λ to $\Lambda_0 = 0.93\Lambda$. The expression of the distance between consecutive defect cells is:

$$\Lambda_{n=1,2,3...,D} = \Lambda_0 + 0.01(\Lambda - \Lambda_0)\left(n - \frac{(\mathrm{D}+1)}{2}\right)^2,$$

where D corresponds to the number of defect cells. The number of mirror cells affects the Q and λ_{res} of our optical resonator, as shown in Fig. 5.4.

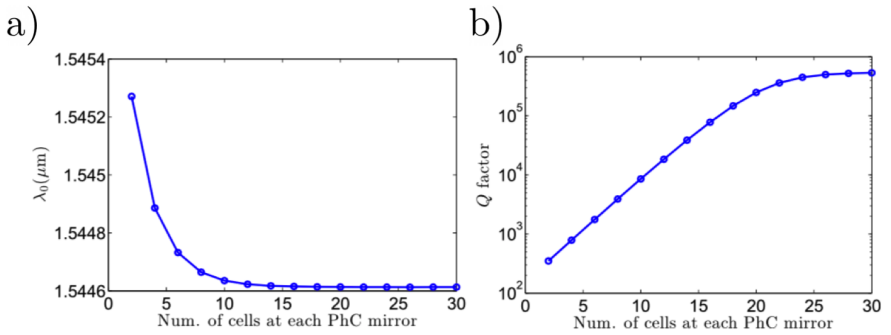

Figure 5.4: FDTD Lumerical simulation: optimization of the number of cells of each PhC mirror for λ_{res} and Q. (a) Variation of λ_{res} with number of PhC mirror cells. The resonant wavelength λ_{res} remains almost invariant when the number of mirror unit cells is increased above 10. (b) Variation of the Q-factor with number of PhC mirror cells. The Q-factor saturates to a value given by the scattering losses produced by the defect.

5.2.3 Dielectric mode nanocavity design

The FDTD simulations in Lumerical assumed an oscillating dipole as a source of light at the center of the PhC nanocavity. However, this does not represent our experiment fairly: we input light through one end of the waveguide and detect the output signal from the other end. To simulate our experiment, the nanocavity PhC design has also been modeled with COMSOL (a finite element method commercial simulation software) by Dr. A. Cuadrado [165]. In this case we have included an input and an output port to introduce and detect radiation, respectively. In the simulation, we have accounted for a boundary mode analysis to obtain the modes that are allowed to propagate through the waveguide. Afterwards, we performed a scan in frequency to obtain the transmission and reflection response of the device. We considered the material-air boundary by including a scattering condition; prohibiting reflections from the transversal radiation.

In Fig. 5.5, we show the PhC on resonance for a number of defect cells $D = 11$ and we included silicon nitride's index of refraction $n = 2.129$ for $\lambda = 1550$ nm (value provided by the manufacturer).

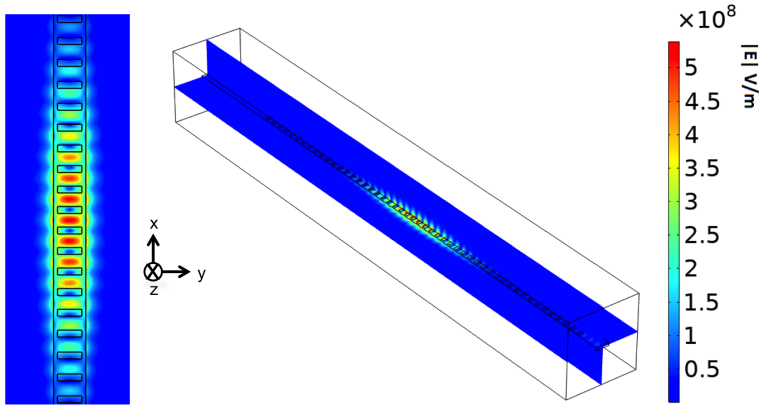

Figure 5.5: COMSOL simulation of the fundamental mode nanocavity on resonance for $D = 11$. This design has a $Q = 55000$. The nanocavity's width is 950 nm.

Once we fabricate the nanocavities, we measure their geometrical dimensions with a scanning electron microscope (SEM). This way, we can introduce the experimental dimensions into the COMSOL model for comparison. The simulation shown in Fig. 5.5 considered $w = 950$ nm, $h_x = 200$ nm, $h_y = 715$ nm, $\Lambda = 643$ nm, and $\Lambda_0 = 600$ nm. We obtained a simulated $Q = 55000$ for the nanocavity with its resonance centered at $\lambda_{\text{res}} = 1539.16$ nm (see Fig. 5.6). The value of the simulated Q is calculated from the transmission of the simulated nanocavity for a given wavelength input. The simulated resonance value usually varies within 5 nm from the experimental one. Also, to experimentally achieve our target λ_{res} within our laser range of 1510–1575 nm, we slightly alter the period and vary the dose in the lithography step during fabrication (i.e. time that the structure is being exposed by the electron beam for a fixed beam current). In practice, we typically measure an experimental quality factor of $Q \approx 5000 - 10000$. This is due to limitations in current fabrication techniques: minor defects in the photonic crystal structure will decrease the quality factor of the nanocavity. It is common to observe an order of magnitude decrease in Q between the simulated structure and the fabricated one.

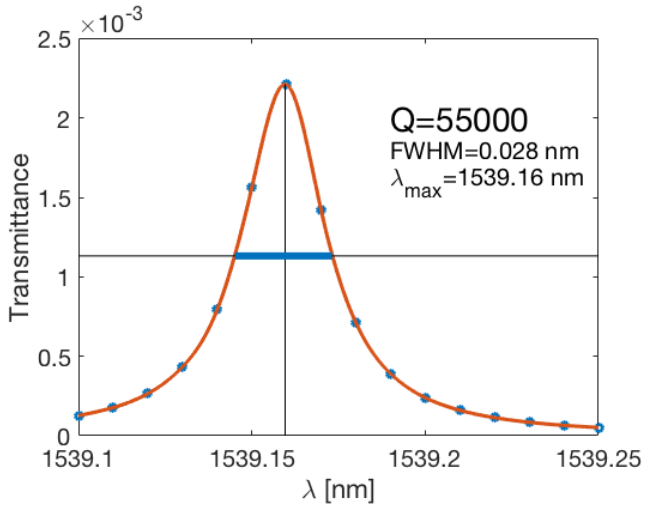

Figure 5.6: Simulated spectral transmittance of the nanocavity close to resonance. Q is obtained from the simulation in Fig. 5.5. Also, the resonance peak is not centered because of the available points from the simulation.

By performing the simulations previously shown, we also found that, by increasing the number of defect cells to $D = 19$ and keeping the rest of the parameters constant we were able to excite the second cavity mode (see Fig. 5.7) in a similar wavelength range. Engineering the PhC cavity in this way could allow for detection of two levitated nanoparticles (see section 7.4.1).

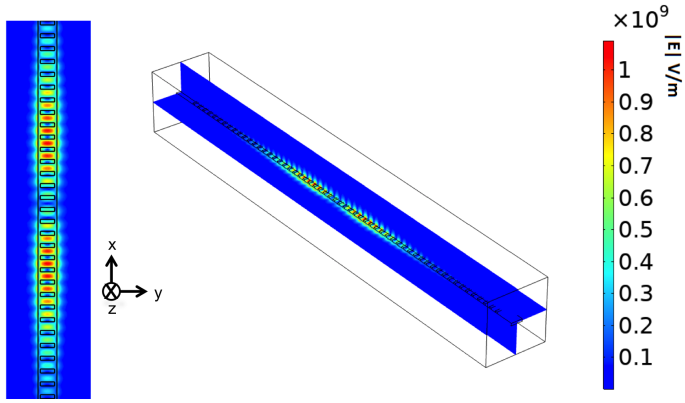

Figure 5.7: COMSOL simulation of the nanocavity's second mode on resonance. For this case, we obtained a $Q = 31000$ and a resonance wavelength of 1569.21 nm. The nanocavity's width is 950 nm.

This second mode of the cavity appears in the wavelength range of our tunable laser and, depending on the fabrication, we sometimes find both (the fundamental and second cavity mode) resonance peaks in this second mode dielectric mode design as shown in Fig. 5.8. However, for this design where $D = 19$, the fundamental mode has a lower transmission and often times it is not visible.

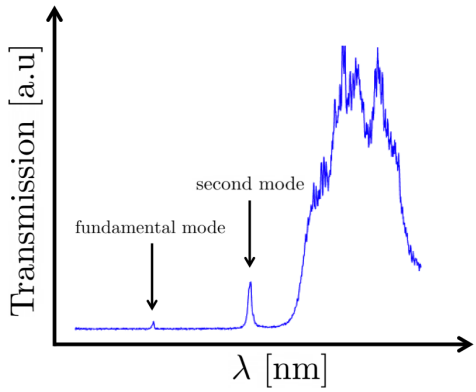

Figure 5.8: Experimental spectra of the nanocavity's second mode design. We see two peaks marked with an arrow: the one at lower wavelengths corresponds to the fundamental mode (1 area where the electric field concentrates) and the peak at higher wavelengths corresponds to the second mode of the nanocavity (2 areas where the electric field concentrates).

5.2.4 Air mode nanocavity design

As it will be discussed in detail in chapter 6, micro- and nanocavities heat up when they are excited on resonance because of the absorbed power from the intra-cavity light and poor heat dissipation due their to their small volumes. This often results in shifts of the resonant wavelength, which prevents a stable intra-cavity field, and therefore an effect we aim to minimize. This is why we implemented an alternative PhC design that supports the air mode instead of the dielectric mode (see section 3.1). In the case of an air mode cavity, most of the electromagnetic energy concentrates at the nanocavity's holes, where there is air instead of silicon nitride as shown in Fig. 5.9. In these simulations provided by Dr. Gomis-Bresco (from ICN2 in Barcelona), we kept the period Λ constant, and the defect is created by a cubic variation of the height of the rectangles h_y.

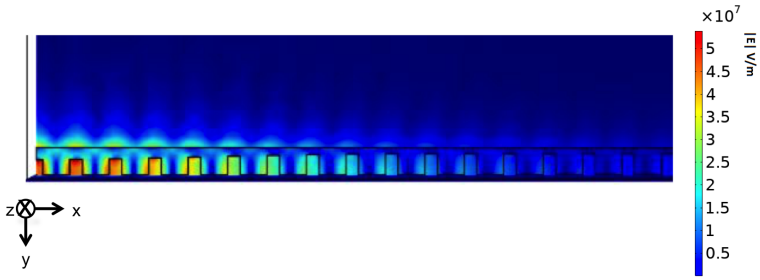

Figure 5.9: COMSOL simulation for air mode PhC nanocavity (performed by Dr. J. Gomis-Bresco). This image just shows 1/4 of the central part of the PhC. The nanocavity's total width is 942 nm.

The parameters we used were: $\Lambda = 710$ nm, $w = 942$ nm, $h_x = 218$ nm, $h_y = 720$ nm and a thickness of 200 nm. The defect is formed by 17 cells with decreasing h_x from 720 nm to 520 nm (at the center) and back. The height of the rectangles in the defect can be described by the cubic polynomial:

$$h_x = -0.4321D^3 + \frac{50}{9}D^2 + \frac{65}{9}D + 520, \tag{5.2}$$

where $D = 0, 1, ..., 8$ is the defect cell number, counting from the center of the defect region. This simulation also considered a rounded fillet for the rectangles, because experimentally it is impossible to get a perfect right angle through electron beam lithography.

5.2.5 Characteristics of the full PhC nanocavity

Before going through how the nanocavities are fabricated and their characterization, we provide a brief description of how each component of the structure contributes (see Fig. 5.10 a)) to its transmission spectrum (see Fig. 5.10 b)). Light is coupled in and out of the nanobeam through two identical grating couplers by means of a 100× objective. By coupling a super-continuum light source into the input coupler (left) and sending the light from the output coupler (right) into a spectrometer, we obtain the spectra shown in Fig. 5.10 b). They correspond to the light transmitted by three different devices:

1. A waveguide with grating couplers, with the latter shown in red in 5.10 a).
2. A waveguide with grating couplers plus a photonic crystal made only of mirror cells, with the latter shown in green in 5.10 a).
3. A waveguide with grating couplers plus a photonic crystal with a defect part (cavity), with the latter shown in blue in 5.10 a).

In Fig. 5.10 b), the red spectrum shows the full transmission through the waveguide. In green, we can see the creation of a band gap. When including the defect, we see a modification in the band gap that allows a cavity mode to propagate through the PhC cavity, with a peak at ~ 1550 nm (blue curve). This resonance is the one that we will use in our levitodynamics experiments.

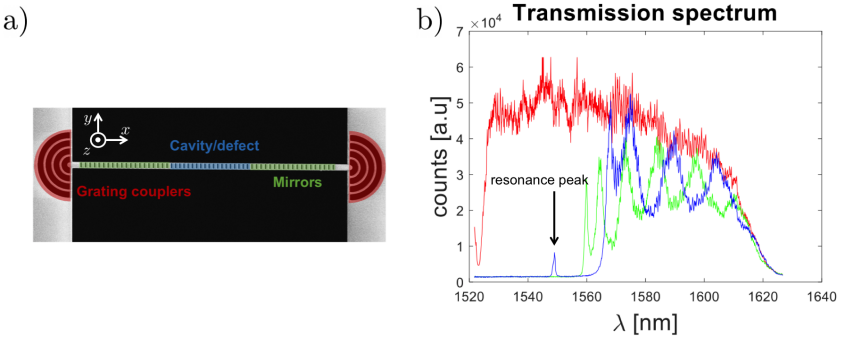

Figure 5.10: a) SEM image with marked parts that make up the device: cavity/defect, mirrors, and grating couplers. b) Spectra of the contribution of each element. The nanocavity's resonance peak is marked with an arrow.

5.2.6 Optomechanical performance of the nanocavity

For the dielectric mode designs previously discussed, we have numerically estimated the optomechanical coupling factor g_0. To do so, we position a 235 nm sized nanoparticle at a certain distance away from the nanocavity. The coordinates defined for our system are: $x = 0$ is the point where the electric field is maximum along the nanobeam, $y = 0$ and $z = 0$ correspond to the center of the nanobeam in each direction (as shown in Fig. 5.11 and Fig. 5.12), where the nanobeam is 1 micron wide and 200 nm thick. Note that the nanocavity does not provide a trapping field for the nanoparticle, its near-field interacts and couples with the levitated object. In the following, the coordinates will be given for the position of the center of the nanoparticle. We have completed the calculation both with the Lumerical simulations and with the COMSOL model [165].

Lumerical simulation

We extract the optical frequency shift per displacement $G_{x_i} = \frac{\partial\omega(x_i)}{\partial x_i}$ of a dielectric fundamental mode nanocavity with the Lumerical simulations for different positions of the nanoparticle. In our experiment we approach the nanoparticle to the nanocavity from the side along the y direction, and in the following, we assume $x = z = 0\,\mu$m. Thus, we place the nanoparticle 500 nm away surface-to-surface distance in the y-axis, such that the nanoparticle's center is at $(x = 0, y = 1.1175, z = 0)\,\mu$m as shown in Fig. 5.11. The nanoparticle will oscilate with an amplitude of ~ 50 nm [1] around this point.

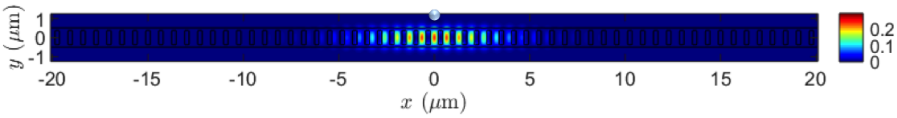

Figure 5.11: Lumerical simulation of the normalized electric field of the PhC nanocavity. The nanoparticle's surface (light blue circle) is 500 nm away from the PhC surface along the y direction. The position of the center of the nanoparticle is at $(x = 0, y = 1.1175, z = 0)\,\mu$m.

If we zoom in on the unit cell in which the nanoparticle is close by, we obtain the situation displayed in Fig. 5.12.

[1] 50 nm is a typical oscillation amplitude for a levitated particle in vacuum. This is later shown in chapter 7.

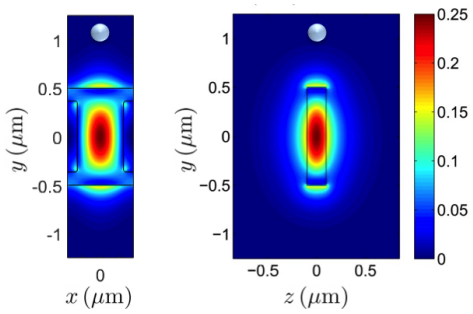

Figure 5.12: Left: zoom of Fig. 5.11 on the central unit cell with the nanoparticle (light blue circle). Right: cross-cut on the same unit cell along the YZ plane. The position of the center of the nanoparticle is at $(x = 0, y = 1.1175, z = 0)\,\mu$m.

Hence, we extracted the normalized field intensity profile along this direction, $f(y)$, and plotted it in Fig. 5.13.

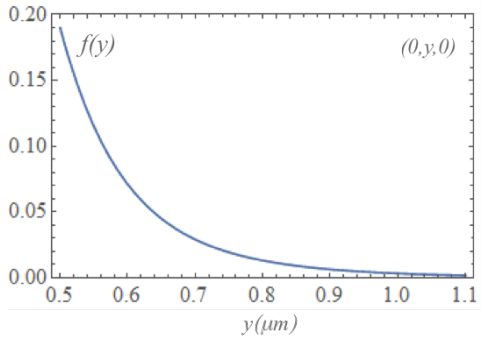

Figure 5.13: Cross-cut of the intensity profile $f(y)$ along the approaching direction y ($x = z = 0$ μm) for the nanocavity excited on resonance ($\lambda_{\text{res}} \sim 1.55$ μm).

From the intensity mode profile $f(y)$ calculated with the Lumerical simulation, we estimated G_y by using perturbation theory [116]:

$$G_y = \left| \frac{\partial \omega_c(y)}{\partial y} \right| \approx \frac{1}{2} \frac{\alpha \omega_c}{\epsilon_0 V_m} \frac{\partial f(y)}{\partial y}, \tag{5.3}$$

where $\alpha = 10^{-32}$ m^2/F is the polarizability of the particle, $\omega_c = 194.1$ THz is the resonance frequency, ϵ_0 is the electric permitivity in vacuum, $V_m \sim 10^{-18}$ m^3 is the nanocavity's mode volume, and $\frac{\partial f(y)}{\partial y}$ is the derivative of the normalized intensity profile $f(y)$ from Fig. 5.13.

Then, substituting the constants and parameters in equation (5.3), we obtained $G_y = 2\pi \cdot 7.86$ MHz/nm for a nanoparticle located at $(x = 0, y =$

$1.1175, z = 0)\,\mu$m which corresponds to the green circle in Fig. 5.14. The coupling G_y can be calculated for different y positions of the nanoparticle (see Fig. 5.14). If the nanoparticle is 300 nm away, $(x = 0, y = 0.9175, z = 0)\,\mu$m, then $G_y = 2\pi \cdot 30$ MHz/nm (see red circle in Fig. 5.14).

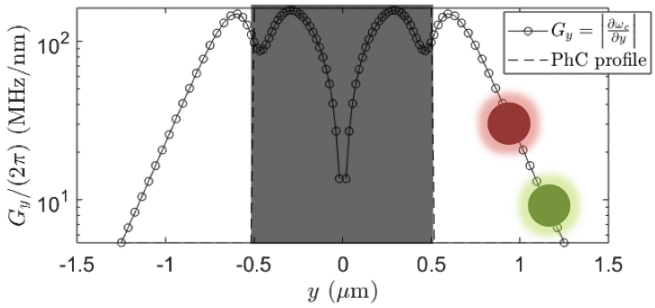

Figure 5.14: Optical shift per displacement for a silica nanoparticle of 235 nm diameter and a nanocavity of $Q = 2.5 \cdot 10^5$. The shaded region indicates the nanobeam's width (area inaccessible for the nanoparticle). The red and green circles represent the nanoparticle at 300 nm and 500 nm surface-to-surface distance away from the nanocavity, respectively.

This calculation can be performed in the same way for the x and z directions. By setting $z = 0\,\mu$m, and $y = 1.175\,\mu$m, we moved the nanoparticle along x and found values up to $G_x = 2\pi \cdot 3.4$ MHz/nm for $x = 0.15\,\mu$m. Finally, for z, we placed the nanoparticle at $(x = 0, y = 1.1175, z = 0.3)\,\mu$m, which lead to a $G_z = 2\pi \cdot 1.6$ MHz/nm.

To obtain the corresponding per photon displacement optomechanical coupling g_{0,x_i}, we multiplied G_{x_i} by the $x_{\mathrm{ZPF}} \approx 10^{-3}$ nm. For x and y, we obtained $g_{0,x} \approx 2\pi \cdot 3.4$ kHz, $g_{0,y} \approx 2\pi \cdot 7.86$ kHz for 500 nm away, and $g_{0,y} \approx 2\pi \cdot 30$ kHz for 300 nm away; while for z, $g_{0,z} \approx 2\pi \cdot 1.6$ kHz.

COMSOL simulation

We have also calculated g_0 from the COMSOL simulations [165] where the nanoparticle is 300 nm and 350 nm away surface-to-surface distance from the nanobeam along y. This simulation considers the same model as the one shown in section 5.2.3. In this case we have estimated g_0 via the nanocavity's resonance shift obtained for a given particle's position. We considered the dielectric second mode nanocavity design with $Q = 31000$ (see section 5.2.3) which we use for our levitodynamics experiment in chapter 7. We will use the same coordinate system as before, but where $x = 0$ μm corresponds to the maximum field intensity along x for one of the two intensity maxima.

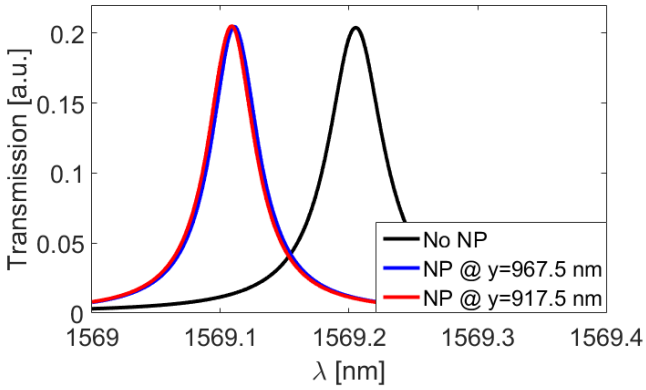

Figure 5.15: Simulation of the nanocavity resonance with and without nanoparticle close to its surface. There are two cases with the nanoparticle at different positions along y (the cavity's resonance is around 1569.1 nm).

In Fig. 5.15 we observe a 0.1 nm resonance shift of the nanocavity's resonance due to the presence of a nanoparticle with a diameter of 235 nm compared to no nanoparticle at all. The nanoparticle is placed at two different positions along the y axis: 300 nm ($y = 917.5$ nm) and 350 nm away ($y = 967.5$ nm) from the edge of the nanocavity. As we've mentioned, we place the nanoparticle close to one of the two maxima of the nanocavity along x. If for Fig. 5.15 we zoom in on the resonance peaks where there is a nanoparticle in the vicinity of the nanocavity, we obtain Fig. 5.16.

We have considered two y positions of the levitated particle, that if substracted result in a total displacement of $\Delta y = 50$ nm[2], which provides a shift in the resonance wavelength $\Delta\lambda = 2$ pm, which corresponds to $\Delta f = 243.73$ MHz. If we recall from section 2.3.1, we can estimate G_{x_i}:

$$G_{x_i} = \frac{\partial \omega_c(x_i)}{\partial x_i} \approx \frac{2\pi \Delta f}{\Delta x_i} \tag{5.4}$$

To evaluate g_0, we multiplied G_{x_i} from expression (5.4) by $x_{\mathrm{ZPF}} \approx 10^{-3}$ nm and obtained $g_{0,y} = 2\pi \cdot 3.6$ kHz.

Although the order of magnitude of g_0 is the same, this last $g_{0,y}$ value is smaller compared to the one in the Lumerical simulation for the same position of the nanoparticle. However, the COMSOL simulations are in closer representation to what we do in the laboratory. We believe that the deviation in g_0 is due to the different modeling considerations and possible

[2]50 nm is a typical oscillation amplitude for a levitated particle in vacuum. This is later shown in chapter 7.

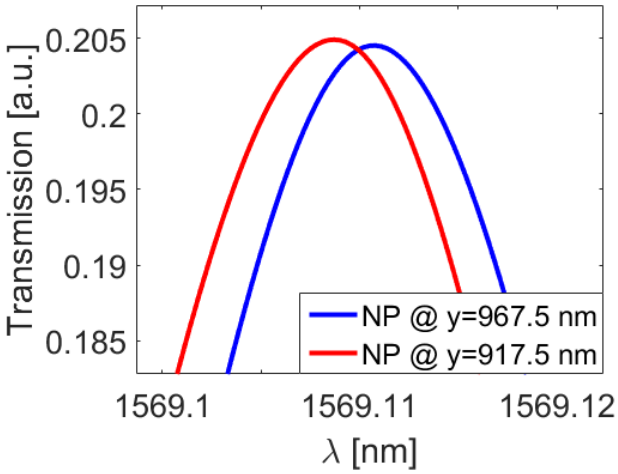

Figure 5.16: Zoom in of the resonance with the nanoparticle at two different locations along y.

dissimilarities in the intensity field profile of the nanocavity. Nevertheless, for both simulations, the values of g_0 are three order of magnitudes larger than in macro-cavity experiments [120].

5.3 Fabrication of nanocavities

We will now describe the fabrication procedure of the PhC nanocavities, starting from their drawing and up to the final imaging characterization with the scanning electron microscope (SEM).

We fabricate our nanocavities on commercial Si_3N_4 membranes from Norcada (reference NX5050D). The Si_3N_4 membrane is 200 nm thick and is supported on a 5×5 mm^2 Si frame with a 0.5×0.5 mm^2 window, where the Si_3N_4 is suspended. All the nanocavities are drawn on the suspended area of the membrane. The fabrication process consists in electron beam lithography—to draw the desired pattern—which is followed by reactive ion etching (RIE)—to etch Si_3N_4 and the left-over resist. A summary of the entire fabrication process is shown in Fig. 5.17.

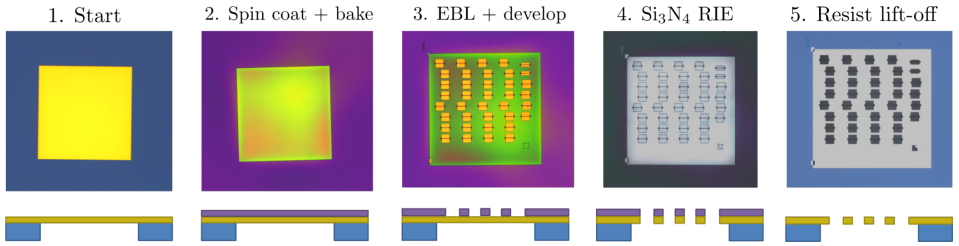

Figure 5.17: Summary of the fabrication process. Si_3N_4 window is 0.5×0.5mm. Top row: optical microscope image of the sample. Bottom row: side view cross-cut diagram. 1) Sample before any fabrication step (yellow square side is 500 μm). 2) Sample after spin coating with EBL resist and baking. 3) Sample after EBL exposure of several nanostructures and developing. 4) RIE of Si_3N_4. 5) RIE to lift-off the remaining resist.

5.3.1 Design drawing

The device is first drawn in MATLAB. We define the characteristics of the grating couplers, rectangles to create the waveguide, and the PhC design is included on the waveguide (see Fig. 5.18). The code to draw the structures is included in Appendix C.

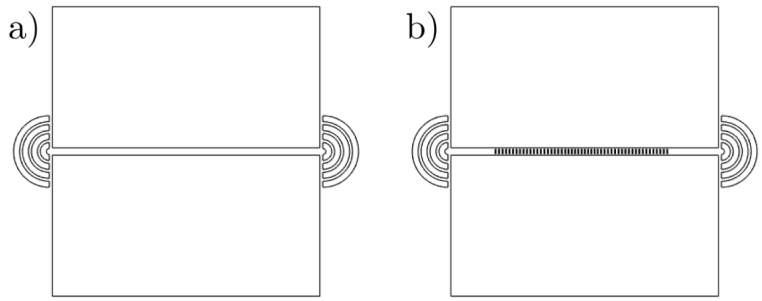

Figure 5.18: MATLAB drawing of structures of a) just the waveguide with couplers and b) the full design for the fundamental mode dielectric mode nanocavity design. The waveguide is 38 μm long.

5.3.2 Spin coating and baking

The first step of a lithographic process is to place a chemical film that is sensitive to the radiation it will be exposed to. This chemical, usually referred to as resist, must be spin coated onto the sample to obtain a homogeneous and controlled thickness. The tool that holds the sample or wafer for spin coating is called a chuck. It usually has a vacuum hold with a hole at the center to

seal and fix the sample. Since our samples have a suspended region at the center, standard vacuum chucks would alter the membrane's curvature: they would bend the central part of the membrane through their central vacuum hole. Therefore, we use a flat chuck where we place double sided tape to fix the sample (see Fig. 5.19). Although we designed a chuck specially for these samples, the best spin coating results have been obtained with the double sided tape technique.

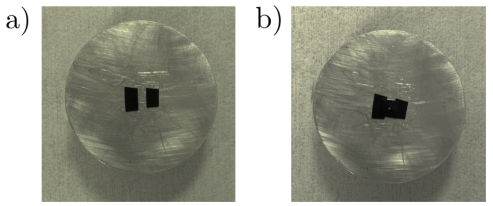

Figure 5.19: Pictures of spin coating chuck. a) Shown with double sided tape. b) Shown with the sample fixed at the center.

We place the sample in the spin coater and deposit a drop of electron beam resist CSAR 62 (AR-P 6200.13) on the membrane and spin coat at 8000 rpm for 1 minute, which provides a thickness of about 300 nm. Afterwards, the sample is baked for 1 minute at 175^{o} Celsius. This stabilizes the resist; it dries it and removes excess solvent, and thus allows higher repeatability of the fabrication process.

5.3.3 Electron beam lithography

Once the sample is ready for lithography, we expose it by scanning a focused beam of electrons with an Inspect F50 electron beam lithography (EBL) microscope RAITH Elphy Plus. The samples are fixed in the holder of the F50 microscope with two metallic pieces (see Fig. 5.20) to ensure that the membranes don't break. The exposure is performed with a spot size of 2 (dimensionless parameter that depends on the system), voltage of 30 kV, emission current 166 μA, beam current of 0.04092 nA, an area dose of 80 μAs/cm^2, and a dose factor between 1.3-1.9. The exposure of 1 sample with around 40 nanocavities takes approximately an hour.

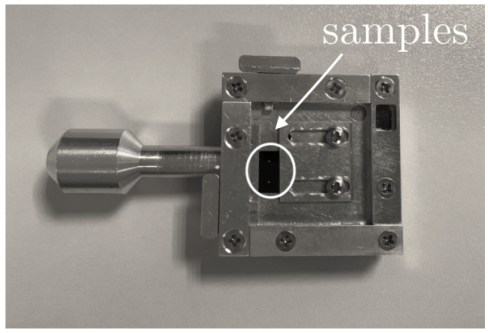

Figure 5.20: Picture of the EBL holder with two samples. They are fixed to the holder with two metallic pieces. The clamps of the holder itself are too big and would damage the sample.

The resist is chemically changed by the electron beam. We remove the exposed regions by developing the sample, introducing the sample in the developer AR600-546 for 1 minute and then in a stopper, IPA (isopropilic alcohol), for 1 minute. This process removes the exposed regions and provides a mask for the next step: etching away the Si_3N_4.

5.3.4 Reactive ion etching

For both etching the Si_3N_4 and removing the leftover resist, we use an Oxford Instruments Plasmalab System 100. A good clean room practice is to first pre-condition the chamber before running any process. Therefore, we run the recipe to etch Si_3N_4 for 10 minutes (see table 5.1).

Set pressure	45 mTorr	**Gasses**	
RF Fwd power	60 W	O_2	5 sccm
RF DC bias	235V	CHF_3	50 sccm
Temperature	20 °C		

Table 5.1: Si_3N_4 etching recipe.

Meanwhile the chamber is undergoing the pre-conditioning process, we prepare the samples by adhering them to a Si wafer with Fomblin–vacuum lubricant. This creates a good thermal contact between the sample and the Si wafer, avoiding crusting and overheating of the resist that is difficult to remove afterwards. Once the preconditioning is over, we introduce the sample in the reactive ion etching (RIE) machine and we etch away the Si_3N_4 in 10 minutes with the recipe shown in table 5.1. Finally, we proceed to remove the remaining resist from the samples. Once again, we pre-condition

the chamber for 5 minutes with an oxygen cleaning process; it is also the one we use to etch away the resist, but for only 1 minute (see table 5.2).

Set pressure	10 mTorr	**Gasses**	
RF Fwd power	100 W	O_2	30 sccm
RF DC bias	426V		
ICP Fwd power	150 W		
Temperature	20 °C		

Table 5.2: Resist lift-off recipe for RIE.

The very last clean room step is a final oxygen plasma in a plasma generator (Tepla) to remove any remaining residue from the RIE (e.g. Fomblin on the bottom of the sample). The recipe parameters consist in an oxygen gas flux of 400 ml/min and 200 W of power during 5 minutes.

Once the fabrication procedure is complete, we take SEM images of the nanocavities to characterize its dimensions and correct parameters accordingly in future exposures. We also check the cleanliness of the structures. In Fig. 5.21, we can see an example of one of the resulting nanobeams.

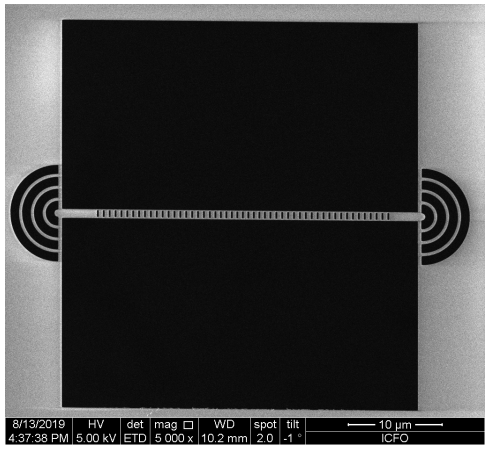

Figure 5.21: SEM image of a dielectric mode PhC nanocavity.

5.4 Optical setup

Our optomechanical and thermal experiments take place inside a vacuum chamber (Kimball Physics). Vacuum conditions are attained with a turbo pump HiCube 80 ECO from Pfeiffer Vacuum. Inside the vacuum chamber there is a 3-axis closed-loop piezo stage from SmartAct with vibration control

where the nanocavity sample is placed and aligned. A 0.85 NA 100× IR objective (Olympus LCPLN100XIR) is used to both trap the nanoparticle and couple in and out light from the nanocavity.

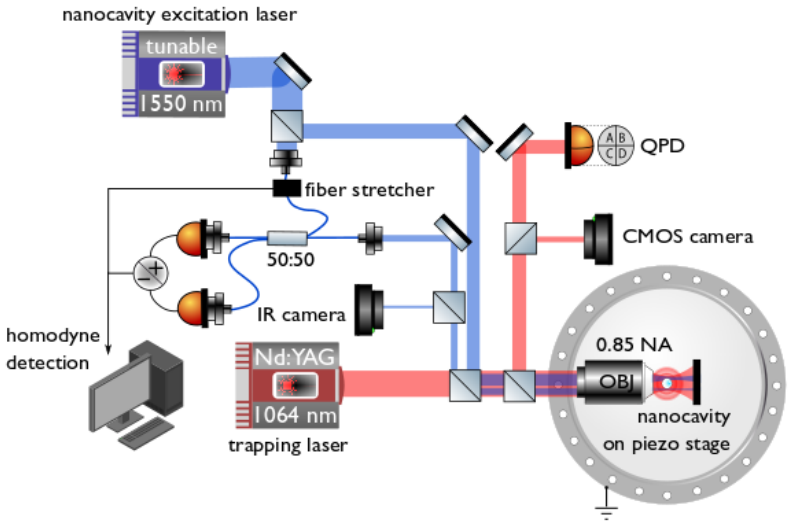

Figure 5.22: Simplified diagram of the optical setup for both the nanocavity excitation and detection, and the nanoparticle trapping and manipulation.

The optical setup of the experiment has two different sections: a nanoparticle trapping and manipulation part, and the nanocavity excitation and read out. In the following we will explain both parts of the setup, which are depicted in Fig. 5.22.

5.4.1 Optical trapping and nanoparticle manipulation

To trap nanoparticles we use a 1064 nm (Manlight) laser. As shown in Fig. 5.23, this laser is fiber coupled out with a collimator and is then re-sized with a telescope made of lenses with $f = -50$ mm and $f = 75$ mm. The last lens is placed on a movable stage to allow changes in the collimation. This enables us to adjust the position of the focus of the trap along the propagation direction z. Afterwards, we ensure maximum transmission of linearly polarized light into the optical trap through a $\lambda/4$ and a $\lambda/2$ waveplates, and a polarization beam splitter (PBS). We use another $\lambda/2$ to rotate the polarization direction of the linearly polarized light; which will provide non-degenerate nanoparticle's mechanical frequencies along the x and y directions and will allow us to identify them.

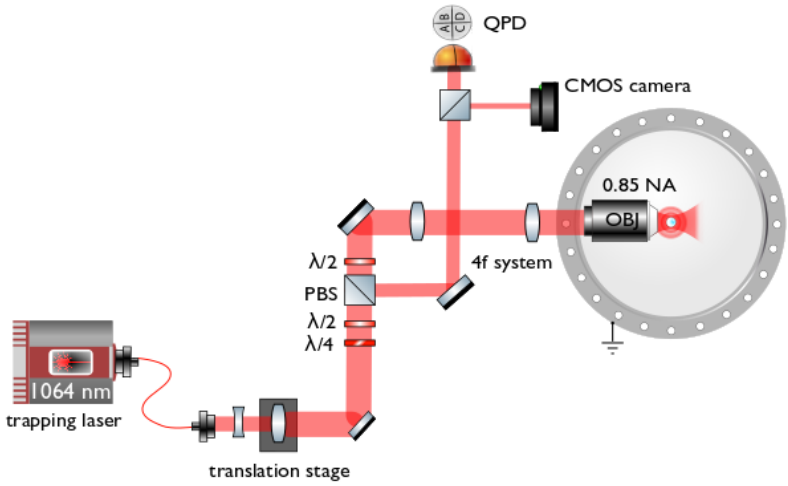

Figure 5.23: Diagram of the optical trapping and nanoparticle manipulation part of the setup. After the 1064 nm light is coupled into free space, two lenses control the collimation of the beam. The last one is placed on a moveable stage to adjust the beam focus (and therefore the nanoparticle's position along z) by varying the collimation. We ensure a controlled polarization with the combination of a PBS and waveplates. The $4f$ system allows us to steer the beam without misalignment at the back aperture of the objective. We monitor the trapped nanoparticle both through imaging with a CMOS camera and with a QPD detector.

Right before the trapping objective we place a $4f$ system that starts at the mirror and ends at the back aperture of the objective (see Fig. 5.24). This permits us to steer the beam inside the chamber along the x and y directions, and to approach the nanoparticle to the nanocavity without losing light that goes through the back aperture of the objective.

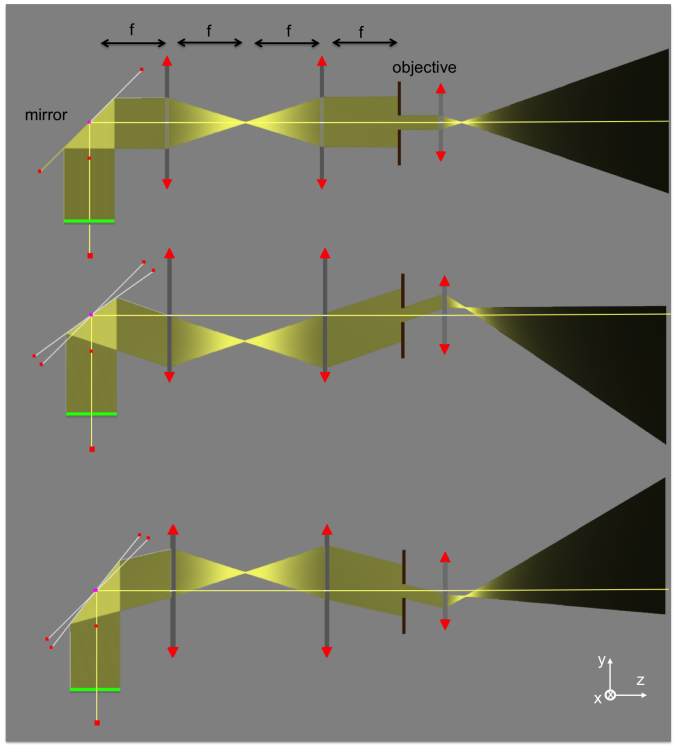

Figure 5.24: Diagram of how a $4f$ system allows us to image the mirror (aperture + lens in this schematics) onto the back aperture of the objective. This results in manipulation of the nanoparticle along both the x and y directions (z is the direction of propagation beam of the light exiting the objective). The yellow line, common to all three cases, indicates the optical axis. The other second and third cases show how the particle can be moved both up and down along the y direction. This also applies for the x direction but is not shown here. Figure created with ricktu288.github.io Ray Optic's simulator.

The motion of the particle is detected in the far-field via backscattering with a QPD (New focus model 2911) and we also monitor the position of the particle with a CMOS camera (Thorlabs DC16545M).

5.4.2 Nanocavity excitation and read-out

The nanocavity section of the setup injects light into the nanocavity and detects the output beam from it (see Fig. 5.25); both input and output go through the 100× IR objective. We use two different types of sources, connected through an optical fiber: a super-continuum source from NKT photonics SuperK compact, and a tunable 1550 nm laser source (shown in

Fig. 5.25), a Cobrite model from Pure Photonics PPCL300 that covers the range of 1515-1575 nm and has a linewidth of 10kHz.

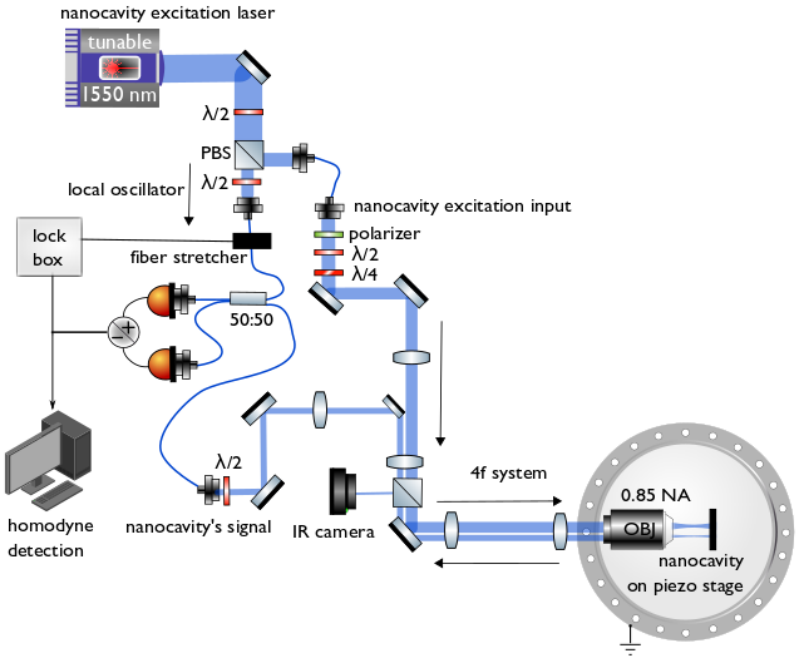

Figure 5.25: Diagram of the nanocavity excitation and read-out. The tunable 1550 nm laser beam splits into nanocavity excitation and local oscillator. The nanocavity excitation includes polarization control, and the use of a $4f$ system to image the nanocavity onto a D-shaped mirror so that only the output light is detected. The nanocavity's signal can be coupled into a fiber for detection or to a spectrometer to characterize it. We also use an IR camera to image the nanocavity. The local oscillator includes a fiber stretcher and a lock box for homodyne detection.

The nanocavity's output beam splits in two. One part is sent to a Xenics Xeva-1795/XC137 IR camera to visualize the structure and check its alignment via its illumination, and the other to a fiber for signal detection. The IR camera also detects the reflection from the nanocavity's input coupler, providing information of the shape and size of our input beam as well as of the output beam (shown in Fig. 7.8).

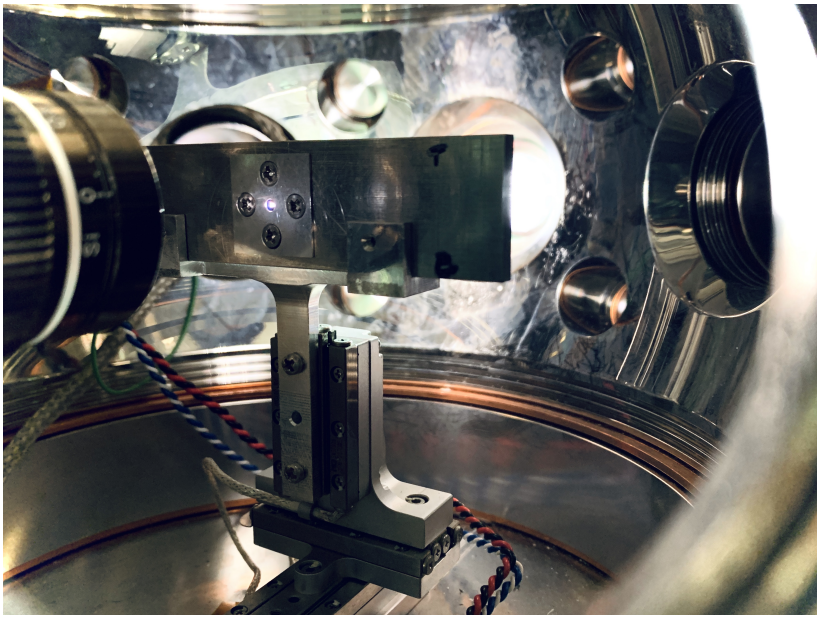

Figure 5.26: Photograph of the inside of the chamber. On the left, we see the trapping objective, and in the middle the sample holder mounted on a 3-axis piezo stage.

Nanocavity characterization

Right after the samples are made in the clean room, we optically characterize them to make sure the cavities' resonances are within the wavelength range of our IR laser. To excite the cavity we use a NKT super-continuum source, and the nanocavity's output signal is sent from the detection fiber into a spectrometer Andor Technology SR-303I-A (with an InGaAs DU491A-1.7). In Fig. 5.27, we show a typical transmission spectra of both air mode and dielectric mode nanocavities.

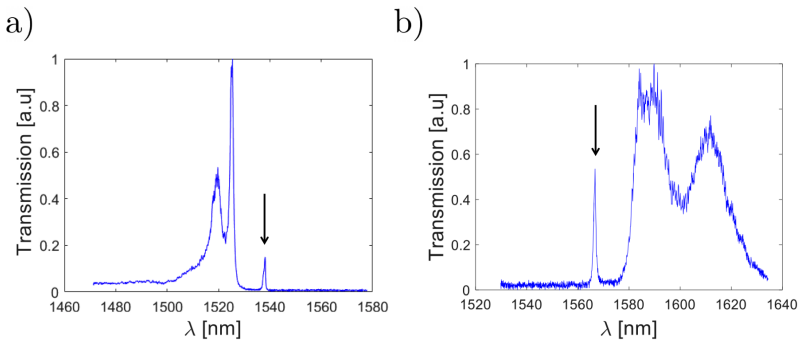

Figure 5.27: Spectra from the nanocavity: a) shows the air mode design: band edge on the left followed by the cavity's resonance peak marked. b) shows the dielectric mode design: resonance peak followed by the band edge, which is similar to the one shown in Fig. 5.10. The cavity's resonance peak is marked with an arrow for each case.

In Fig. 5.27 a), we present the spectra of an air mode nanocavity. The peaks in the range of 1500–1530 nm are the band edge. There is another band edge at higher wavelengths but we don't always observe it because our excitation source has low emission at long wavelengths and the grating coupler's transmission is always multiplied with the band gap transmission spectra. The nanocavity's resonant wavelength that propagates inside the band gap is the peak close to 1540 nm, due to the defect. In a similar way, we observe the band edge peaks of the dielectric mode nanocavity between 1580–1640 nm in Fig. 5.27 b). In this case, we find the other band edge at lower wavelengths, but for the same reasons, we don't usually observe it. The nanocavity's peak is around 1565 nm. For both cases, the sections with low transmission represent the band gap.

Balanced homodyne detection

Homodyne detection is an interferometric detection scheme based on the interference of two beams of the same wavelength λ: the signal beam and the reference beam, often referred to as the local oscillator (see Fig. 5.28). We will use this detection method in section 7.4.1 to measure the nanoparticle's dynamics through the nanocavity. It is a detection scheme sensitive to optical phase shifts—given by the optical path difference—of one beam with respect to the other. The interference between the two beams transforms any phase modulation into an intensity modulation.

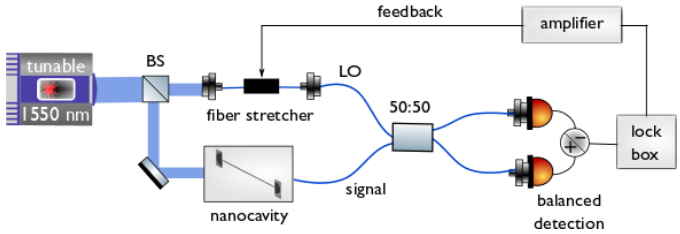

Figure 5.28: Schematic balanced homodyne detection diagram. The laser beam is divided into the light that goes into the cavity and to the local oscillator. The output of the nanocavity and the local oscillator interfere, providing a signal that contains information about the phase modulation between the two beams. This interference signal is divided in two and is detected with a balanced photodiode. The balanced photodiode signal is introduced into the lock box to keep the phase difference constant between the two beams. The error signal from the lock box provide the feedback that drives the fiber stretcher in the local oscillator's path.

In our experiment the signal beam is the cavity output light, and the local oscillator is given by another beam of light from the same laser source (see Fig. 5.28). These two beams, signal and local oscillator, interfere at the 50:50 fiber beam splitter (IDIL fibres optiques):

$$E_{\mathrm{LO}}(t) = E_{\mathrm{LO,o}} \cos\left(k x_{\mathrm{LO}}(t) - \omega t\right), \tag{5.5}$$

$$E_{\mathrm{signal}}(t) = E_{\mathrm{signal,o}} \cos\left(k x_{\mathrm{signal}}(t) - \omega t\right). \tag{5.6}$$

Just like a free-space beam splitter, the fiber beam splitter adds a π phase shift only to one of the outcoming beams. The transmitted electric fields have no phase shift and, according to the Fresnel equation, reflection carries a phase shift when light propagated through a low refractive index is reflected at a material of high refractive index. The two outcoming optical signals are:

$$I_1(t) = \frac{1}{2}\left[E^2_{\mathrm{LO,o}} + E^2_{\mathrm{signal,o}} + 2E_{\mathrm{LO,o}}E_{\mathrm{signal,o}} \cos\left(\Delta\phi(t)\right)\right], \tag{5.7}$$

$$I_2(t) = \frac{1}{2}\left[E^2_{\mathrm{LO,o}} + E^2_{\mathrm{signal,o}} - 2E_{\mathrm{LO,o}}E_{\mathrm{signal,o}} \cos\left(\Delta\phi(t)\right)\right], \tag{5.8}$$

where $\Delta\phi(t) = \phi_{\mathrm{LO}}(t) - \phi_{\mathrm{signal}}(t)$, $\phi_{\mathrm{LO}}(t) = \frac{2\pi}{\lambda} x_{\mathrm{LO}}(t)$, $\phi_{\mathrm{signal}}(t) = \frac{2\pi}{\lambda} x_{\mathrm{signal}}(t)$. The intensities $I_1(t)$ and $I_2(t)$ are the two inputs of a balance photodetector (New focus 1817). So, ultimately, the signal we detect is the subtraction of these two:

$$I_{\mathrm{detector}}(t) = 2E_{\mathrm{LO,o}}E_{\mathrm{signal,o}} \cos\left(\phi_{\mathrm{LO}}(t) - \phi_{\mathrm{signal}}(t)\right). \tag{5.9}$$

To eliminate unwanted noise, ideally, the difference in phase $\Delta\phi = \phi_{\mathrm{LO}} - \phi_{\mathrm{signal}}$ between both beams must be locked for frequencies that are outside

our window of interest[3]. The phase lock is done at the point where the intensity profile from the interference of both beams varies the most: at the greater slope of the cosine term in equation (5.9). So, for a cosine, the maximum of the intensity profile is found at $\Delta\phi = 0$ and the minimum at $\Delta\phi = \pi$; the steepest slope, and therefore where sensitivity is maximum, corresponds to the quadrature point of $\Delta\phi = \pi/2$.

We use the Cobrite laser to perform homodyne detection. The information carrier is the light that exits the output grating coupler (typically 500–1000 nW); the local oscillator arm (around 0.2 mW) includes a polarization maintaining fiber stretcher (IDIL fibres optiques) which can be driven by a voltage signal between 0–150 V to vary its length up to 20μm. We correct for slow drifts (e.g. mechanical noise, slight changes in temperature, laser intensity or polarization) under 1 kHz by means of a lock box[4] (LB1005 Servo controler from New Focus), and an amplifier (Falco Systems WMA-300): they drive the fiber stretcher to compensate for drifts and keep the difference in phase between the cavity signal and the local oscillator locked at $\Delta\phi = \pi/2$, thanks to its integrator module.

Homodyne detection has the advantage of being insensitive to fluctuations in laser intensity. Moreover, the light from E^2_{signal} is generally weaker than the local oscillator, so the interfered signal can be amplified just by increasing I_{LO}. However, polarization must be the same for both the signal and local oscillator beams for a good interference; for this reason, we use polarization maintaining fibers and we adjust the polarization for both beams with a $\lambda/2$ waveplate before coupling light into the fibers that reach the 50:50 fiber beam splitter for interference.

Considering the phase profile of an optical cavity (see Fig. 5.29), we can see that homodyne detection works best when we are probing the cavity on resonance. Under these circumstances, we are more sensitive to phase changes than if we are detuned from the nanocavity's resonance. The opposite is true for direct detection—where we directly probe cavity intensity changes—as shown on Fig. 5.29, where the optimum detuning regions are marked in orange.

[3]Our window of interest is the range of frequency of the nanoparticle's oscillations. This typically ranges between 30 kHz and 180 kHz.

[4]The lock box primary function is to provide a feedback system: it forces the system's parameters to a selected value regardless of external disturbances. The difference between this desired value and the actual value is called the error signal.

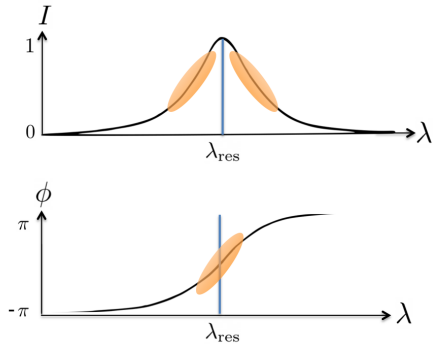

Figure 5.29: Direct detection vs. homodyne detection. Top: for best sensitivity in intensity, we must be slightly off resonance (orange sections). Bottom: In the case of homodyne detection—sensitive to phase—the excitation wavelength must be on resonance for best sensitivity [105, 166].

Chapter 6

Nanocavity's thermal dynamics

6.1 Introduction

As we have seen in section 3.2, to increase the single-photon optomechanical coupling factor g_0, we require a high Q/V_c. This is the main motivation to use nanocavities. Micro- and nanocavities, when excited on resonance, confine high powers into small volumes, becoming susceptible to thermally induced nonlinearities. The absorbed power is forced to dissipate through a small surface area, giving rise to a thermal drift of the resonance [66], also called thermal dispersion. This is specially true when the nanocavity is in vacuum and is thermally isolated from the environment, like our PhC nanobeam. More in general, recent studies have demonstrated that the most common mechanisms that affect micro- and nanocavities' resonance frequencies are: the nonlinear thermo-optic effect[1], the optical Kerr effect[2], two photon absorption[3], thermal expansion[4], and the thermo-mechanical effect[5] [67]. They all affect the resonance of the cavity λ_{res} by, usually, modifying the geometry of the cavity or the refractive index of the material it is made off.

In this chapter, we begin by characterizing the dependence of λ_{res} with temperature for different heating sources. We also compare a dielectric mode

[1]The nonlinear thermo-optic effect—typically dominant in micro- and nanocavities—relates a change in refractive index to a change in temperature.

[2]The optical Kerr effect is a nonlinear effect where the index of refraction varies with the intensity of light propagating through a material, it is due to a nonlinear polarization generated in the medium.

[3]Two photon absorption is a nonlinear optical process where the absorption of two photons generates free carriers in a material.

[4]Thermal expansion is the tendency of matter to change its shape, area, and volume in response to a change in temperature.

[5]The thermo-mechanical effect can actually deform the mechanical structure due to a temperature variation.

nanocavity (see section 6.3.1) to an air mode nanocavity (see section 6.3.2): the first concentrates most of the electric field on the volumes of the defect where there is silicon nitride, and the second in air. Finally, we show and characterize bistability, as well as self-induced oscillations in the nanocavity's output transmission. The data presented here has allowed us to obtain further understanding of the nanocavity's thermal dynamics, to later perform and analyze the experiments shown in chapter 7.

6.2 Resonance dependence with temperature

When the nanocavity's temperature increases, the resonant wavelength λ_{res} varies. For silicon nitride, this can be provoked by a thermo-optic effect, a thermal expansion, and/or a thermo-mechanical effect. In our experiment in chapter 7, the power absorbed by the nanocavity is due to the resonant intra-cavity light propagating along the nanobeam, and the radiation from the trapping laser close to the nanocavity. In Fig. 6.1 we show two COMSOL thermal simulations for how both light sources increase the temperature of the nanocavity in vacuum conditions.

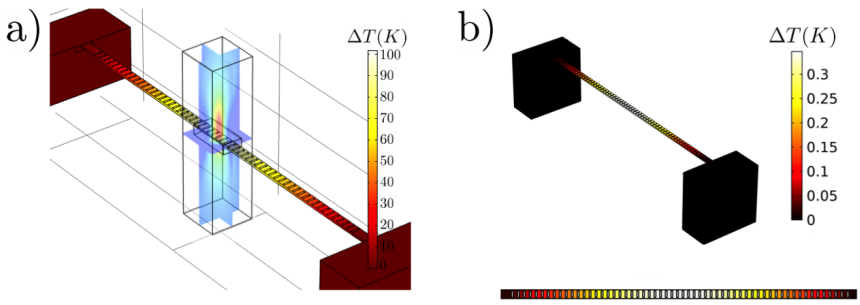

Figure 6.1: COMSOL simulation of the nanocavity's temperature with a) 100 mW of the 1064 nm trapping laser focused at the center of the nanobeam as a heat source and b) cavity on resonance at 1μW of light coupled to the nanobeam [165].

The COMSOL simulations consider conduction as the only heat dissipation mechanism: convection does not happen in vacuum, and black body radiation is considered negligible [167]. We account for the material's absorption by including the imaginary part of the index of refraction of the Si_3N_4 membranes, $k_{\lambda_{\text{trap}}} = 0.001$ [6] at $\lambda_{\text{trap}} = 1064$ nm. From the simulation, we observe a temperature increase of 100 K when a 100 mW laser beam, having a Gaussian width of 2 μm at λ_{trap}, is focused on the center of

[6] Value provided by Norcada.

the nanobeam. When considering the light propagating inside the cavity, we take the imaginary part of the index of refraction of Si_3N_4, $k_{\lambda_{res}} = 0.0005$ [7] at $\lambda_{res} = 1550$ nm. For the resonant wavelength λ_{res}, we obtain a temperature increase of about 0.3 K when the input power is 1 μW (see Fig. 6.1 b)). These simulations estimate how much each light source contributes to an increase in temperature of the cavity.

Experimentally, we observed a shift in the cavity's resonant wavelength λ_{res} related to the increase in temperature. To look directly at these spectral changes, we excited the nanocavity with a super-continuum source (SC) and analyzed the out-coupled light with a spectrometer (see section 5.4.2). In this way, we tested the heating effect for both the trapping beam and the intra-cavity light. For both of these light sources, we initially observed the resonant wavelength λ_{res} blue-shift as shown in Fig. 6.2. We believe this is due to a thermo-mechanical effect [83], which describes how the mechanical deformation of the nanocavity, due to a temperature increase, leads to a change in resonance.

In Fig. 6.2 a), we show the dielectric mode nanocavity's experimental resonance shift to lower wavelengths (blue-shift) for the trapping laser as we increased its optical power. To limit the effect of heating, which can lead to damages of the nanocavities[8], we carried out this test in ambient conditions. At lower pressures we obtain the same qualitative behavior, but for lower optical input powers. Hence, we expect a lower temperature increase than the one in the simulation in Fig. 6.1 a) because of air, which dissipates energy through convection, plus lower optical powers of the trapping beam.

In contrast, the spectra for the intra-cavity light were taken at 0.5 mbar, which is the pressure used in chapter 7 for the levitodynamics experiment. We increased the temperature of the nanocavity by keeping it on resonance, adjusting the excitation laser's wavelength repeatedly. Hence, λ_{res} shifts to smaller wavelengths until it reaches a point λ_{final}. At λ_{final}, excitability effects such as self-induced oscillation appear in the nanocavity's transmission . The blue-shift is presented in Fig. 6.2 b), where the resonant wavelength λ_{res} can vary up to 20 nm from the starting value λ_0.

In the following experiments, we used a second mode (dielectric mode design) nanocavity, design with 19 defect cells (see section 5.2.3), unless otherwise specified.

[7] Value provided by Norcada.

[8] More details on the thermal damage threshold of the nanocavities are shown in Appendix A.

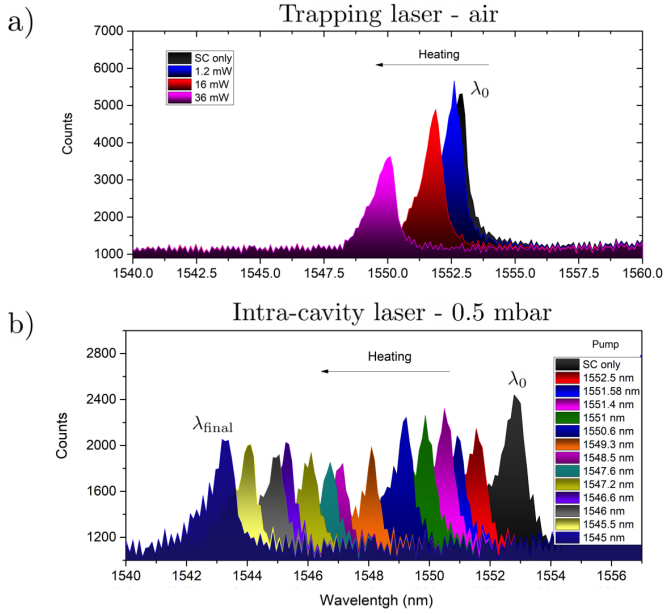

Figure 6.2: Nanocavity under super-continuum illumination and read-out with a spectrometer. a) Shift in resonance due to increasing power of 1064 nm trapping laser focused at the center of the nanobeam in ambient conditions. The resonance can be continuously shifted by increasing the power until the nanocavities are damaged. b) Shift in resonance due to the intra-cavity excitation from the 1550 nm tunable laser source at 0.5 mbar. We excited the nanocavity on resonance, and observed λ_{res} blue-shift. We repeatedly varied the 1550 tunable laser's wavelength to always excite the nanocavity on resonance until the nanocavity reached λ_{final}.

6.2.1 Resonance characterization with other heating sources

To further understand and characterize the blue-shift in λ_{res}, we measured the variation in the nanocavity's resonance with two different heating sources. First, we illuminated the full nanobeam with a 532 nm laser. We focused it to a $\sim$ 100 μm Gaussian width size with a f = 150 mm lens. This differs from the two previous experiments since the green laser heated the whole structure, and not just the central part of the nanobeam. Second, we used a temperature-controlled heater where the heater was in direct contact with the sample holder (see Fig. 6.3). We controlled and measured the temperature externally with a Thorlabs TC200 Thermal Controller and a thermocouple positioned $\sim$ 5 mm away from the cavities.

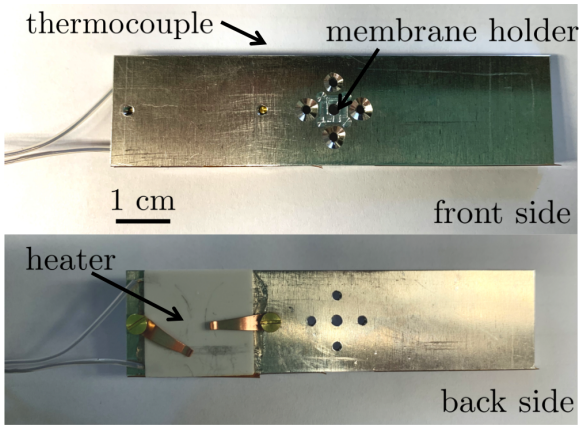

Figure 6.3: Front and back pictures of the aluminum sample holder with a heater. A thermocouple is inserted on the top side part of the sample holder. It measures the temperature of the sample holder close to where the Si_3N_4 membrane is placed. In the back, we show the heater which is controlled externally with a Thorlabs TC200 Thermal Controller.

We observed a blue-shift of the cavity's resonance for both the green laser and the heater as the nanocavity heats up. For the 532 nm laser, we observed a linear decrease of the cavity's resonance wavelength as the power of the laser increased. We extracted a value of -0.12 ± 0.2 nm/mW from Fig. 6.4 a). In the case of the heater, we monitored λ_{res} in time at $5 \cdot 10^{-5}$ mbar; besides the blue-shift induced by a temperature increase, we noticed that the cavity takes time to heat up and reach thermal equilibrium ($\sim$ 20 minutes as shown in Fig. 6.4 b)). Although the sample holder heats up quickly, the nanocavities take longer to thermalize with it because they are suspended on a membrane. As previously mentioned, there are very few air molecules for heat to dissipate through convection at low pressures, and radiation is negligible. At higher pressures we did not observe a significant temperature increase due to the aforementioned heating dissipation mechanisms.

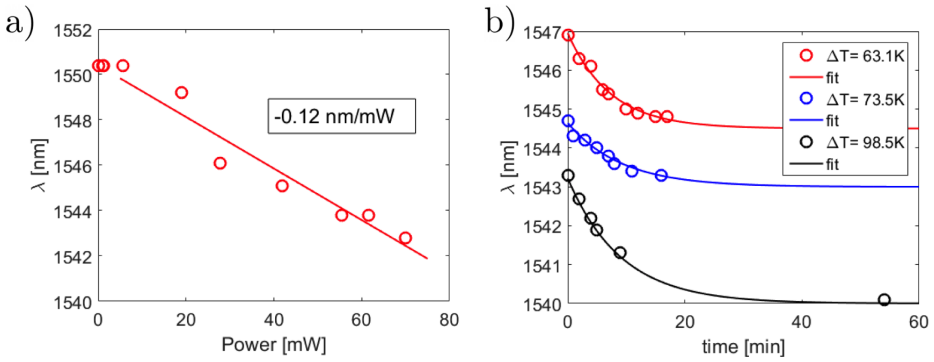

Figure 6.4: Variation of the nanocavity's resonance λ_{res} by a) heating it up with a green laser illuminating the full membrane at 0.5 mbar, with a slope of -0.12 ± 0.2 nm/mW, and in time with b) a heater at $5 \cdot 10^{-5}$ mbar. This last measurement was done at low pressures to reduce convection. We plot three curves: for each one we set the temperature to a given value and waited for the sample to heat up and reach a thermal equilibrium state (this process is quite slow). After 20 minutes, we increased the temperature and restarted the time count for the temperature change. By fitting an exponential decay to all three curves, we obtain a decay rate of ~ 9 minutes. In both measurements, the measurements' error for the wavelength is 0.1nm, for the power 1%, and for the time 0.1 minutes.

The controlled-temperature heater allowed us to quantify the variation of λ_{res} and its blue-shift. The results are shown in Fig. 6.5, where we waited for the nanocavity to find a thermal equilibrium after each temperature increase ΔT, as we show in Fig. 6.4 b). Through a linear fit, we found a $\frac{d\lambda}{dT}$ of -0.15 ± 0.05 nm/K, which we hypothesize is due to a thermo-mechanical (TM) effect (see Fig. 6.5). With this value, we can estimate that a blue-shift of 20 nm corresponds to a $\Delta T \sim 130$ K. The value of $\frac{d\lambda}{dT} = -0.15 \pm 0.05$ nm/K is very close to state of the art experiments that strive for a high thermal sensitivity: 0.162 nm/K for cascaded PhC nanobeam cavities in silicon [168], 0.245 nm/K for a PDMS covered microsphere sensor [169], and 1.17 nm/K for a silk fibroin microtoroid [170].

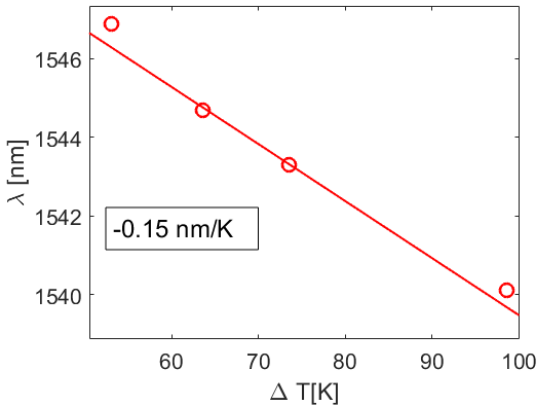

Figure 6.5: Measurements of the variation of the nanocavity's resonance λ_{res} by increasing its temperature with a heater at $5 \cdot 10^{-5}$ mbar. We obtain a blue-shift of -0.15 ± 0.05 nm/K. Our measurement in wavelength has an error of 0.1 nm given by the spectrometor and in temperature of 0.1 K given by the Thorlabs thermal controller.

Besides the predominant thermo-mechanical (TM) blue-shift, we know that the thermo-optic (TO) effect given by dn/dT provides a red-shift, and is $\sim 2.5 \cdot 10^{-5}$ K^{-1} for silicon nitride [134], [135]. From this we can calculate the corresponding wavelength shift: $\frac{dn}{dT}\frac{\lambda_{\text{res}}}{n_0} \approx 0.02$ nm/K for $n_0 = 2.13$ (value provided by Norcada) and $\lambda_{\text{res}} = 1550$ nm. The thermal expansion, which also produces a red-shift, is considered negligible [136] since it is an order of magnitude smaller than the thermo-optic effect. Thus, the complete expression of $\frac{d\lambda_{\text{res}}}{dT}$ for our system, similar to what is shown in section 3.3, is:

$$\begin{aligned} \frac{d\lambda_{\text{res}}}{dT} &= \left(\frac{d\lambda_{\text{res}}}{dT}\right)_{\text{TM}} + \left(\frac{d\lambda_{\text{res}}}{dT}\right)_{\text{TO}} \\ &= \left(\frac{d\lambda_{\text{res}}}{dT}\right)_{\text{TM}} + \frac{dn}{dT}\frac{\lambda_0}{n_0}, \end{aligned} \tag{6.1}$$

where the TM term produces a blue-shift of the nanocavity's resonance whereas the TO term induces a red-shift.

In summary, we've experimentally found a predominant blue-shift, attributed to the deformation of the nanobeam with increasing temperatures. To further understand the heating behavior, we also carried out tests to heat the nanocavity with both the heater and the green laser. With these assessments, we wanted to evaluate if we could actively control the nanocavity's resonance with an external heating source. Unfortunately, the increase in temperature due to exciting the cavity on resonance and its associated

blue-shift, proved to be considerably stronger than any other heating source, eliminating this possibility. However, we managed to obtain a stable resonance via the excitation block, as will be shown in chapter 7. In other systems, the cavity's resonance is usually controlled with an external laser or a heater [171, 172, 173].

6.3 Nanocavity design comparison

A different direction to reduce and minimize the nanocavity's heating dynamics was to vary its design: from a dielectric mode to an air mode nanocavity. With the latter, we expected less blue-shift for the same input power since the electric field concentrates in the air holes instead of in the material.

We've just mentioned that the cavity's resonant wavelength λ_{res} can blue-shift up to 20 nm when heated, until a value of λ_{final} is reached for heating due to the intra-cavity light (see Fig. 6.2 b)). We typically observe this large shift for samples which are stored in air after fabrication, and we believe it could be partially caused by water adsorption. The presence of water red-shifts the cavity's resonance due to an increase in the refractive index of the surrounding medium around the nanocavity [174]. Afterwards, when we heat the nanocavities, water probably evaporates. Thus, the resonance blue-shifts back and a large excursion in the cavity's resonance takes place. On the contrary, when samples are preserved directly in vacuum after fabrication, we observe significantly smaller blue-shifts when heating the nanocavities.

6.3.1 Dielectric mode nanocavity

In Fig. 6.6 we show a 3 nm blue-shift of the dielectric mode nanocavity's resonance at a pressure of 0.5 mbar. The samples were always illuminated with a super-continuum source and the cavity's resonance was monitored with a spectrometer. We continuously excited the nanocavity on resonance with a $P_{\text{in}} = 320\ \mu$W, by following the resonance λ_{res}, until it would not shift any further.

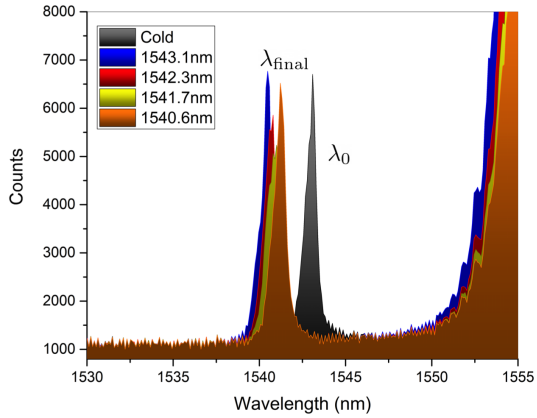

Figure 6.6: Dielectric mode nanocavity under super-continuum ilumination and read-out with a spectrometer. The blue-shift in resonance is due to the 1550 nm tunable laser source when the nanocavity is excited on resonance. The structures heat up, and blue-shift up to 3 nm. These measurements were taken at 0.5 mbar. The transmission at higher wavelengths corresponds to the edge of the band gap.

In fact, we observe how in Fig. 6.6, we reach λ_{final} with the excitation wavelength $\lambda_{\text{L}} = 1543.1$ nm. Afterwards, in an attempt to heat it further with lower excitation wavelengths we pass λ_{final}, the nanocavity is not on resonance anymore and it starts to cool back.

6.3.2 Air mode nanocavity

Just like we measured the blue-shift of the dielectric mode cavities in the previous section, we repeated the experiment for an air mode cavity that was also stored in vacuum after fabrication. We observe exactly the same behavior: a blue-shift of about 3 nm when the air mode nanocavity is excited on resonance. This design, in principle, could lead to less intense heating effects. However, we've obtained very similar thermal results with both designs, as shown in Fig. 6.7: both blue-shift ~ 3 nm.

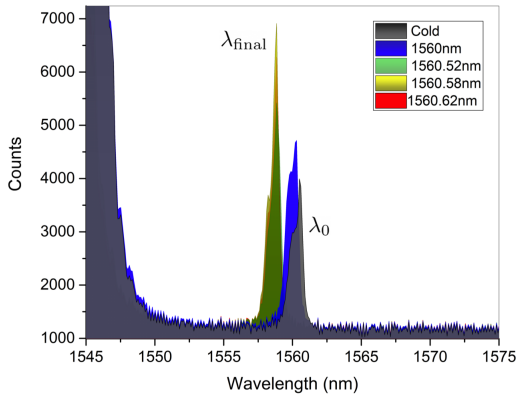

Figure 6.7: Air mode nanocavity under super-continuum ilumination and read-out with a spectrometer. The blue-shift in resonance is due to the 1550 tunable laser source when the nanocavity is excited on resonance. The structures heat up, and shift up to ~ 3 nm. These measurements were taken at 0.5 mbar. The transmission at low wavelengths corresponds to the edge of the band gap.

We believe this similarity is due to the nanocavity's thermo-mechanical effect. Regardless of the design, we always observe a predominant blue-shift, just like with the other heating sources from section 6.2.1.

6.4 Nanocavity's bistability analysis

Bistability in transmission or reflection of an optical system appears when combining a resonance in the spectral domain and a nonlinearity that alters the device's spectral response as a function of light intensity input. This translates into two co-existing stable states for transmission or reflection for the same input parameters (see section 3.3.2).

Here, we experimentally study our nanocavity's bistability by scans in wavelength and power for the intra-cavity light. These two variables dictate the amount of optical power that circulates within the cavity. The wavelength scans in Fig. 6.8 show a bistable behavior due to a red-shift given by the thermo-optic effect, which occurs at a faster timescale than the blue-shift we've measured in the previous section. These measurements were taken once we had reached λ_{final}, point where the thermo-optic effect becomes dominant and we can observe it.

In general, a direct evidence of the existence of optical bistability is the deformation of the cavity's resonance transfer function into a more and more

prominent triangular resonance profile for increasing input powers P_{in} [69, 139]. Another way to observe bistability is to vary the input power while the excitation wavelength remains the same (power scans at fixed excitation wavelength λ_{L}). In this case, we can observe the full hysteresis cycle (see Fig. 6.11). This procedure reveals two transmission states (low and high) when the input power increases or decreases along the cycle.

The experimental bistability measurements of the nanocavity were taken with a Photonetics Tunics Plus tunable external cavity laser. We programmed a code in Python to control a Red pitaya[9] to scan and save the data for all our scans. Although the scan procedure is simple, these measurements require that the timescale of the nanocavity's thermal dynamics are compatible with the duration of the scans. Also, the starting λ_{res}, should remain the same for the different scans.

6.4.1 Wavelength scans at fixed P_{in}

As we've mentioned, one sign of bistability is the appearence of the thermo-optically distorted resonance. A sharp drop starts to emerge at a given threshold power, which also depends on the pressure of the experiment. If we lower the pressure, we reduce air convection and the nanocavities reach higher temperatures for the same input power. In Fig. 6.8, we show three sets of wavelength scans for different injection powers P_{in}. One is conducted in air (top), another at a pressure of 11 mbar (middle), and the other at 0.5 mbar (bottom).

In air, the threshold power for bistability is attained at powers greater than $P_{\text{in}} \sim 500$ μW in front of the nanocavity's coupler, beyond this value we observe that the resonance looks clearly asymmetric. If we reduce the pressure further, this value drops down to 51 μW and 20 μW, for 11 mbar and 0.5 mbar, respectively. We can also notice that the linewidth of the nanocavity increases for increasing input powers for each fixed pressure [175].

[9]Red pitaya is an open-source hardware project. It is a low cost alternative to expensive laboratory instruments for measurement and control.

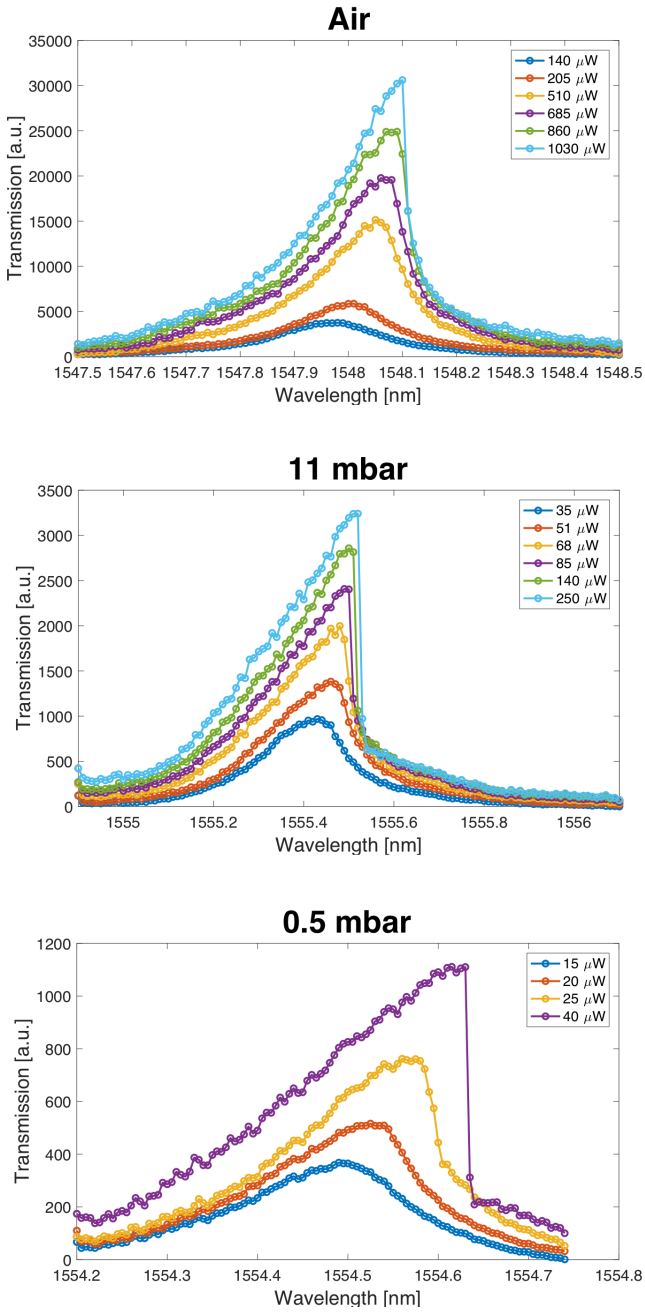

Figure 6.8: Wavelength scans for different input powers for a dielectric mode cavity. Top to bottom: scans performed in air, at 11 mbar, and 0.5 mbar. The legend indicates the power that is in front of the input coupler, $\sim 15\%$ of this power is actually injected into the waveguide. We can also observe how the linewidth of the cavity increases for increasing input power for each fixed pressure.

For a more quantitative approach to establish the bistability threshold, we calculated the skewness of the resonance profile. The skewness is a measurement of the asymmetry of a distribution. The skew can be either positive or negative. A negative skew would correspond to a longer left tail where the mass of the distribution is concentrated towards the right, just like our bistability curves in Fig. 6.8, and a positive skew would be the other way around. The skew can be defined in different ways, but they all usually include a combination of the characteristic parameters of a distribution: the mean, median, mode and standard deviation. In our case, we've used Pearson's first skewness coefficient (mode skewness) [176] to evaluate the bistability threshold for our data:

$$\text{skewness} = \frac{\text{mean} - \text{mode}}{\text{standard devitation}}. \tag{6.2}$$

With equation (6.2), we have calculated the skewness of our bistability curves in Fig. 6.8. We have set the bistablity threshold for a skewness of -0.2 [10], beyond which we establish that the transmission of the nanocavity is bistable (see Fig. 6.9). The value of -0.2 is conservative, so we are overestimating the lowest power for which bistability can be observed. The error bars are calculated by error propagation for expression (6.2).

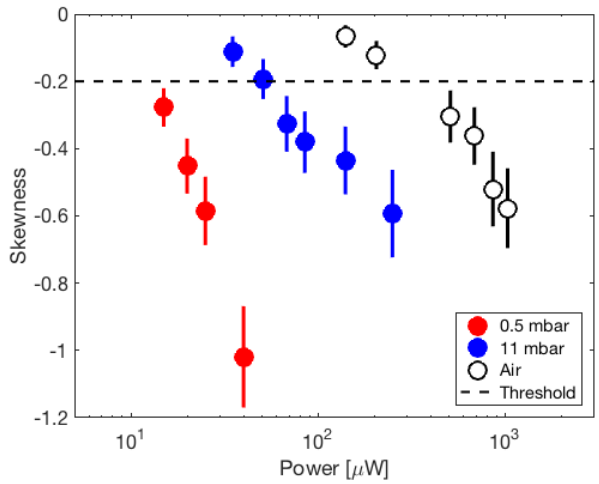

Figure 6.9: Skewness for the different bistability measurements shown in Fig. 6.8. We have set the bistability skewness threshold to -0.2. The error bars are calculated by propagating the uncertainties in each magnitude following the definition of skewness in equation (6.2).

[10] Skewness of -0.2: this means that the difference between the maximum and the mean of the distribution is 0.2× the distribution's width.

When we compare the results from Figs. 6.8 and 6.9, we see that for the scan conducted in air, we have bistability for input powers greater than $P_{\text{in}} \sim 500$ μWs. For 11 mbar, the second scan is right at the threshold power $P_{\text{in}} = 51$ μW; and for 0.5 mbar, the scan with the lowest input power, $P_{\text{in}} = 15$ μW, already shows bistability.

If we recall that our estimated coupling efficiency—similar to what is shown in literature [161]—is $\sim 15\%$, the actual injected threshold power into the waveguide lowers down to $P_{\text{thres}} \sim 75$ μW, 7.7 μW, 3 μW, for air, 11 mbar and 0.5 mbar, respectively. Other works show a minimum power threshold of 12 μW for bistability [76], and even down to 1.6 μW [68]. A low threshold power for bistability is one of the two main characteristics needed to create optical analogs of electronic components; the other attribute is that they should have a fast response time to a given stimulus.

6.4.2 P_{in} scans at fixed excitation wavelength

We can obtain the hysteresis cycle by performing power scans for a fixed excitation wavelength, as shown in Fig. 6.10 at 0.5 mbar. In these scans, we increased the input power P_{in} injected at the coupler from 35 μW to 1.3 mW and back. Each scan took 165 seconds. The speed of our scans is limited by the wavelength tunability of the excitation laser. However, the heating dynamics for the red-shift—given by the thermo-optic effect—seem to be compatible with our scan speed, since we can recover the full hysteresis loop. Similar scans completed in silicon range between 100 ns to tens of μs [76], and for silica they are ~ 10 ms [66], where thermal dynamic timescales are much faster.

In Fig. 6.10, the black stars correspond to the input power P_{in} into the nanocavity, and the blue circles to the transmitted output power from the nanocavity. The powers have been rescaled to easily compare P_{in} and P_{out} with one another: we show the linear input P_{in} and the hysteresis cycle in the nanocavity's output transmission P_{out}.

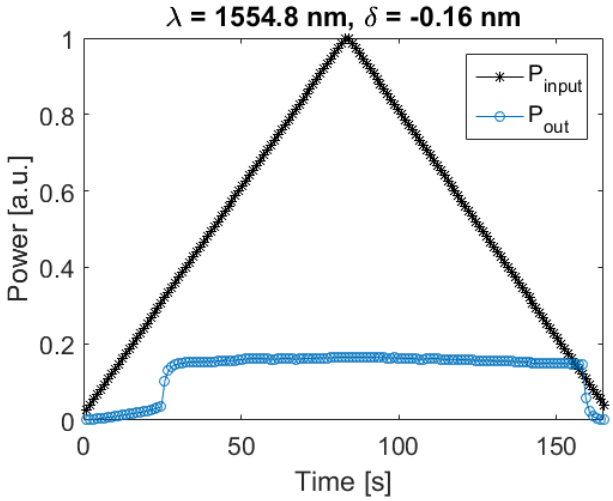

Figure 6.10: Power scan for a fixed excitation wavelength. The black stars indicate the input power at the input coupler of the nanocavity. The blue dots indicate the transmitted output power from the nanocavity.

We define the detuning from resonance as $\delta\lambda = \lambda_{\text{res}} - \lambda_{\text{L}}$, which is equivalent to the detuning defined in the frequency domain in section 3.3.2. In this definition, we obtain λ_{res} from a low P_{in} scan to avoid thermal nonlinearities, and λ_{L} is the excitation wavelength we set in our laser source. The blue-shift we've shown in section 3.3.2 can shift the starting λ_{res} and provide an inaccurate value for $\delta\lambda$. We suspect this is the case because bistability should occur for $\delta\lambda/\Delta\lambda > \sqrt{3}/2$ (see section 3.3.2), where $\Delta\lambda \sim 0.2$ nm is the linewidth for a nanocavity with $Q \sim 7000$. This means, that we should observe bistable behavior for $|\delta\lambda| \gtrsim 0.17$ nm. If we look at Fig. 6.11, we see that this is not always true, indicating that the starting λ_{res} is most likely shifting in between scans. This could be solved by performing faster and continuous scans, unavailable for our laser source.

The scan in Fig. 6.10 corresponds to the purple scan in Fig. 6.11, where we plot the cavity's output power versus the input power. Depending on the detuning from the nanocavity's resonance, we observe a different bistability area in the nanocavity's transmission (see Fig. 6.11). For wavelengths that are furthest detuned from resonance both red- and blue-detuned ($\delta\lambda = -0.51$ nm and $\delta\lambda = 0.24$ nm, respectively), the transmission is close to linear with respect to the input power and no bistability behavior is observed.

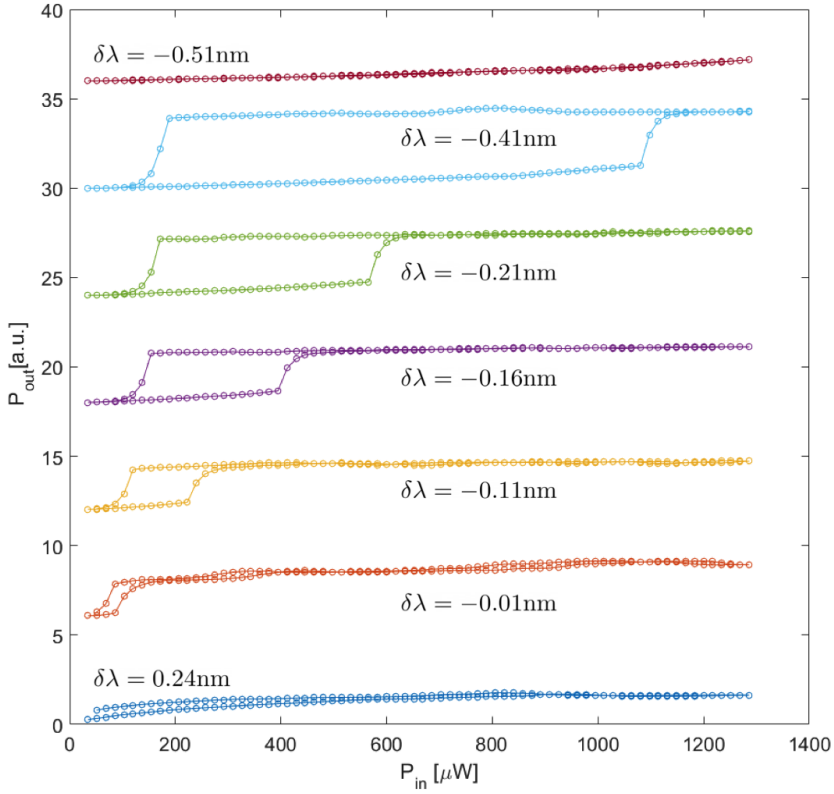

Figure 6.11: Power scans for different excitation wavelengths λ_{in} performed at 0.5 mbar for a dielectric mode cavity. Each scan is separated by a fixed value for displaying purposes. We define $\delta\lambda = \lambda_{\text{res}} - \lambda_{\text{L}}$.

The hysteresis cycles for red-detunings closer to resonance (see Fig. 6.11) show the underlying bistability curve from Fig. 3.7 a), where P_{up} is the injection power that brings the nanocavity into the high transmission state, and P_{down} is the power when it lowers back to the minimum transmission state. These values depend on the power and the wavelength of the excitation source λ_{L}, since both of these parameters determine the amount of optical power that circulates within the nanocavity. In Fig. 6.11, for the cases where the hysteresis cycle is clearly visible, we observe how the greater the detuning, the larger P_{up} is. On the contrary, P_{down} remains constant for most $\delta\lambda$ where bistability is observed (see Fig. 6.12).

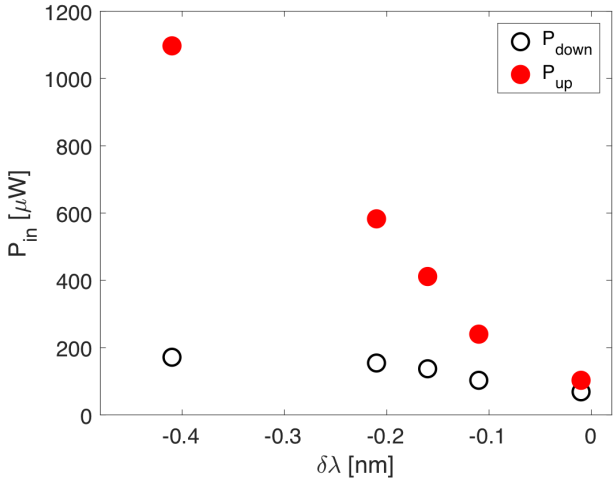

Figure 6.12: P_{up} and P_{down} for all red-detuned $\delta\lambda$ that show a hysteresis cycle from Fig. 6.11. The error for P_{in} is less that 1% and the resolution in $\delta\lambda = 0.001$ nm.

In Fig. 6.12, we extracted P_{up} and P_{down} for the hysteresis cycles from Fig. 6.11. Considering the $\sim$ 15% efficiency of the couplers, for $\delta\lambda = -0.1$ nm, $P_{\text{up}} \sim 11$ μW and the value for P_{down} is almost the same. In contrast, for $\delta\lambda = -0.41$ nm, the $\delta\lambda$ with the greatest hysteresis, $P_{\text{up}} \sim 170$ μW, and $P_{\text{down}} \sim 30$ μW. Also, in Fig. 6.12, we observe how as the detuning increases, so does the bistability zone: P_{down} stays mostly constant and P_{up} is proportional to the detuning. The minimum threshold power $P_{\text{up}} = 11$ μW is similar to previous reported power thresholds [69, 77].

The same type of behavior can be found for an air mode nanocavity. These results are shown in Appendix B.

6.5 Self-induced oscillations

Self-induced oscillations are the result of two competing effects of opposite sign and different time scales. Our nanocavities show self-induced oscillations in transmission, which we believe are provided by a negative—blue-shift—and slow thermo-mechanical effect within the nanobeam, and a positive fast—red-shift— thermo-optic nonlinearity (see model in section 3.3.3). The behavior of the nanocavity's transmission output signal are given by nonlinear thermal effects, and can be varied through the detuning $\delta\lambda$ and the injected optical power. A cycle of a full oscillation is described in Fig. 3.8 in section 3.3.3.

Experimentally, we recorded self-induced oscillations of the nanocavity's transmission for different powers and a fixed excitation wavelength at 0.5 mbar. If we inject powers P_{in} higher than 29 μW at the input coupler, as shown in Fig. 6.13, we obtain stable and periodic oscillations. We also observe that the period length increases with higher optical powers. Most of these oscillations have a total period Λ between 1 second and 9 seconds. This period time Λ can increase by further increasing the injection power. If we keep increasing the power, we can reach an excitation block[11], where the nanocavity stabilizes on the high transmission state (or "on" state) and its value saturates. The excitation block can be explained by the FitzHugh-Nagumo model [129, 130]. Another possible outcome from increasing P_{in} is that λ_{res} can blue-shift a few linewidths, resulting in no transmission from the nanocavity's output for a fixed excitation wavelength.

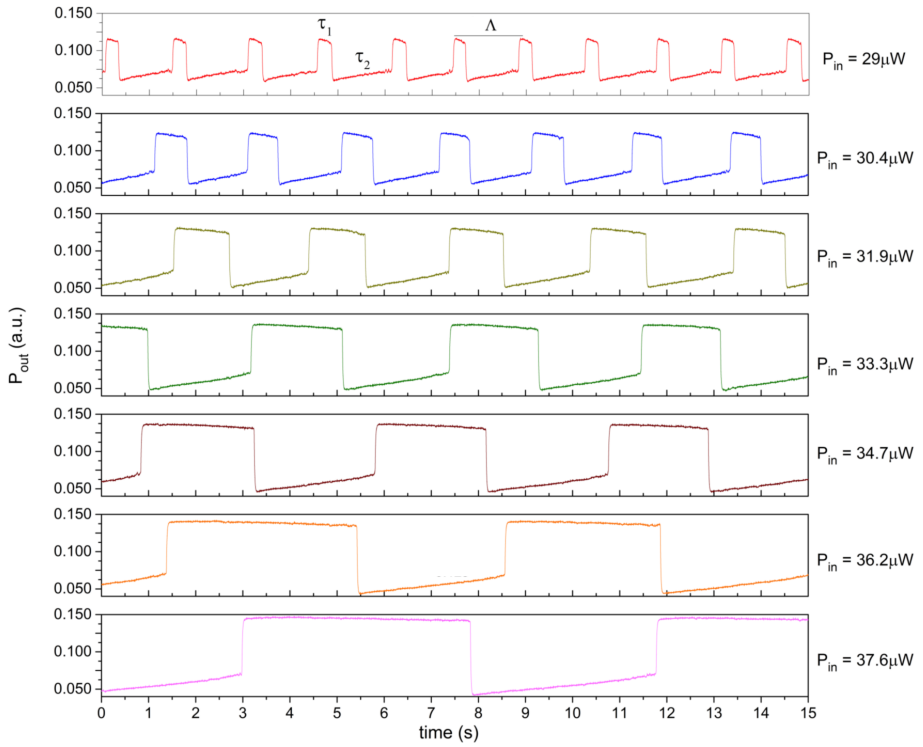

Figure 6.13: Time trace of the nanocavity's transmission for a $\delta\lambda = -0.13$ nm. The output power increases as well as the oscillation period's length Λ. We define τ_1 as the amount of time the nanocavity's transmission is on the "on" state, and τ_2 for the time on the "off" state

[11] Excitation block: phenomenon where repetitive spiking ceases as the amplitude of the stimulus current increases.

To quantify the time the system spends at the "on" state and "off" state in Fig. 6.13, we define τ_1 for the "on" state, and τ_2 for the "off" state. For higher P_{in}, τ_1 increases (see Fig. 6.14 a)). Although τ_2 also increases, it does so at a slower rate than τ_1. Therefore, for increasing powers, the nanocavity will spend more time on the "on" state than on the "off" state until it reaches the excitation block. We also observe that the period becomes longer for higher input powers in Fig. 6.14 b). The duration of these oscillations is similar to those observed in silicon nitride microdisks [83].

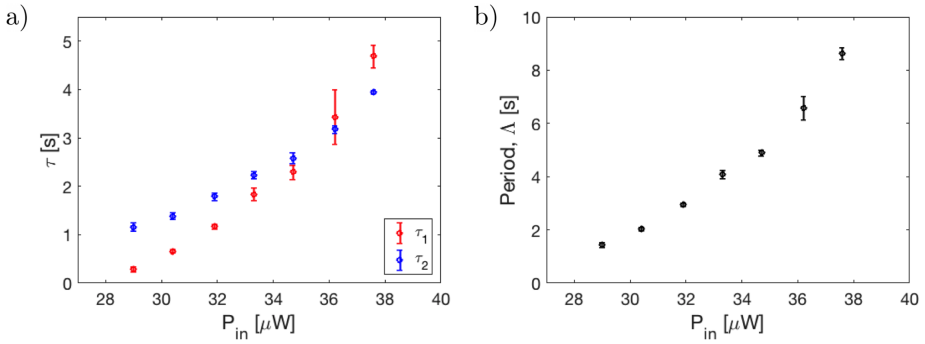

Figure 6.14: Nanocavity's τ_1 and τ_2 in a) and the full period Λ in b) from the time traces shown in Fig. 6.13. We observe that τ_1 increases faster than τ_2 for higher input powers. Λ also increases for higher input powers. Each data point represents the mean of τ_1, τ_2 and Λ for a given time trace at fixed input power. We estimate the error in τ_1, τ_2 and Λ by taking the maximum of the standard deviation and the duration of the rising and falling time for the time trace corresponding to each input power.

In Fig. 6.15, we show the timetrace of the nanocavity's output transmission as the injected power is decreased in several steps within a small range (from 28.3 μW to 24.7 μW). We begin by observing self-induced oscillations, and as we lower the input power, the periodic output becomes more and more irregular until the spikes become chaotic ($P_{\text{in}} = 25.4$ μW). These transmission pulses are excitable responses randomly elicited by the small remnant noise unavoidable in the experiment [131]. The transition from chaotic spiking to self-induced oscillations can also be explained with FitzHugh-Nagummo–like models [131].

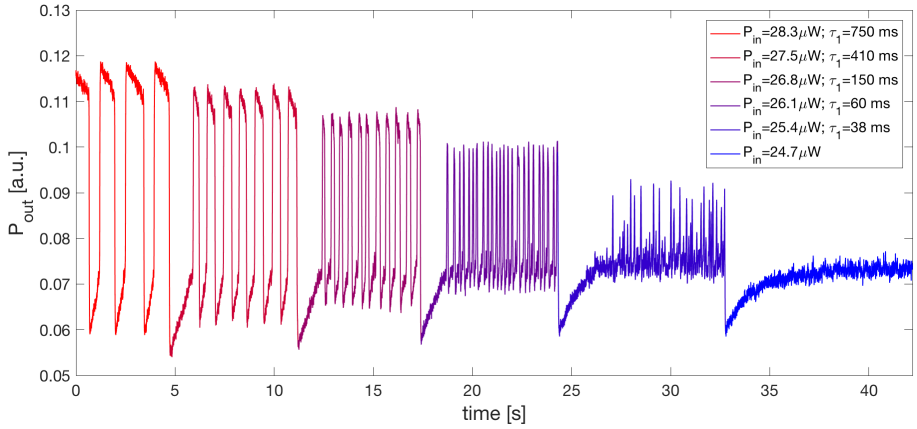

Figure 6.15: Timetrace of the nanocavity's transmissions for a fixed $\delta\lambda = -0.11$ nm. We observe how the period and amplitude of the oscillations decrease for lower powers until the oscillations become chaotic and stop. We define τ_1 as the time that the nanocavity's transmission is on the "on state".

The shape of the periodic oscillations starts to become irregular for powers below $P_{\text{in}} = 27.5$ μW, which corresponds to ~ 4 μW coupled into the PhC waveguide. For them to be regular, P_{in} should be higher than ~ 29 μW. Also, equivalent to what we observed in Fig. 6.13, the time length in the "on" state τ_1 is proportional to the injected input power P_{in} until the periodic oscillations cease.

6.6 Conclusions and outlook

As soon as we input light at the resonant wavelength λ_{res} into the nanocavity, the circulating radiation within gives rise to a temperature increase. We have studied and characterized the thermal behavior of the nanocavity's resonance for different heating sources: the trapping beam, the intra-cavity light, an external laser, and a heater. When the nanocavity heats up, we've observed a predominant blue-shift of -0.15 ± 0.05 nm/K which we believe is due to a thermo-mechanical effect that deforms the geometry of the nanocavity. This value of temperature sensitivity is comparable to current nanophotonic devices. To our knowledge, this is the first time that these effects are studied in a 1D photonic crystal nanobeam in Si_3N_4.

We have observed bistability in the nanocavity's transmission in two ways. First, by a deformation of the resonance's Lorentzian into a triangular resonance profile due to the thermo-optic effect. This allowed us to find a bistability threshold input power of 3 μW for a pressure of 0.5 mbar. In other

works, one of the main goals is to achieve bistable devices with the lowest power threshold possible. Currently, these values sit at 1.6 μW [68]. Second, we performed power scans for a fixed wavelength and observed the hysteretic response of the nanocavity's transmission. The "on" state and the "off" state in the cavity's transmission depend on the detuning from resonance and on the power injected into the nanocavity. These two variables determine the amount of energy delivered into the cavity, and therefore, how much its temperature increases. We've reached the "on" state of the hysteresis cycle at 0.5 mbar with a power of 11 μW coupled into the cavity. We've found that the value of the detuning $\delta\lambda$ is not reliable because the starting cavity's resonance λ_{res} varies between scans. This could be solved with faster scans, a possibility that is currently unavailable due to the limitations of our excitation laser. Also, we've observed that the heating performance of the dielectric mode and air mode nanocavities is very similar.

We have experimentally demonstrated self-induced oscillations in the nanocavity's output transmission—driven by a slow thermo-mechanical effect and a fast thermo-optic effect—at a pressure of 0.5 mbar with a minimum injection power of 29 μW at the input coupler of the structure, resulting in approximately ~ 4 μW coupled into the waveguide. We have also observed a dependence on the length of the period of the oscillations with both the detuning from resonance and the injection power. Furthermore, for low enough powers we observed chaotic behavior in the nanocavity's output.

Both bistability and self-induced oscillations are the main building blocks to develop photonic and all-optical circuits, allowing for more complex integrated photonic platforms. Moreover, since the nanobeam's thermal dynamics are very sensitive, it could perform well as a pressure or temperature sensor: either through the variation of resonance in temperature, the bistability power threshold or by an analysis of the self-induced oscillations.

Chapter 7

Levitodynamics with photonic crystal nanocavities

As we've discussed in previous chapters, for the optomechanical interaction to occur, the nanoparticle must be within the nanocavity's near-field. To ensure this, we require precision in manipulating the nanoparticle's position as well as a stable intra-cavity field—and therefore a stable high output transmission—through the photonic crystal nanocavity to measure the nanoparticle's dynamics through it.

This chapter weaves together many concepts and techniques from the previous chapters: control, manipulation, and detection of the levitated nanoparticle, and the design, characterization, and understanding of the thermal dynamics of the nanocavities. We begin by describing two proof-of-concept near-field experiments where we detect the levitated nanoparticle's dynamics in the overdamped regime through an optical fiber tip, and through a nanotaper at 4 mbar. Afterwards, we describe and explain the main achievements of the levitodynamics experiment with a nanocavity: we position the nanoparticle in the vicinity of the nanocavity's evanescent field and detect, with two different detection schemes, the motional dynamics of the nanoparticle through the nanocavity.

7.1 Preliminary near-field experiments

This section includes proof-of-concept experiments conducted before we began to fabricate the photonic crystal nanocavities on suspended silicon nitride membranes. These trials enabled us to develop and test a setup that was suited to approach the nanoparticle to the near-field of an optical waveguide.

7.1.1 Nanoparticle detection through a fiber tip

The first experiments were conducted in air, in the overdamped regime. The setup was confined inside a box—to avoid air currents—where we optically trapped nanoparticles of a diameter of 235 nm with 1064 nm light. We used Arduino controlled motors to approach the optical fiber tip to the levitated nanoparticle. We fabricated the fiber tips in-house at ICFO's clean room with a fiber puller Model P-2000 from Sutter Instrument Co. and from SM600 Thorlab fibers. The result is a fiber with two different ends: one end with a fiber tip and the other extreme is connectorized and couples light into an avalanche photodiode (Thorlabs APD110C/M).

In our first approaching experiments, the levitated nanoparticle was approached by the fiber tip up to $\sim$ 1 micron, considering surface-to-surface distance (see Fig. 7.1). We estimated the distance between them by first calibrating the focal plane given by the 100$\times$ objective, which is also used for trapping, with a sample of known size, thus we could measure the distance in pixels and convert it into units of distance.

We approached the fiber tip to the nanoparticle in two ways: from the front of the fiber tip and from the side. In the case of the front approach, we positioned the fiber tip at 950 ± 250 nm away from the nanoparticle. Light is coupled into the fiber tip from the particle's scattering, and we extracted the power spectral density (PSD) of the nanoparticle's motion from the signal that arrived to the detector. We obtained the typical PSD of an object in the overdamped regime (see section 2.1.2), where there is no natural frequency peak, and we can observe a corner frequency around 5 kHz. There is also a clear difference in the level of the signal between having a nanoparticle or not. Consequently, we've proved that we are able to get close enough to the optical probe to detect the nanoparticle's dynamics through the light that couples into the fiber tip via the nanoparticle's scattered light.

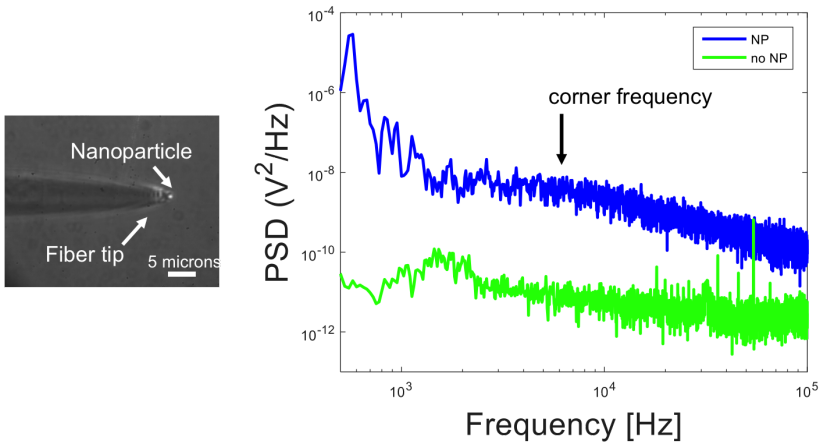

Figure 7.1: Left: image of the focal plane of the 100× objective where we see both the nanoparticle (NP) and the fiber tip. Right: PSD of the nanoparticle's dynamics in the overdamped regime when the nanoparticle is in front of a fiber tip. The scattered light from the trapped nanoparticle is coupled into the fiber tip. We observe a corner frequency of about 5 kHz.

For the side approach, we brought the fiber tip slightly closer to the nanoparticle: 750 ± 250 nm away. In Fig. 7.2 we show the PSD from the signal that is coupled into the fiber with and without particle. Once again, we see a clear difference of the level of the PSD signal along with the appearance of the corner frequency due to the overdamped motion of the levitated particle.

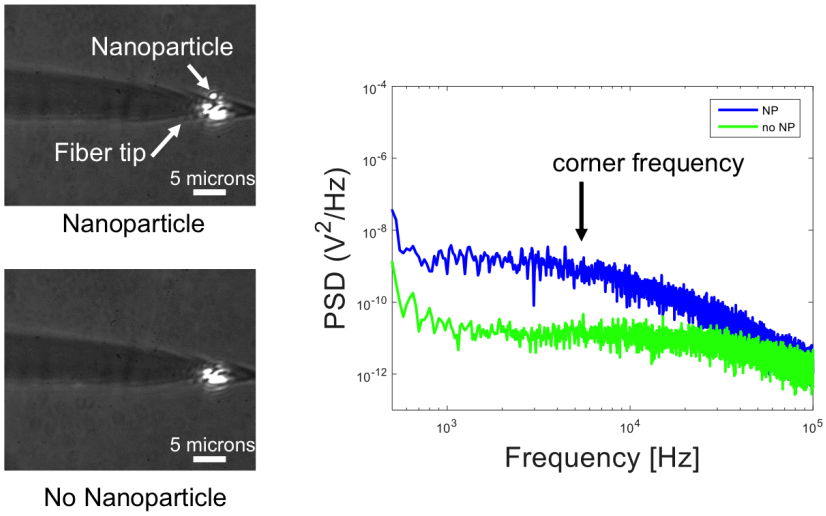

Figure 7.2: Nanoparticle detection in air through the side of a fiber tip. The scattered light from the trapped nanoparticle is coupled into the fiber tip, and we detect it through the other side of the fiber. We also observe a corner frequency of about 5 kHz.

After observing the overdamped motion, we decided to optically drive the nanoparticle—inducing it to oscillate at a known frequency—to detect a direct signature of its dynamics. Hence, we superimposed a 532 nm laser (with 0.45 mW in power) to the trapping beam. We used 200 mW for the 1064 nm trapping beam and modulated its intensity by 60% with an AOM: 80 mW of power was in the 0th diffraction order—to always provide enough power for a stable trap—and the remaining 120 mW oscillated between the 1st and 0th diffraction order at a set frequency. We pursued the approach from the side, and the fiber tip was positioned at 750 ± 250 nm close to the nanoparticle's surface. On the detector, we included a notch filter to block 1064 nm radiation to ensure that we just detected the proble light from the 532 nm laser. Moreover, we changed the intensity modulation frequency of the trapping light to 2 kHz, 3 kHz, and 4 KHz. The PSDs in Fig. 7.3 show an overdamped driven motion of the nanoparticle's dynamics where the peaks are given by the motion of the particle at the frequency set by the applied intensity modulation. Differences in the peaks' width are due to the logarithmic scale of the graph.

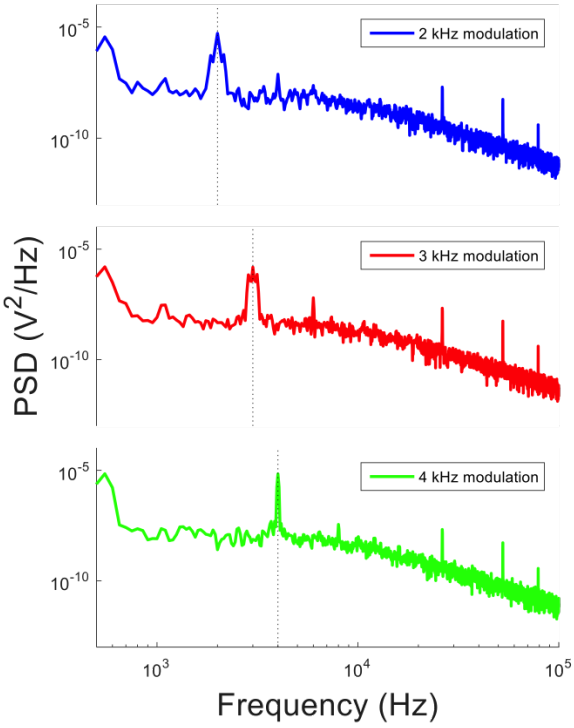

Figure 7.3: PSD of optically driven nanoparticle in the overdamped regime. We detected the signal from the scattered light of the particle coupled into the fiber tip from the side. Trapping occurs with 1064 nm light and detection with 532 nm light. The difference in the peaks' width are due to the logarithmic scale of the graph.

In these set of experiments with a simple setup, we have successfully measured the dynamics of a levitated nanoparticle in the overdamped regime, with and without driving, by coupling the light scattered by the particle into the optical fiber tip. These preliminary tests have provided a first notion to approach and detect nanoparticles through an optical probe.

7.1.2 Nanoparticle detection through a tapered fiber

After the results obtained with fiber tips, we moved to work with nanotapers. Our goal with this experiment was to gain knowledge on how to control the position of the nanoparticle when approaching it to a tapered fiber. To this purpose, we implemented a $4f$ system in our setup to control the position of the nanoparticle optically (see section 5.4.1). The $4f$ system allows us to freely move the nanoparticle within the focal plane of 100× objective—

we vary the trapped nanoparticle's position along the laser's propagation axis—without losing the alignment at the objective's back aperture. We've also measured the nanoparticle's dynamics through its interaction of the nanotaper's evanescent field (see Fig. 7.4).

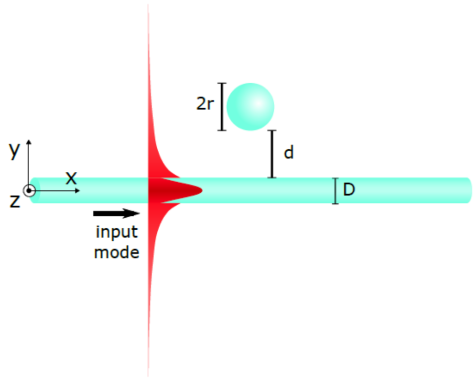

Figure 7.4: Diagram for nanoparticle of radius r at a distance d to a tapered nanofiber of diameter D.

This study was completed in collaboration with the Takeuchi Lab from Kyoto, Japan. They provided us with nanotapered fibers with a diameter between 500-600 nm made from single mode fibers on a mount already compatible with our setup. Here, we levitated 304 nm diameter particles with a 1064 nm laser at 100 mW, in a low vacuum of 4 mbar. We decided to use larger particles (compared to the 235 nm ones) to facilitate the detection of the nanoparticle's motion. Although there is no cavity in this case, the interaction of the nanoparticle with the near-field is $\propto \frac{V_\mathrm{p}}{V_\text{near-field}}$, where V_p is the volume of the nanoparticle and $V_\text{near-field}$ is the volume corresponding to the near-field [116]. Therefore, the larger the nanoparticle, the greater the overlap and interaction with the nanotaper's evanescent field for a fixed distance between them. We brought the nanoparticle at distance of $\sim 1\,\mu$m to the nanotaper (measured from the focal plane image as before and shown in Fig. 7.6). This distance was the minimum distance we could reach without losing the particle. We coupled 1550 nm light into one of the tapered fiber's ends, and the other end went directly into an avalanche photodiode (Thorlabs APD110C/M) for detection.

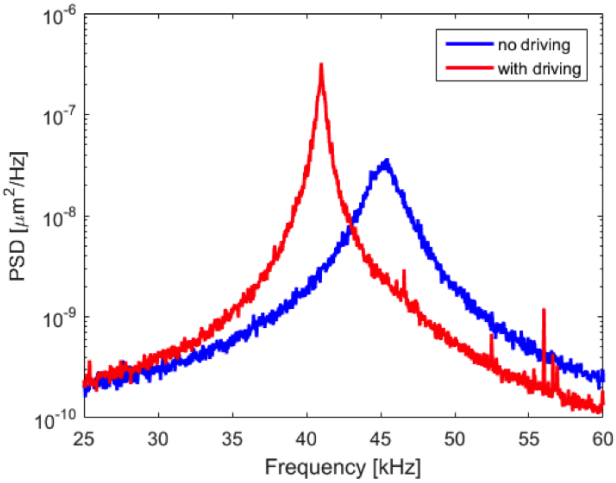

Figure 7.5: PSD of the nanoparticle's motion along z detected from the backscattered light with a QPD. We plot the particle's natural oscillation frequency (blue) and the particle's parametric driven oscillation frequency (red). By comparing the areas under each peak we obtain an increase of ≈ 50 nm in the oscillation amplitude of the nanoparticle (see section 2.1.1).

The nanoparticle was parametrically driven at twice its natural frequency along z ($2 \times f_z$ kHz), which we could monitor through the PSD as we performed the measurement, with an AOM to: 1) increase the amplitude of the nanoparticle's oscillation, and 2) to ensure we detected the signature of the nanoparticle through the nanotaper and not the intensity modulation of the trapping laser. We estimated an oscillation amplitude of 50 nm without driving by calculating the area under the oscillation peak and finding the variance of the nanoparticle's position along z (see section 2.1.1). With the AOM parametric driving, we increased it to ≈ 100 nm (see Fig. 7.5). From here, we approached the nanoparticle to the tapered fiber and observed a peak in the PSD of the photodiode's signal, which is shown in Fig. 7.6. The natural frequency along the z motion can vary when approaching the nanoparticle to the nanotaper (from 45 kHz to 100 kHz as shown in Fig. 7.5 and Fig. 7.6, respectively). This difference is caused by standing waves created from the interference of the incoming trapping beam with its reflection at the nanotaper's surface. The standing waves give to a rise series of optical potential wells where the trapping intensity is higher, and therefore, the oscillation frequency of the nanoparticle increases [177].

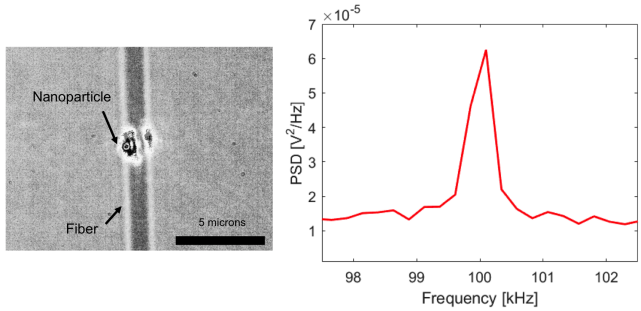

Figure 7.6: Left: focal plane image of the 100× objective where we see the levitated nanoparticle in close proximity to the nanotaper. Right: zoom in of the PSD where we observe the peak of the nanoparticle's motion along z at 100 kHz at 4mbar. The nanoparticle is parametrically driven at 200 kHz with an AOM. The frequency of the z motion is higher than in Fig. 7.5 because of the standing wave formed as we approached the nanotaper.

The photodiode included a notch filter for 1064 nm to avoid light from the trapping beam to couple into the tapered fiber. Also, as part of a general protocol, and due to the low signal-to-noise ratio, we re-checked that there weren't any electronic leaks from the AOM going into the detector, or any cross-talk between detectors.

This proof-of-principle shows that we can interact with the near-field of a photonic structure by optimally positioning the levitated particle (see Fig. 7.6). To continue the study of the near-field interaction of a nanoparticle with a nanocavity, we began to fabricate nanocavities on the nanotapers with a focused ion beam (FIB) as shown on Fig. 7.7. However, the nanotapers oscillated within the FIB, and although we left them the night before inside the chamber to stabilize, they would still vibrate during the exposure. This made fabricating on them very challenging and out of reach. Moreover, at this time we began fabricating the photonic crystal nanocavities on Si_3N_4 membranes. The membranes were more robust than the nanotapers and the fabrication on silicon nitride was systematic, so we continued to fabricate nanocavities on-a-chip instead of on nanotapers.

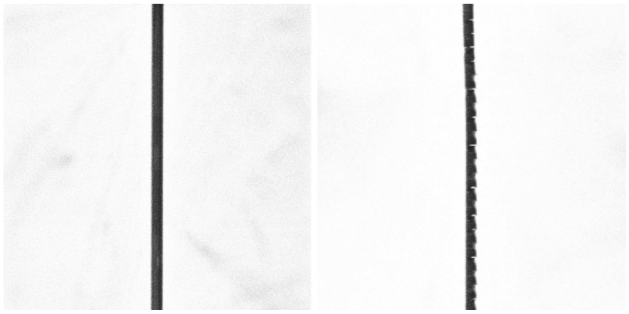

Figure 7.7: FIB images of a 500 nm diameter tapered fiber before (left) and after exposure (right).

7.2 Nanoparticle approach to nanocavity

With the pre-cavity experiments explained in section 7.1, we have developed the tools to optically approach a nanoparticle to a photonic structure. From now on, the photonic structure that we approach with a nanoparticle is a photonic crystal nanocavity fabricated in-house (see section 5.3).

The following experiments were completed in the setup described in section 5.4. To begin, we loaded a single 235 nm in diameter silica nanoparticle into the 1064 nm optical tweezer at 80-100 mW. Once the nanoparticle is trapped, we sealed the chamber, pumped down in pressure to 0.5 mbar[1], approached, and aligned the 1D photonic crystal nanocavity with the piezos to couple light into it with the 1550 nm tunable laser.

The first and most important condition we need to perform the measurements is a stable intra-cavity field of the nanocavity. From what we've learned in chapter 6, we need to stabilize the nanocavity's resonance by reaching the excitation block.

In our first experiments, the Cobrite laser coupled light into the nanocavity as shown in section 5.4.2. To obtain a stable output transmission, we heated up the nanocavity by repeatedly exciting it on resonance with $P_{\text{in}} \approx 0.5$ mW in front of the input coupler until reaching λ_{final}; at this point the system enters into self-induced oscillations. From here, we increased the input power to achieve the excitation block and arrive to the high transmission or "on" state (see Fig.7.8) where λ_{res} is stable. This state is blue-detuned from resonance $\approx \Delta\lambda/2$, where $\Delta\lambda$ is the linewidth of the nanocavity [66].

[1] 0.5 mbar is a pressure region where we can clearly see the natural frequencies of the nanoparticle and do not need to implement any type of feedback mechanism to avoid particle loss.

The nanocavity can remain in the excitation block for hours, or even days if the pressure remains constant and the piezos don't shift and modify the alignment. We can't change the detuning given by the excitation block because the Cobrite laser turns off if we vary the wavelength.

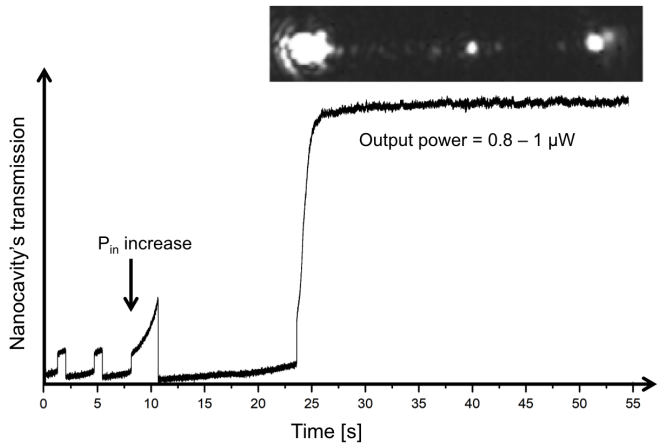

Figure 7.8: The nanocavity undergoes an excitation block: departing from the self-induced oscillations state it reaches the high transmission state as we increase the input power from 0.45 mW to 2.9 mW. On the top: image of IR camera showing the nanocavity when it is excited on resonance, thermally stable, and under excitation block.

To measure the nanoparticle's dynamics, this excitation block or "on" state must not be lost while we approach the 235 nm silica nanoparticle to it. As we performed the approach, we observed the nanocavity's transmission lower to about half of its initial value (see Fig. 7.9). This is due to the trapping beam providing additional heating to the nanocavity, further shifting λ_{res}. Although this decrease in transmission is a result of the nanocavity's resonance shifting ≈ 0.1 nm[2], the excitation block state is maintained. We recall that the thermo-optic deformation effectively increases the linewidth of the cavity (see section 6.4.1), which is why we still had transmission through the nanocavity. These are the experimental conditions in which we performed the homodyne detection experiments shown in section 7.4.1. In the end, because we were not probing the cavity on resonance, we don't expect homodyne detection to operate at its best sensitivity, as earlier discussed in section 5.4.2. This is due to the detuning from the thermal nonlinearities, the thermo-optic deformation of the resonance, and the offset provided by the trapping laser.

[2]We estimate this value from the decrease of the nanocavity's transmitted power, which happens at half of $\Delta\lambda/2$.

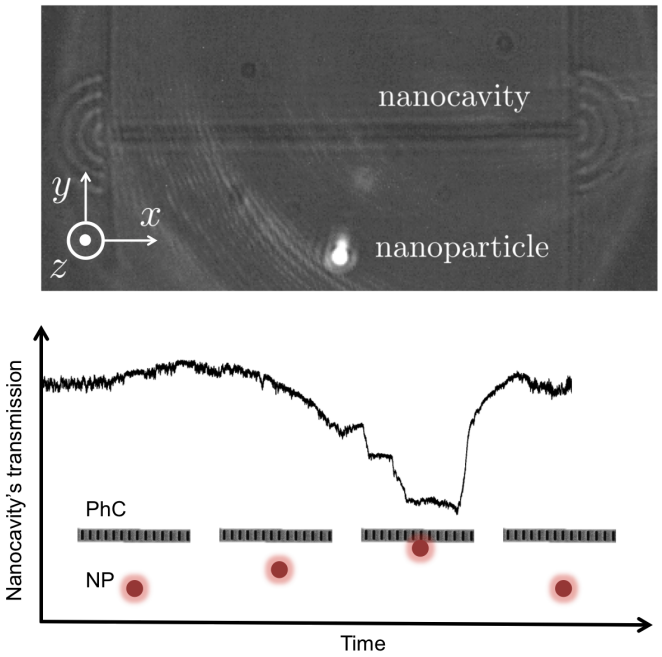

Figure 7.9: Top: Focal plane image of the 100× objective showing both the nanocavity and nanoparticle. Bottom: we approach the nanoparticle to the nanocavity when it is thermally self-locked to the "on" state (excitation block state). The nanocavity's transmission lowers as the nanoparticle is approached, as shown with the diagram of the nanoparticle (NP) and photonic crystal cavity (PhC), yet remains in the same high transmission state. Once we bring the nanoparticle away from the nanocavity, we recover the original transmission value.

One of the weaknesses of our nanoparticle to nanocavity approach is that we don't have a reliable method to measure with the desirable resolution and accuracy the distance between them. Although the IR camera provides an image of the approach, we are unable to estimate a distance under $\approx 1\,\mu$m away from the structure.

7.3 Signal calibration and g_0 estimation

We've mentioned along various sections how g_0 is a figure of merit in optomechanical systems. In this section we describe the method [178] we use to estimate the optical frequency shift per displacement $G = \frac{\partial \omega_c(x)}{\partial x}$, and later the single-photon optomechanical coupling strength g_0, in our experiments.

From [178], we may express G in the frequency domain as:

$$G(w)^2 = \frac{S_\omega(\omega)}{S_x(\omega)}, \tag{7.1}$$

where $S_\omega(\omega)$ and $S_x(\omega)$ are the power spectral densities (PSDs) of the transmitted signals through the nanocavity in units of frequency and distance, respectively. If we integrate for both PSDs and apply Parseval's theorem (see section 2.1.1), equation (7.1) becomes:

$$G^2 = \frac{\int_{-\infty}^{\infty} S_\omega(\omega)\mathrm{d}\omega}{\int_{-\infty}^{\infty} S_x(\omega)\mathrm{d}\omega} = \frac{\langle \delta\omega_\mathrm{c}^2(t)\rangle}{\langle \delta x^2(t)\rangle}, \tag{7.2}$$

where $\langle \delta x^2(t)\rangle = \frac{k_\mathrm{B}T}{m\omega_\mathrm{m}^2}$ is the variance of displacement fluctuations of the nanoparticle and $\langle \delta\omega_\mathrm{c}^2(t)\rangle$ is the variance of frequency fluctuations of the nanocavity.

In the experiment, since we typically extract our PSDs in units of volts, we need to convert them into units of frequency, to obtain $\langle \delta\omega_\mathrm{c}^2(t)\rangle$. For this unit conversion, we apply a known frequency modulation (FM) to the laser beam that is transmitted through the nanocavity. This modulation is generated by applying a known AC signal of voltage amplitude V_in, directly to our laser source[3], which has a known FM response expressed by a transfer coefficient c_L (in MHz/V). This transfer coefficient converts our measurements from volts to frequency units. With V_in and c_L, we can generate a peak—which we refer to as calibration peak—in the PSD in the vicinity of the frequencies we are interested in (i.e. the nanoparticle's oscillation frequency).

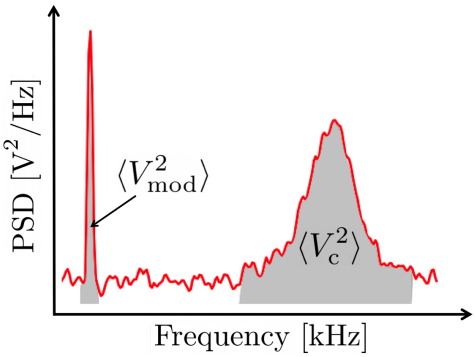

Figure 7.10: PSD showing the calibrations peak and the peak corresponding to the nanoparticle's dynamics. $\langle V_\mathrm{mod}^2\rangle$ is the area under the calibration peak and $\langle V_\mathrm{c}^2\rangle$ is the area under the peak given by the near-field interaction with the nanoparticle.

[3]Through an analog input into the laser PZT driver circuit.

As we show in Fig. 7.10, we complete the calibration by comparing the area under the two peaks in the PSD: $\langle V_c^2 \rangle$ given by the near-field interaction with the nanoparticle, and $\langle V_{mod}^2 \rangle$ given by calibration peak. By proportionality,

$$\langle \delta\omega_c^2(t) \rangle = \langle V_c^2 \rangle \frac{V_{in}^2 c_L^2}{\langle V_{mod}^2 \rangle}. \tag{7.3}$$

Replacing $\langle \delta\omega_c^2(t) \rangle$ on the right hand side of equation (7.2), we calculate G as:

$$\begin{aligned} G^2 &= (2\pi)^2 \frac{\langle \delta\omega_c^2(t) \rangle}{\langle \delta x^2(t) \rangle} \\ &= \frac{m\omega_m^2}{k_B T} \langle V_c^2 \rangle \frac{V_{in}^2 c_L^2}{\langle V_{mod}^2 \rangle}. \end{aligned} \tag{7.4}$$

From here on, defining $g_0^2 = G^2 x_{ZPF}^2 = G^2 \frac{\hbar}{2m\omega_m}$, we obtain:

$$g_0 = 2\pi \sqrt{\frac{\hbar\omega_m}{2k_B T} \langle V_c^2 \rangle \frac{V_{in}^2 c_L^2}{\langle V_{mod}^2 \rangle}}. \tag{7.5}$$

7.4 Nanoparticle near-field detection

In the next series of experiments, we have followed the procedure reported in section 7.2 and calculated g_0 as explained in section 7.3. Before loading the particle into the optical trap, we first characterized and selected the best nanocavities within the fabricated sample. Our selection criteria was: a high transmission for the resonant wavelength, and that they must display the thermal behavior—excitation block—we've discussed in chapter 6.

7.4.1 Balanced homodyne detection

In this section we measure the nanoparticle's dynamics by measuring fluctuations in the phase of the nanocavity's transmission. As we described earlier in section 7.2, we used the Cobrite 1550 nm tunable laser and the optical setup described in 5.4.2 to heat the nanocavity by exciting it on resonance until reaching the self-induced oscillations regime. From here, with an increase in input power, we reach the excitation block and the nanocavity's resonance stabilizes. We also refer to this state as a "thermal self-lock". We performed the experiment under these stable intra-cavity field conditions. Unfortunately, in this stable state the excitation laser was always detuned with respect to the cavity's resonance and, since we could not further change

the laser wavelength without losing the thermal self-lock[4] we could only perform homodyne detection in such detuned state (see section 5.4.2).

After the thermal self-lock, we approached the nanoparticle to the nanocavity, which we identified through the IR camera as the bright central spot shown in the top part of Fig. 7.8. We carefully optimized the position of the nanoparticle with respect to the nanobeam by using the $4f$ system and by varying the trapping beam's collimation to control the nanoparticle's position along the laser beam's propagation axis z (see section 5.4.2). The nanoparticle was approached to the nanobeam until we obtained the best signal-to-noise ratio possible, or we lost the particle. Nanoparticle loss can occur due to misalignment from varying the nanoparticle's position with the $4f$ system. This misalignment at the back aperture of the objective decreases the trap's optical power: it makes the trapping potential shallower such that the particle often escapes. As we approached the nanoparticle to the nanocavity, we created reflections and also blocked the trapping beam with the nanobeam. All these disturbances modify the optical potential and, if large enough, can lead to nanoparticle loss too. Furthermore, any variations in the amount of intensity of the trap results in a variation of frequency of the nanoparticle's oscillations.

In the following we describe the balanced homodyne detection result of the nanoparticle's motion through the two dielectric mode designs of the nanocavity: the fundamental (defect cells $D = 11$) and second mode nanocavity (D=19).

Fundamental mode nanocavity (dielectric mode design)

After carefully approaching the nanoparticle to the nanocavity, and optimizing the signal-to-noise ratio by varying the particle's position with respect to the nanobeam, we measured the nanoparticle's dynamics through the nanocavity's output transmission.

[4]This is because the Cobrite laser doesn't provide continuous tunability, thus briefly turns off when the wavelength is changed.

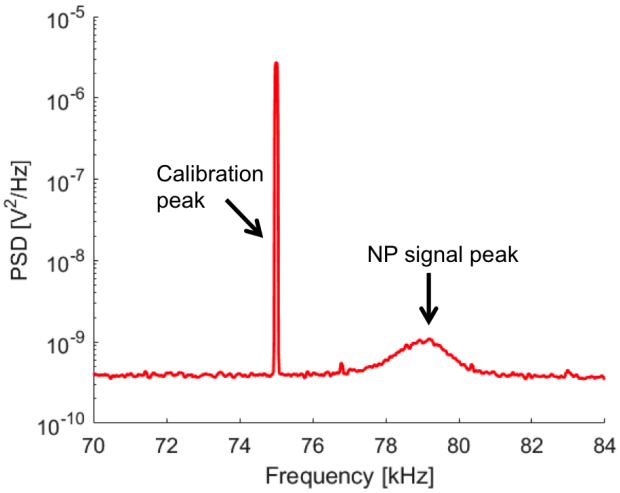

Figure 7.11: PSD of the output signal from the nanocavity in balanced homodyne detection. We have a calibration peak at 75 kHz and another peak given by the z motion of the nanoparticle at 79 kHz.

In Fig. 7.11 we show a PSD of the output signal from the cavity where we see both the calibration peak at 75 kHz and the peak associated with the nanoparticle's motion along z at 79 kHz. We used the calibration peak to calculate g_0 as shown in section 7.3. In this case, we send to the Cobrite laser's FM input a sinusoidal signal of amplitude $V_{\text{in}} = 10$ mV and frequency 75 kHz to generate the calibration peak. The frequency modulation transfer coefficient for this frequency range is $c_{\text{L}} = 15$ MHz/V. The signal to noise ratio (SNR) for the nanoparticle's signal through the nanocavity is slightly over 2. This low SNR is partially caused by the trapping beam, which heats the nanocavity and shifts its resonance as we approached the nanoparticle to it, reducing the amount of power arriving at the detector. Furthermore, such detuning limits the sensitivity of our phase detection.

After performing the calibration, following the steps detailed in section 7.3, we calculated a value of $g_0 \approx 2\pi \cdot 1$ Hz. This value is much lower than expected from the simulations in section 5.2.6. We believe that one of our limitations lies in that we are not close enough to the nanobeam. In our current experimental setup we don't have a precise way to measure the distance from the nanoparticle to the nanocavity. Although the sample is on a piezostage, we can't use it for this purpose. This is a consequence of using the 100× objective both to trap the nanoparticle and excite the nanocavity: once the nanocavity is aligned, the piezos can't be moved. Therefore, we would need to couple light into the structure differently to gain this degree

of freedom: through a re-design of the nanocavity's coupling with a tapered fiber, a fiber tip or end-fiber coupling. A change in the coupling technique could also help improve the current coupling efficiency: allowing the use of less input power, enabling to excite the nanocavity on resonance, and reducing thermo-optic effects [120].

Second mode nanocavity (dielectric mode design)

Just as we completed the nanoparticle detection measurement for the fundamental mode nanocavity, we repeated the experiment with another cavity design: the second mode nanocavity shown in section 5.2.3. In this case, we detected the nanoparticle's dynamics (see Fig. 7.12) through both of the illuminated spots towards the middle of the nanobeam. We have detected the motion of the nanoparticle along the z axis through each lobe. The nanoparticle's motional frequencies are different between each other (37 kHz and 40 kHz) because the trapping potential has varied due to the new position of the nanoparticle[5].

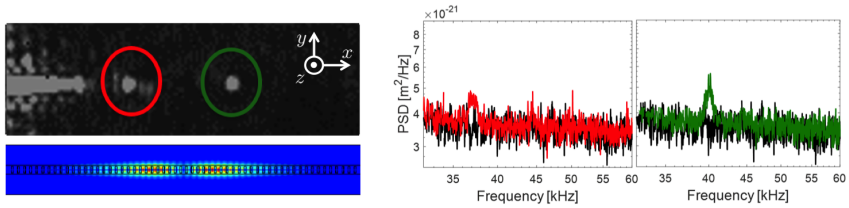

Figure 7.12: PhC design with the second mode available in the wavelength range of our laser. Left: image of the PhC nanocavity thermally stable, showing the two intensity maxima, and simulation of the structure below. Right: PSD of the measurement of the nanoparticle's dynamics through the nanocavity for both maxima or lobes (color coded). The black line shows the PSD of the nanocavity's transmission when the nanoparticle is away.

This experiment proves that we can detect the nanoparticle's dynamics with either the fundamental mode or the second mode nanocavities (dielectric mode design). Moreover, the second mode nanocavity allows to detect at two locations: either through the left or right lobe. In the future, this could enable coupling two levitated nanoparticles through a photonic crystal cavity.

[5]The motional frequency of the trapped object is proportional to the optical intensity at the trap.

7.4.2 Direct detection

From detecting variations in phase of the nanocavity's output signal, we changed our detection to measure fluctuations in the nanocavity's transmission's amplitude—intensity fluctuations. We adapted our setup to what we will refer as a direct detection scheme. We've already shown that the excitation wavelength is always detuned from resonance when the nanocavity is thermally self-locked, so a direct detection is more sensitive under these conditions. We continued to use the second mode nanocavity for these experiments (see section section 5.2.3). We also changed lasers and used the Tunics tunable laser instead of the Cobrite; with the Tunics laser it is straightforward to drive the cavity into the thermal self-lock state thanks to its continuous tunability. In addition, as we approached the nanoparticle we could now compensate for the shift given by the heating from the 1064 nm by readjusting the nanocavity's excitation laser's wavelength without the risk of loosing the thermal self-lock state. We used the same balanced detector from the balanced homodyne detection, but just one of the two input ports. In Fig. 7.13, we observe both the far-field and near-field detection and show the frequency peaks related to the motion of the nanoparticle (see section 5.4). For the far-field detection, we collected the backscattered light of the nanoparticle at the QPD. We observe all the frequencies related to the motion of the particle along x, y, and z, plus higher order harmonics like $2f_z$ or $f_x - f_z$, which we show in Fig. 7.13 a).

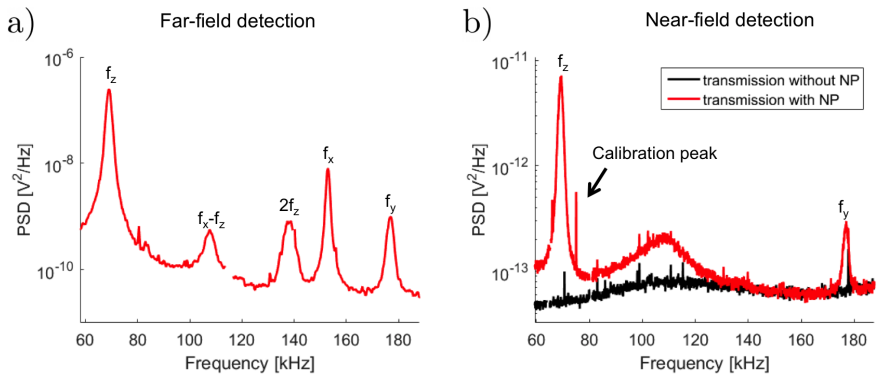

Figure 7.13: PSD of the far-field and near-field measurement of the nanoparticle's dynamics in direct detection. a) The far-field detection is given by the backscattered light of the nanoparticle collected by the QPD. We observed the peaks related to the dynamics of the nanoparticle as well as some harmonics: $f_z = 69$ kHz, $f_x = 153$ kHz, $f_y = 177$ kHz, $2f_z = 138$ kHz, and $f_x - f_z = 108$ kHz. b) In the near-field detection, we measured the nanoparticle's dynamics through its interaction with the right lobe of the second mode nanocavity (dielectric mode design), via the cavity transmission signal. The calibration peak is at 75 kHz. We observed the frequencies corresponding to f_z and f_y, but not f_x. In both graphs we have eliminated peaks that correspond to electrical noise.

In the near-field detection, we measured the nanoparticle's dynamics through its interaction with the right lobe of the second mode nanocavity (dielectric mode design), via the cavity transmission signal. By measuring fluctuations in intensity of the light transmitted through the nanocavity and calculating the PSD, we observe that the z peak is the one with the largest amplitude at a frequency of 69 kHz, and the y one is at 177 kHz (see Fig. 7.13 b)). We do not observe the motion of the nanoparticle along x, we believe this is because the nanoparticle is placed either where the nanocavity's gradient near-field is close to zero or not close enough to the nanocavity.

To obtain g_0, we placed a calibration peak at 75 kHz by including an AOM driven with a VCO [6] into the 1550 nm laser path to add a modulated frequency shift. To do so, we aligned the setup so that the 1st diffracted order of the AOM arrived to the nanocavity's input coupler. We applied a 10 mV voltage to the VCO, which was then attenuated by 4 orders of magnitude, so that $V_{\text{in}} \approx 1\mu$V. The frequency modulation transfer coefficient for this frequency range is $c_{\text{L}} = 4$ MHz/V. We obtained $g_0 \approx 2\pi \cdot 1$ Hz for both axes of motion, value which is consistent with the homodyne detection results. We

[6] Voltage-controlled oscillator (VCO): electronic oscillator whose oscillation frequency is controlled by a voltage input. It can be used for frequency modulation by applying a modulating signal to the control input.

also observed similar results by detecting through the first (or left) bright lobe of the nanobeam (same nanocavity design shown in Fig. 7.12).

By approaching the nanoparticle closer to the nanobeam, we managed to detect all three axes of motion: the z peak is at a frequency of 68 kHz, and the x and y are at 151 kHz, and 169 kHz, respectively (see Fig. 7.14 a) and b)). We also observe a wide peak centered at 110 kHz in Figs. 7.13 b) and 7.14 which seems to be related to the nanoparticle's presence. For this measurement, we set the frequency of the VCO at 64 and 160 kHz (the latter is visible in Fig. 7.14 b)). With the calibration peak for each case, we calculated $g_0 \approx 2\pi \cdot 1$ Hz for the z axis and $g_0 \approx 2\pi \cdot 0.5$ Hz for x and y.

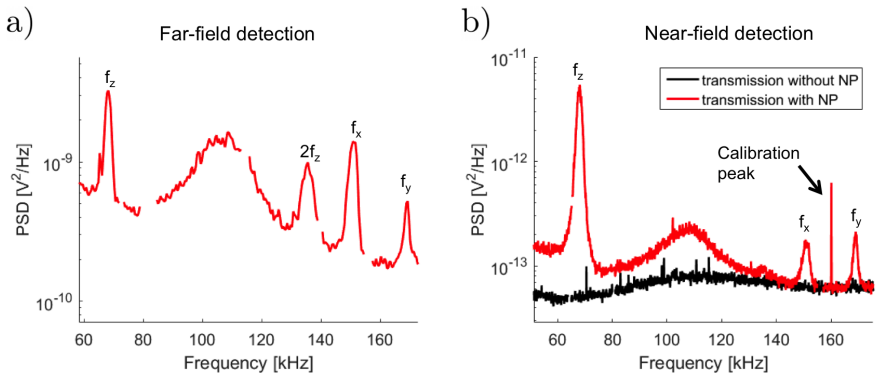

Figure 7.14: PSD of the far-field and near-field measurement of the nanoparticle's dynamics in direct detection. a) The far-field detection is given by the backscattering light of the nanoparticle on the QPD. We observed the peaks related to the dynamics of the nanoparticle as well as some harmonics: $f_z = 68$ kHz, $f_x = 151$ kHz, $f_y = 169$ kHz, and $2f_z = 136$ kHz. b) In the near-field detection, we measured the nanoparticle's dynamics through its interaction with the right lobe of the second mode nanocavity (dielectric mode design), via the cavity transmission signal. The calibration peak is at 160 kHz. We also observed the frequencies corresponding to f_z, f_x, and f_y through near-field detection. In both graphs we have eliminated peaks that correspond to electrical noise.

If we compare the result from the far-field and near-field detection (shown in Fig. 7.13 and Fig. 7.14), depending on the position of the nanoparticle respect to the nanocavity, we obtain the same information from the nanoparticle's dynamics. The difference in the PSD level is caused by the difference in optical power of the detection beam: $\sim$ 1 mW in the case of far-field detection and $\sim 1\mu$W in the case of near-field measurement.

We can now also compare the signals obtained through direct detection and homodyne detection. The direct detection measurements show a higher

SNR compared to the homodyne ones. In the homodyne measurement we had a lower SNR because we could not tune the wavelength nor improve the output transmission of the nanocavity. However, both detection schemes are affected by the detuning provided by the thermal self-lock and by the thermo-optic deformation of the cavity's resonance—resulting in an increase in its linewidth. We believe the detection of intensity fluctuations (direct detection) provides a better signal-to-noise because the detection scheme's sensitivity performs well when detuned from resonance. Although we can't alter the detuning given by the thermal self-lock, we were able to achieve a higher SNR and nanocavity output transmission compared to the homodyne experiment.

7.5 Limitations and future developments

There are three main limitations in our experimental setup. First, we are limited by the thermal dynamics of the nanocavity: there is a given detuning provided by the thermal self-lock, as well as the thermo-optic deformation of the cavity's resonance which increases its linewidth. A solution could be to change the coupling technique. This would also enable to move the nanocavity freely without affecting the in- and out-coupling conditions. Currently, the same 100× objective both traps and couples light into the nanocavity. Another option would be thermally lock the nanocavity with one laser, and probe with another one. We've tried this, but the probing laser takes over the thermal dynamics in order to observe a signal from the nanocavity. Also, being able to come closer and reducing the input power would also help to experimentally reach similar g_0 values that we've obtained in simulations. Plus, it could provide a direct distance read-out between the nanoparticle and nanocavity given by the piezo, information that we currently lack from our experimental system.

The second limitation is that the trapping beam is continuously affected by the nanobeam as we approach the nanoparticle to it. We create reflections and we physically block it as it partially overlaps with the nanostructure. This can decrease the trap's depth and lead to particle loss. A solution could be to trap in front of the nanobeam and benefit from the standing waves, created from the nanobeam's reflection [120].

However, if we approach from the front of the nanobeam, our nanocavities burn—our third limitation. Improvements in the nanocavity's cleanliness as well as better quality Si_3N_4 could help. Until now, if we focused the 1064 nm trapping beam at the center of the nanobeam, we obtained a threshold burning power of 13 ± 4 mW at a pressure of 0.5 mbar (further

analysis shown in Appendix A). We define the burning power threshold as the power that destroys the nanocavity by using a laser beam focused to a size of ≈ 2 μm. This is why we approached the nanoparticle from the nanobeam's side. Also, fabrication is completed on low stress membranes, and for instance, high stress ones have lower absorption both for 1064 nm and 1550 nm. This would help reduce the heating. Furthermore, we could trap with a 1550 nm laser since absorption for Si_3N_4 is two times less when compared to 1064 nm.

7.6 Conclusions and outlook

Through a series of various experiments, we've shown near-field coupling of a levitated nanoparticle to different photonic structures. We've detected the dynamics of a levitated nanoparticle's in the overdamped regime through a fiber tip, and also through a tapered fiber at a pressure of 4 mbar. With these preliminary experiments, we achieved the know-how to manipulate levitated nanoparticles and we proved that they can interact with the near-field of a photonic structure.

We've worked with two types of detection, balanced homodyne and direct detection, to measure the nanoparticle's dynamics through a suspended nanocavity in silicon nitride. We found an experimental protocol to stabilize the intra-cavity field and carry out the experiment.

In the case of the balanced homodyne detection, we were limited in sensitivity by the detuning given by the thermal self-lock, also referred to as excitation block. Additionally, the nanocavity's resonance shifts further as we approach the nanoparticle with the 1064 nm trapping laser to it because of heating. This also reduces the nanocavity's output transmission. We've shown detection through the fundamental mode dielectric nanocaviy design as well as with the second mode nanocavity (dielectric mode design). For direct detection, the wavelength tunability of our laser gave us more flexibility to optimize the nanocavity's transmission, which allowed for a higher signal-to-noise ratio. We detected the nanoparticle's motion along the three axes. However, in both cases we were limited by the thermo-optic deformation of the resonance and the excitation block state. For the two detection schemes, we estimated a g_0 of $\sim 2\pi \cdot 1$ Hz along the different axes.

Recent experiments [120], also show a 1D Si_3N_4 photonic crystal nanobeam "glued" onto an optical fiber tip with an optomechanical coupling $g_0 \approx$ 10 kHz. This value is three orders of magnitude larger than macro-cavities. In this work [120], the authors claim that the capabilities of this system would improve if mounted in an on-a-chip device: both for thermal dissi-

pation and mechanical support; which would result in better experimental mechanical stability and would enable a higher intra-cavity photon number. In their experiment the input power is also limited due to thermo-optical effects [120].

Our experiment is very similar to the one described in [120], but already on-a-chip. However, our g_0 is lower than expected. We believe that it is mostly because we need to bring the nanoparticle closer to the nanocavity's near-field, and we also suffer from the thermo-optic effect—the nanocavity's linewidth is increased—given by high input power into the nanocavity. Our on-a-chip nanocavities are stable both mechanically and thermally, via the excitation block. However, our current coupling technique using the 100× microscope objective to couple light in and out, makes the position of the piezos very critical and requires a high input power due to losses caused by the grating couplers. It also hinders us from an extra control on the nanoparticle-nanocavity distance with the piezos. Furtheremore, a frontal approach with thermally resistant nanocavities would allow us to bring both elements closer to each other without destroying the nanocavity. Moreover, we could exploit standing waves from the reflection of the trapping laser on the nanobeam's surface. Also, with the flexibility and design of two detection spots within a single nanobeam, we could also read out the dynamics of two levitated objects and create more complex and versatile optomechanical systems.

Chapter 8

Conclusions and outlook

In this thesis, I have described the work completed with two on-a-chip levitodynamics experiments. On one hand, we have shown and discussed how a planar Paul trap is designed, built, and used to levitate charged nanoparticles. On the other hand, we have also designed, fabricated, and tested a suspended 1D photonic crystal nanocavity fabricated on a silicon nitride membrane to study near-field levitodynamics. Here, we summarize, collect, and itemize the main conclusions of our work and also include a brief outlook.

Planar Paul Traps (PPT)

Design and optimization: We have optimized the design of a PPT to improve the trapping confinement by making the trapping potential 10× deeper compared to previous works [87]. We have also compared the confinement of the original design to the optimized one. It is one of the first contributions of a PPT used to levitate nanoparticles.

PPT for levitation and manipulation: We have used a PPT for 3D manipulation of single charged 100 nm polystyrene nanoparticles under ambient conditions. The trap enables stable particle confinement of ~ 4 μm along each axis, it can be rotated throughout the full 360°, and we can also adjust the trapping distance of the nanoparticle to the surface of the PPT. Furthermore, if we increased the optical power of the laser source used for detecting the nanoparticle's motion, we observed that optical forces become prominent and affect the dynamics of the trapped specimen.

Thermal behavior of nanocavities

Cavity's resonance shift: We have studied and characterized the thermal behavior of the nanocavity's resonance for different heating sources: the trapping beam, the intra-cavity light, an external laser beam, and a heater. When the nanocavity heats up, we've observed a predominant blue-shift of -0.15 ± 0.05 nm/K which we believe is related to a thermo-mechanical effect that deforms the geometry of the nanocavity. This value of temperature sensitivity is comparable to current nanophotonic devices. However, most of them are hybrid systems that require a more complex fabrication whereas our device can be easily integrated in commercially available membranes with standard nanofabriation tools. To our knowledge, this is the first time that these effects are studied in a 1D photonic crystal nanobeam in Si_3N_4. Our on-a-chip system also displays bistability and self-induced oscillations in its output transmission, providing the key behavior for optical integrated circuits as well as enabling the integration of a temperature or pressure nanosensor, expanding and opening new facets and applications for on-a-chip levitodynamics.

Bistability: We have observed bistability in the nanocavity's transmission in two ways. One signature of bistability is the deformation of the resonance's Lorentzian shape into a triangular resonance profile for high input powers into the cavity. For our nanocavities, it is due to the thermo-optic effect, and we have observed it by performing wavelength scans for increasing input powers. This allowed us to find a bistability threshold input power of 3 μW for a pressure of 0.5 mbar. In other works, one of the main goals is to achieve bistable devices with the lowest power threshold possible. Currently, these values sit at 1.6 μW [68]. Another way to observe bistability is by measuring the hysteretic response in the nanocavity's transmission. To do so, we performed power scans for a fixed wavelength and observed how both the "on" state and the "off" state in the cavity's transmission depend on the detuning from resonance and on the power injected into the nanocavity. Both variables determine the amount of energy delivered into the cavity, and therefore, how much its temperature increases. We've reached the "on" state of the hysteresis cycle at 0.5 mbar with a power of 11 μW coupled into the waveguide. We've also found that the value of the detuning $\delta\lambda$ between the excitation source and the cavity's resonance is not fully reliable because the starting cavity's resonance λ_{res} varies between scans. This could be solved by performing faster scans, a possibility that is currently unavailable due to the current lim-

itations of our excitation laser. Also, we've observed that the heating performance of the dielectric mode and air mode nanocavities are very similar.

Self-induced oscillations: We have experimentally demonstrated self-induced oscillations in the nanocavity's output transmission—driven by a slow thermo-mechanical effect and a fast thermo-optic effect—at a pressure of 0.5 mbar with a minimum injection power of 29 μW at the input coupler of the structure, resulting in approximately ~ 4 μW coupled into the waveguide. We also observed a dependence on the length of the period of the oscillations with both the detuning from resonance and the injection power. Furthermore, for low enough input powers we showed chaotic behavior in the nanocavity's output.

Levitodynamics with photonic crystal nanocavities

Preliminary near-field experiments: As proof-of-principle experiments, we've detected the dynamics of a levitated nanoparticle in the overdamped regime through a fiber tip, and also through a tapered fiber at a pressure of 4 mbar. With these preliminary tests, we developed the tools and expertise to manipulate levitated nanoparticles and we proved a near-field interaction between the particle and a photonic structure.

Design, simulation and fabrication: We have designed a 1D photonic crystal nanocavity that includes grating couplers to couple light into the nanocavity. We carried out a preliminary simulation in Lumerical to determine the design, followed by a COMSOL simulation to further understand the nanocavity's characteristics. We have worked with two designs: one that confines the electric field in the dielectric (dielectric mode), and the other in air (air mode). We were able to further tune the nanocavity's dielectric mode design to obtain the second order mode of the cavity within the tunability of our laser, where the field intensity shows two maxima on the nanobeam. The nanocavities have been fabricated on a silicon nitride membrane using nanofabrication tools and procedures.

Particle's detection: We've worked with two types of detection, balanced homodyne and direct detection, to measure the nanoparticle's dynamics through a suspended nanocavity in silicon nitride. We have developed a procedure to stabilize the nanocavity's transmission—via the excitation block—and carry out the experiment.

Homodyne detection: In the case of the balanced homodyne detection, we were limited in sensitivity by the detuning given by the thermal self-lock, also referred to as excitation block. Additionally, the nanocavity's resonance shifts further as we approach the nanoparticle with the 1064 nm trapping laser to it because of heating. This also reduces the nanocavity's output transmission. We've detected the nanoparticle's dynamics through the fundamental mode nanocavity as well as with the second mode nanocavity (both dielectric mode designs).

Direct detection: In this detection scheme, the wavelength tunability of the laser used gave us more flexibility to optimize the nanocavities transmission and also allowed us to obtain a higher signal to noise ratio. We detected the nanoparticle's motion along its three directions of oscillation.

Results and limitations: We found that both homodyne and direct detection schemes are limited by the thermo-optic deformation of the resonance—increasing the linewidth of the nanocavity—and the excitation block state—which fixes the detuning respect to resonance. For both types of detection schemes, we estimated a $g_0 \sim 2\pi \cdot 1$ Hz along the different axes. We've also detected the nanoparticle's dynamics with two types of dielectric mode nanocavities: one where the fundamental mode is excited, and one where the second mode design is used.

Outlook and future work

As we've discussed throughout this thesis, the trend of aiming for lower masses and dimensions in optomechanics is due to the dependence of the fundamental optomechanical interaction g_0 with the mechanical oscillator's mass $\propto 1/m$ and the cavity's mode volume $\propto 1/V_c$. Increasing g_0 allows us to obtain more information per photon from the oscillator's motion—in our case, an optically trapped particle—and from the forces that act upon it.

Along this dissertation we have also analyzed the current limitations of our approach. Therefore, we identify future improvements to be implemented to exploit the full capabilities of these techniques and devices.

Planar Paul Traps

The main motivations to work with a Planar Paul Trap (PPT) are to levitate objects that would otherwise burn in optical tweezers, as well as to explore a possible controlled nanoparticle loading mechanism for optical trapping

schemes. For instance, a charged particle could be transferred from the PPT to an optical tweezer and then brought close to a photonic crystal nanocavity, like the one we've presented on-a-chip in this work. This integrated and adaptable system could provide a tool to load nanoparticles in vacuum for contamination-sensitive levitodynamical experiments. Currently, the most common particle loading method consists in the use of nebulizers, mechanism which forces us to open the vacuum chamber each time one needs to load a particle and also disperses a mist of particles everywhere. To achieve a clean loading into an optical trap, one needs a geometry with optical access, such as the planar geometry of the proposed PPT. Also, the nanoparticle's charge could be a useful handle when approaching, for example, a PhC nanocavity with a certain voltage difference, such that we can attract or repel the nanoparticle to the nanocavity's surface. In summary, a PPT can be an economical and useful trapping tool for charged nano-objects for optical interrogation, manipulation in four different directions: x, y, z, plus rotation, as well as levitation over long periods of time.

Photonic crystal nanocavities for levitodynamics

As soon as we input light at the resonant wavelength into the nanocavity, the circulating radiation within gives rise to a temperature increase. This triggers interesting behaviors in transmission, such as bistability and self-induced oscillations, which are driven by thermo-optical and thermo-mechanical effects. Both bistability and self-induced oscillations are the main building blocks to develop photonic and all-optical circuits, allowing for more complex integrated photonic platforms. In this dissertation we have also seen that the nanocavity is very sensitive to variations in temperature. Hence, we believe it could perform well as a pressure or temperature sensor: either through the variation of resonance with temperature, the bistability power threshold, or by an analysis of the self-induced oscillations.

Recent works [120] show a 1D Si_3N_4 photonic crystal nanobeam "glued" onto an optical fiber tip with an optomechanical coupling $g_0 \approx 10$ kHz, which is three orders of magnitude larger than for macro-cavities. In this work [120], the authors claim the system should improve if mounted in an on-a-chip device: both for thermal dissipation and mechanical support. In their experiment the input power, and therefore intra-cavity photon number, is limited by thermo-optical effects too [120].

Our experiment is very similar to the one described in [120], and already on-a-chip. However, our g_0 is lower than we have estimated with simulations. We believe that we need to bring the nanoparticle closer to the nanocavity's near-field, as well as avoid the thermo-optic distortion—

the nanocavity's linewidth increases—given by high input powers into the nanocavity. Our on-a-chip nanocavities are stable both mechanically and thermally, via the excitation block. However, our current coupling technique using the 100× microscope objective to couple light in and out, requires a high input power, due to losses caused by the grating couplers, and a stable position of the piezos in time. This coupling technique also eliminates the possibility to know the nanoparticle-nanocavity distance with the piezos. A different and more efficient coupling mechanism could help reduce the high input powers, reducing thermo-optical effects. Instead of approaching the nanoparticle from the side, we could approach from the front. Thermally resistant nanocavities would allow us to bring the nanoparticle as close as needed, exploiting standing waves from the trapping beam's reflection on the nanobeam's surface. Also, with the flexibility and design of two detection spots within a single nanobeam, we open the possibility to read out the dynamics of two levitated objects and provide a more complex and versatile optomechanical platform.

Declaration of contributions

In this section, I describe the different contributions of both myself and those involved in the work related with my PhD thesis.

Romain Quidant supervised all the progress of this project from the earliest states until its completion.

Planar Paul Traps (PPT)

I partially built the setup, took and analyzed all the data shown. In this project, I was under the supervision of Johann Berthelot, who designed the setup and trained me in fabrication and in building optical setups. Raúl A. Rica helped with the Paul trap calibration method.

Photonic crystal (PhC) cavity design and fabrication

The initial nanocavity design was proposed by Marcos López from Prof. Chang's group at ICFO. He also provided a simulation on the optomechanical performance of the nanocavity. Alexander Cuadrado, from Universidad Complutense de Madrid, helped us optimize the design in COMSOL. Alexander also performed a thermal simulation of the nanocavity. Jordi Gomis-Bresco from ICN2 provided the air-mode nanocavity design and taught us how to simulate our own PhC cavities in COMSOL.

Mikael Svedendahl, former group member, taught me the main fabrication process for Si_3N_4 membranes. I performed all the fabrication of the nanocavities, as well as improved the fabrication protocol. I optically characterized the nanocavities to make sure they were compatible with our laser source. Also, during the months where ICFO's RIE machine was unavailable, I continued with the fabrication by arranging visits to IMDEA nano in Madrid.

Pre-cavity experiments

I fabricated all fiber tips in the clean room. I took and analyzed all fiber tip-related measurements.

The nanofibers were provided by the Takeuchi lab from Tokyo, Japan thanks to Andreas W. Schell. I took and analyzed the nanotaper fiber's measurements alongside with Vincenzo D'Ambrosio and Andreas. With the help of Johann Osmond, ICFO clean room technician, I made trials to draw a PhC cavity on the nanofibers.

I ordered items and elements for the experiment and mounted the optical setup—including lasers and the vacuum equipment—with the supervision and help of Vincenzo and Andreas.

Nanocavity-related experiments

Andreas and I designed the input and output coupling of light into the nanocavities. I mounted this part of the setup with Piergiacomo Z.G. Fonseca, who supervised the last two years of my PhD. I set up the spectral characterization part of the optical system to characterize the nanocavities. Piergiacomo designed and mounted the balanced-homodyne detection scheme.

Piergiacomo and I took all measurements for the thermal characterization. Jan Gieseler helped us in the design of the experiment with the heater. Gerard P. Conangla and I automatized laser scans with a program in python. I analyzed all the measurements shown in this dissertation.

Piergiacomo and I took all the nanoparticle near-field detection experiments together. I analyzed all the measurements shown here. Jan helped us with the calibration method for the nanocavity's signal and the calculation of g_0.

Appendix A

Nanocavity's optical damage threshold

One of our experimental limitations is that the nanocavities burn at a certain optical power if we focus the 1064 nm trapping light on them at a pressure of 0.5 mbar (see Fig. A.1). This is one of the reasons why we approach the nanoparticle to the nanocavity's near-field from the side.

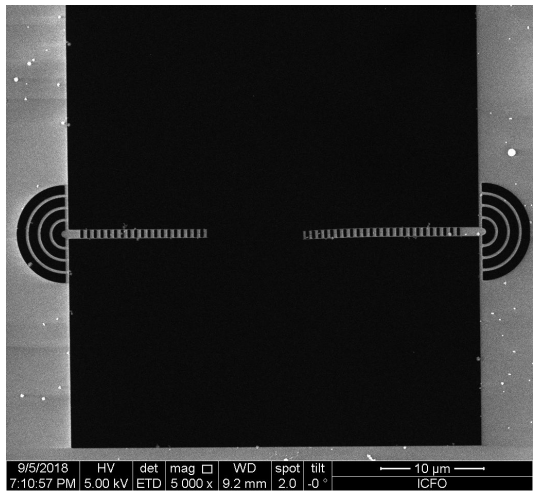

Figure A.1: SEM image of an optically broken nanobeam. This image is an example of a nanocavity with resist residues, most likely due to crusting during the RIE process. Also, the sample has silica nanoparticles deposited on its surface.

To find the power threshold at which the nanocavity's burn, we placed the nanocavities at 0.5 mbar and focused the 1064 nm trapping beam down

to a diameter of $\approx 2\,\mu$m on the center of the nanocavity at a low optical power. Then, we increased the laser's power until we saw the nanocavity's degrade with a CMOS camera, which allows us to image the focal plane of the 100× objective where the nanocavities are located.

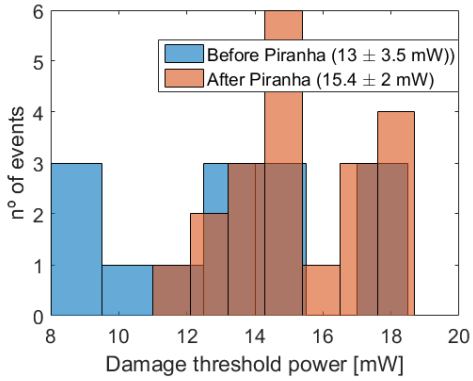

Figure A.2: Histogram of burnt nanocavities with a focused 1064 nm laser beam at the center of the nanocavity. We show the results for a sample before and after a piranha clean.

In Fig. A.2, we show the powers at which the nanocavities were burnt. We compared these with nanocavities cleaned with 8' of piranha solution[1] (4:1) to see if this would vary the threshold power. However, the result obtained for before (13 ± 3.5 mW) and after cleaning (15.4 ± 2 mW) was similar; the cleaning process did not provide a notable change.

Since the absorption of our silicon nitride membranes is two times less for 1550 nm than for 1064 nm[2], we decided to replace the 1064 nm laser for a 1550 nm one (Keopsys CEFL-KILO), while keeping the same optical scheme. In this case we didn't perform a piranha clean.

[1] A piranha solution is a mixture of sulfuric acid and hydrogen peroxide (usually at 30%). It is used to clean organic residues from substrates.

[2] Values of the imaginary part of the index of refraction provided by Norcada: $k_{\lambda=1064\text{ nm}} = 0.001$ and $k_{\lambda=1550\text{ nm}} = 0.0005$.

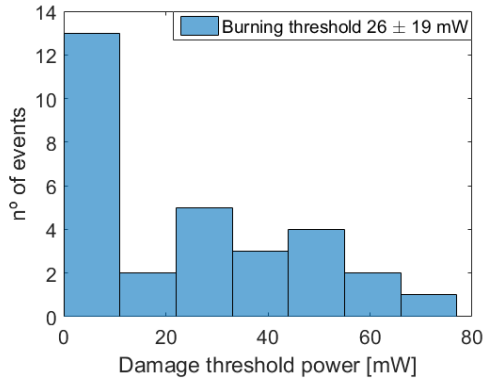

Figure A.3: Histogram of burnt nanocavities with a focused 1550 nm laser beam at the center of the nanocavity.

The maximum amount of power we could focus on the nanocavity was limited to 90 mW. The size of the beam should be roughly the same as the one for 1064 nm since we used the same optics. In Fig. A.3, we show the number of nanocavities that were burnt for each power. Nevertheless, for the 1550 nm laser we observed no burning for 4 out of the 34 nanocavities we tested. This hints that the cleanliness of the nanocavities could play an important role to fix the damage threshold of the device. We observed a large number of cavities burn at lower powers for 1550 nm light. However, as expected, the burning threshold for the 1550 nm laser on average is higher (26 ± 19 mW) than for the 1064 nm laser (13 ± 3.5 mW).

Appendix B

Bistabiliy measurements for air mode nanocavity

As a comparison, we repeated the same bistability experiments and analysis from section 6.4 for the air mode nanocavity. In Fig. B.1, we observe the nanocavitiy's resonance become thermo-optically distorted for higher input powers, both for a pressure of 10 mbar and 0.5 mbar. In this case, the bistability power threshold of the light coupled into the waveguide lies between 8-12 μW for a pressure of 10 mbar, and at 3.6 μW for 0.5 mbar. This result is very similar to the dielectric mode cavity.

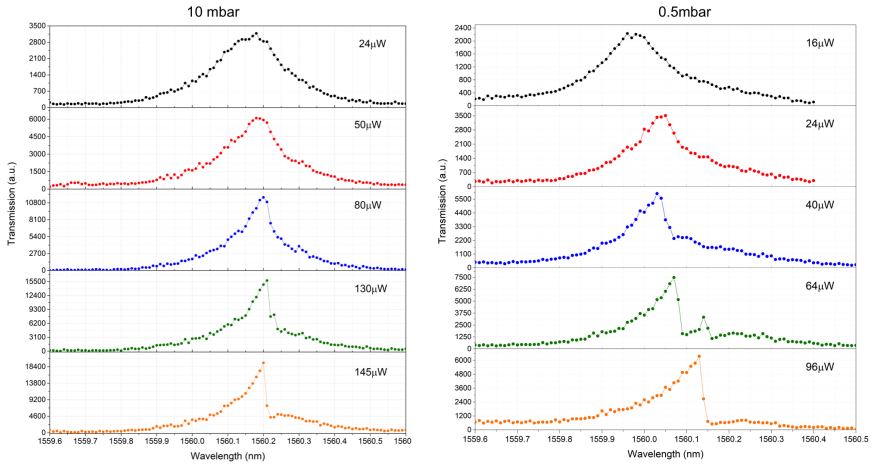

Figure B.1: Wavelength scans for different input powers for air mode cavity. Left to right: scans performed at 10 mbar, and 0.5 mbar. The power in the legend indicates the power that is in front of the input coupler, $\sim$ 15% of this power is actually injected into the waveguide.

We also performed power scans for different excitation wavelengths (see Fig. B.1). We observe a similar outcome compared to the dielectric nanocavity. In Fig. B.1, considering our $\sim 15\%$ coupling efficiency into the waveguide, we observe that the lowest P_{up} is ~ 90 μW and $P_{\text{down}} \sim 75$ μW is very similar for all the hysteresis loops shown, which correspond to a P_{in} of 600 μW and 500 μW in Fig. B.2, respectively. Just like in the case of the dielectric mode nanocavity, $|\delta\lambda| \gtrsim 0.17$ nm is not true: we observe the hysteresis cycle for $|\delta\lambda|$ smaller than 0.17 nm. We believe this is due a difference in λ_{res} at the start of each scan, which is also why we didn't measure the linear behavior for the blue-detuned wavelength. However, we can observe the linear dependency between P_{in} and P_{out} clearly for $\delta\lambda = -0.5$ nm in Fig. B.2.

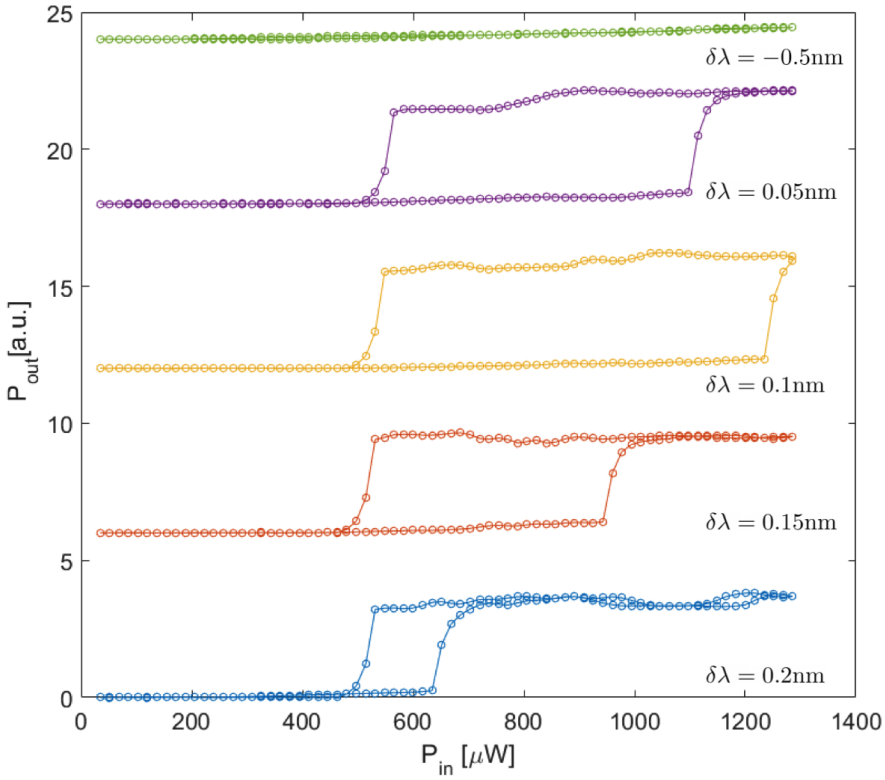

Figure B.2: Power scans for different excitation wavelengths λ_{in} performed at 0.5 mbar for an air mode cavity. Each scan is separated by a fixed value for displaying purposes. We define $\delta\lambda = \lambda_{\text{res}} - \lambda_{\text{L}}$. P_{in} indicates the power that is in front of the input coupler, ~ 15 % of this power is actually injected into the waveguide.

When compared to the results of section 6.4.2, we see that all detunings are positive for the nanocavities with a hysteretic response. This is most likely due to the inaccuracy in our estimation for $\delta\lambda$.

Appendix C

MATLAB code to draw nanocavities and create an EBL file in .asc

The code we use to draw the grating couplers, waveguide and photonic crystal nanocavities can be found in:

https://github.com/irenealda/ebl_nanocavity_drawing.

It must be executed in the following order:

1. Draw grating couplers and waveguide.
2. Draw 1D Photonic crystal cavity. There is code for both the dielectric mode design and the air mode design.
3. Convert drawing into .asc file.

Bibliography

[1] Johannes Kepler. *Astronomia Nova Aitiologētos, Sev Physica Coelestis, tradita commentariis De Motibvs Stellae Martis, Ex observationibus GV Tychonis Brahe.* Republished 1968, 1609.

[2] Isaac Newton. *Philosophiae naturalis principia mathematica*, volume 1. G. Brookman, 1833, 1687.

[3] James C Maxwell. *A dynamical theory of the electromagnetic field.* Wipf and Stock Publishers, 1996, 1865.

[4] Tongcang Li, Simon Kheifets, and Mark G Raizen. Millikelvin cooling of an optically trapped microsphere in vacuum. *Nature Physics*, 7(7):527–530, 2011.

[5] Jan Gieseler, Bradley Deutsch, Romain Quidant, and Lukas Novotny. Subkelvin parametric feedback cooling of a laser-trapped nanoparticle. *Physical Review Letters*, 109(10):103603, 2012.

[6] Erik Hebestreit, Martin Frimmer, René Reimann, and Lukas Novotny. Sensing static forces with free-falling nanoparticles. *Physical Review Letters*, 121(6):063602, 2018.

[7] Arthur Ashkin. Acceleration and trapping of particles by radiation pressure. *Physical Review Letters*, 24(4):156, 1970.

[8] Jeffrey R Moffitt, Yann R Chemla, Steven B Smith, and Carlos Bustamante. Recent advances in optical tweezers. *Annu. Rev. Biochem.*, 77:205–228, 2008.

[9] DE Chang, Jeffrey Douglas Thompson, H Park, V Vuletić, AS Zibrov, P Zoller, and MD Lukin. Trapping and manipulation of isolated atoms using nanoscale plasmonic structures. *Physical Review Letters*, 103(12):123004, 2009.

[10] Andreas Reiserer, Christian Nölleke, Stephan Ritter, and Gerhard Rempe. Ground-state cooling of a single atom at the center of an optical cavity. *Physical Review Letters*, 110(22):223003, 2013.

[11] Haitao Li, Dejian Zhou, Helena Browne, and David Klenerman. Evidence for resonance optical trapping of individual fluorophore-labeled antibodies using single molecule fluorescence spectroscopy. *Journal of the American Chemical Society*, 128(17):5711–5717, 2006.

[12] Bason E Clancy, William M Behnke-Parks, Johan OL Andreasson, Steven S Rosenfeld, and Steven M Block. A universal pathway for kinesin stepping. *Nature structural & molecular biology*, 18(9):1020, 2011.

[13] Jin-Der Wen, Laura Lancaster, Courtney Hodges, Ana-Carolina Zeri, Shige H Yoshimura, Harry F Noller, Carlos Bustamante, and Ignacio Tinoco. Following translation by single ribosomes one codon at a time. *Nature*, 452(7187):598–603, 2008.

[14] Ciro Cecconi, Elizabeth A Shank, Carlos Bustamante, and Susan Marqusee. Direct observation of the three-state folding of a single protein molecule. *Science*, 309(5743):2057–2060, 2005.

[15] Yasuharu Arai, Ryohei Yasuda, Ken-ichirou Akashi, Yoshie Harada, Hidetake Miyata, Kazuhiko Kinosita, and Hiroyasu Itoh. Tying a molecular knot with optical tweezers. *Nature*, 399(6735):446–448, 1999.

[16] Arthur Ashkin, James M Dziedzic, JE Bjorkholm, and Steven Chu. Observation of a single-beam gradient force optical trap for dielectric particles. *Optics letters*, 11(5):288–290, 1986.

[17] Steven Chu, Leo Hollberg, John E Bjorkholm, Alex Cable, and Arthur Ashkin. Three-dimensional viscous confinement and cooling of atoms by resonance radiation pressure. *Physical Review Letters*, 55(1):48, 1985.

[18] Steven Chu, JE Bjorkholm, A Ashkin, and Alex Cable. Experimental observation of optically trapped atoms. *Physical Review Letters*, 57(3):314, 1986.

[19] K. C. Neuman, G. F. Liou, S. M. Block, and K. Bergman. Characterization of photodamage induced by optical tweezers. In *Lasers and Electro-Optics. CLEO.*, pages 203–204, May 1998.

[20] H. Steinwedel W. Paul. Ein neues massenspektrometer ohne magnetfeld. *Zeitschrift für Naturforschung A*, 8(7):448–450, 1953.

[21] Mathieu L Juan, Maurizio Righini, and Romain Quidant. Plasmon nano-optical tweezers. *Nature Photonics*, 5(6):349–356, 2011.

[22] David Erickson, Xavier Serey, Yih-Fan Chen, and Sudeep Mandal. Nanomanipulation using near field photonics. *Lab on a Chip*, 11(6):995–1009, 2011.

[23] Yuanjie Pang and Reuven Gordon. Optical trapping of a single protein. *Nano letters*, 12(1):402–406, 2011.

[24] Mathieu L Juan, Reuven Gordon, Yuanjie Pang, Fatima Eftekhari, and Romain Quidant. Self-induced back-action optical trapping of dielectric nanoparticles. *Nature Physics*, 5(12):915–919, 2009.

[25] Y. Pang and R. Gordon. Optical trapping of 12 nm dielectric spheres using double-nanoholes in a gold film. *Nano letters*, 11(9):3763–3767, 2011.

[26] Chang Chen, Mathieu L Juan, Yi Li, Guido Maes, Gustaaf Borghs, Pol Van Dorpe, and Romain Quidant. Enhanced optical trapping and arrangement of nano-objects in a plasmonic nanocavity. *Nano letters*, 12(1):125–132, 2011.

[27] J Berthelot, SS Aćimović, ML Juan, MP Kreuzer, J Renger, and R Quidant. Three-dimensional manipulation with scanning near-field optical nanotweezers. *Nature nanotechnology*, 9(4):295–299, 2014.

[28] Francesco Ricci, Marc T Cuairan, Gerard P Conangla, Andreas W Schell, and Romain Quidant. Accurate mass measurement of a levitated nanomechanical resonator for precision force-sensing. *Nano letters*, 19(10):6711–6715, 2019.

[29] Martin Frimmer, Karol Luszcz, Sandra Ferreiro, Vijay Jain, Erik Hebestreit, and Lukas Novotny. Controlling the net charge on a nanoparticle optically levitated in vacuum. *Physical Review A*, 95(6):061801, 2017.

[30] Pau Mestres, Johann Berthelot, Marko Spasenović, Jan Gieseler, Lukas Novotny, and Romain Quidant. Cooling and manipulation of a levitated nanoparticle with an optical fiber trap. *Applied Physics Letters*, 107(15), 2015.

[31] Francesco Ricci, Raúl A Rica, Marko Spasenović, Jan Gieseler, Loïc Rondin, Lukas Novotny, and Romain Quidant. Optically levitated nanoparticle as a model system for stochastic bistable dynamics. *Nature communications*, 8(1):1–7, 2017.

[32] Olivier Arcizet, Vincent Jacques, Alessandro Siria, Philippe Poncharal, Pascal Vincent, and Signe Seidelin. A single nitrogen-vacancy defect coupled to a nanomechanical oscillator. *Nature Physics*, 7(11):879–883, 2011.

[33] Gerard P. Conangla, Andreas W. Schell, Raúl A. Rica, and Romain Quidant. Motion control and optical interrogation of a levitating single nitrogen vacancy in vacuum. *Nano letters*, 2018.

[34] T Delord, L Nicolas, M Bodini, and G Hétet. Diamonds levitating in a paul trap under vacuum: Measurements of laser-induced heating via nv center thermometry. *Applied Physics Letters*, 111(1):013101, 2017.

[35] Gambhir Ranjit, David P. Atherton, Jordan H. Stutz, Mark Cunningham, and Andrew A. Geraci. Attonewton force detection using microspheres in a dual-beam optical trap in high vacuum. *Phys. Rev. A*, 91:051805, May 2015.

[36] Vijay Jain, Jan Gieseler, Clemens Moritz, Christoph Dellago, Romain Quidant, and Lukas Novotny. Direct measurement of photon recoil from a levitated nanoparticle. *Physical Review Letters*, 116(24):243601, 2016.

[37] R. Reimann. Iqlev: Inertial sensing based on quantum enhance levitation systems. private comunication, February 2020.

[38] Oriol Romero-Isart, Anika C Pflanzer, Florian Blaser, Rainer Kaltenbaek, Nikolai Kiesel, Markus Aspelmeyer, and J Ignacio Cirac. Large quantum superpositions and interference of massive nanometer-sized objects. *Physical Review Letters*, 107(2):020405, 2011.

[39] Oriol Romero-Isart, Anika C Pflanzer, Mathieu L Juan, Romain Quidant, Nikolai Kiesel, Markus Aspelmeyer, and J Ignacio Cirac. Optically levitating dielectrics in the quantum regime: Theory and protocols. *Physical Review A*, 83(1):013803, 2011.

[40] Felix Tebbenjohanns, Martin Frimmer, Andrei Militaru, Vijay Jain, and Lukas Novotny. Cold damping of an optically levitated nanoparticle to microkelvin temperatures. *Physical Review Letters*, 122(22):223601, 2019.

[41] Gerard P Conangla, Francesco Ricci, Marc T Cuairan, Andreas W Schell, Nadine Meyer, and Romain Quidant. Optimal feedback cooling of a charged levitated nanoparticle with adaptive control. *Physical Review Letters*, 122(22):223602, 2019.

[42] Felix Tebbenjohanns, Martin Frimmer, Vijay Jain, Dominik Windey, and Lukas Novotny. Motional sideband asymmetry of a nanoparticle optically levitated in free space. *Physical Review Letters*, 124(1):013603, 2020.

[43] PF Barker and MN Shneider. Cavity cooling of an optically trapped nanoparticle. *Physical Review A*, 81(2):023826, 2010.

[44] Peter Asenbaum, Stefan Kuhn, Stefan Nimmrichter, Ugur Sezer, and Markus Arndt. Cavity cooling of free silicon nanoparticles in high vacuum. *Nature communications*, 4(1):1–7, 2013.

[45] Nikolai Kiesel, Florian Blaser, Uroš Delić, David Grass, Rainer Kaltenbaek, and Markus Aspelmeyer. Cavity cooling of an optically levitated submicron particle. *Proceedings of the National Academy of Sciences*, 110(35):14180–14185, 2013.

[46] Markus Aspelmeyer, Tobias J. Kippenberg, and Florian Marquardt. Cavity optomechanics. *Rev. Mod. Phys.*, 2014.

[47] J Millen, PZG Fonseca, T Mavrogordatos, TS Monteiro, and PF Barker. Cavity cooling a single charged levitated nanosphere. *Physical Review Letters*, 114(12):123602, 2015.

[48] PZG Fonseca, EB Aranas, J Millen, TS Monteiro, and PF Barker. Nonlinear dynamics and strong cavity cooling of levitated nanoparticles. *Physical Review Letters*, 117(17):173602, 2016.

[49] Nadine Meyer, Andrés de los Rios Sommer, Pau Mestres, Jan Gieseler, Vijay Jain, Lukas Novotny, and Romain Quidant. Resolved-sideband cooling of a levitated nanoparticle in the presence of laser phase noise. *Physical Review Letters*, 2019.

[50] Dominik Windey, Carlos Gonzalez-Ballestero, Patrick Maurer, Lukas Novotny, Oriol Romero-Isart, and René Reimann. Cavity-based 3d cooling of a levitated nanoparticle via coherent scattering. *Physical Review Letters*, 122(12):123601, 2019.

[51] Uroš Delić, Manuel Reisenbauer, David Grass, Nikolai Kiesel, Vladan Vuletić, and Markus Aspelmeyer. Cavity cooling of a levitated nanosphere by coherent scattering. *Physical Review Letters*, 122(12):123602, 2019.

[52] Uroš Delić, Manuel Reisenbauer, Kahan Dare, David Grass, Vladan Vuletić, Nikolai Kiesel, and Markus Aspelmeyer. Cooling of a levitated nanoparticle to the motional quantum ground state. *Science*, 367(6480):892–895, 2020.

[53] Aaron D O'Connell, Max Hofheinz, Markus Ansmann, Radoslaw C Bialczak, Mike Lenander, Erik Lucero, Matthew Neeley, Daniel Sank, H Wang, Ms Weides, et al. Quantum ground state and single-phonon control of a mechanical resonator. *Nature*, 464(7289):697–703, 2010.

[54] John D Teufel, Tobias Donner, Dale Li, Jennifer W Harlow, MS Allman, Katarina Cicak, Adam J Sirois, Jed D Whittaker, Konrad W Lehnert, and Raymond W Simmonds. Sideband cooling of micromechanical motion to the quantum ground state. *Nature*, 475(7356):359–363, 2011.

[55] Jasper Chan, TP Mayer Alegre, Amir H Safavi-Naeini, Jeff T Hill, Alex Krause, Simon Gröblacher, Markus Aspelmeyer, and Oskar Painter. Laser cooling of a nanomechanical oscillator into its quantum ground state. *Nature*, 478(7367):89–92, 2011.

[56] Oriol Romero-Isart. Quantum superposition of massive objects and collapse models. *Physical Review A*, 84(5):052121, 2011.

[57] TP Purdy, RW Peterson, PL Yu, and CA Regal. Cavity optomechanics with si3n4 membranes at cryogenic temperatures. *New Journal of Physics*, 14(11):115021, 2012.

[58] Albert Schliesser, Rémi Rivière, Georg Anetsberger, Olivier Arcizet, and Tobias J Kippenberg. Resolved-sideband cooling of a micromechanical oscillator. *Nature Physics*, 4(5):415–419, 2008.

[59] J. T. Hill. *Nonlinear optics and wavelength translation via cavity optomechanics*. PhD thesis, Califiornia Institute of Technology, 2013.

[60] Lu Ding, Christophe Baker, Pascale Senellart, Aristide Lemaitre, Sara Ducci, Giuseppe Leo, and Ivan Favero. Wavelength-sized gaas optomechanical resonators with gigahertz frequency. *Applied Physics Letters*, 98(11):113108, 2011.

[61] Tal Carmon and Kerry J Vahala. Modal spectroscopy of optoexcited vibrations of a micron-scale on-chip resonator at greater than 1 ghz frequency. *Physical Review Letters*, 98(12):123901, 2007.

[62] A Naik, O Buu, MD LaHaye, AD Armour, AA Clerk, MP Blencowe, and KC Schwab. Cooling a nanomechanical resonator with quantum back-action. *Nature*, 443(7108):193–196, 2006.

[63] Jordi Gomis-Bresco, Daniel Navarro-Urrios, Mourad Oudich, Said El-Jallal, Amadeu Griol, Daniel Puerto, Emiglio Chavez, Yan Pennec, Bahram Djafari-Rouhani, Franscesca Alzina, et al. A one-dimensional optomechanical crystal with a complete phononic band gap. *Nature communications*, 5(1):1–6, 2014.

[64] Hiroki Takahashi, Alex Wilson, Andrew Riley-Watson, Fedja Oručević, Nicolas Seymour-Smith, Matthias Keller, and Wolfgang Lange. An integrated fiber trap for single-ion photonics. *New Journal of Physics*, 15(5):053011, 2013.

[65] S-P Yu, JD Hood, JA Muniz, MJ Martin, Richard Norte, C-L Hung, Seán M Meenehan, Justin D Cohen, Oskar Painter, and HJ Kimble. Nanowire photonic crystal waveguides for single-atom trapping and strong light-matter interactions. *Applied Physics Letters*, 104(11):111103, 2014.

[66] Tal Carmon, Lan Yang, and Kerry J Vahala. Dynamical thermal behavior and thermal self-stability of microcavities. *Optics express*, 12(20):4742–4750, 2004.

[67] Xuefeng Jiang and Lan Yang. Optothermal dynamics in whispering-gallery microresonators. *Light: Science & Applications*, 9(1):1–15, 2020.

[68] Laurent-Daniel Haret, Takasumi Tanabe, Eiichi Kuramochi, and Masaya Notomi. Extremely low power optical bistability in silicon demonstrated using 1d photonic crystal nanocavity. *Optics express*, 17(23):21108–21117, 2009.

[69] Masaya Notomi, Akihiko Shinya, Satoshi Mitsugi, Goh Kira, Eiichi Kuramochi, and Takasumi Tanabe. Optical bistable switching action of si high-q photonic-crystal nanocavities. *Optics express*, 13(7):2678–2687, 2005.

[70] Raji Shankar, Irfan Bulu, Rick Leijssen, and Marko Lončar. Study of thermally-induced optical bistability and the role of surface treatments in si-based mid-infrared photonic crystal cavities. *Optics express*, 19(24):24828–24837, 2011.

[71] KA Williams, M Trajkovic, V Rustichelli, F Lemaître, HPMM Ambrosius, and XJM Leijtens. High-speed energy-efficient inp photonic integrated circuit transceivers. In *Optical Interconnects XIX*, volume 10924, page 1092411. International Society for Optics and Photonics, 2019.

[72] Alexey E Fomin, Michael L Gorodetsky, Ivan S Grudinin, and Vladimir S Ilchenko. Nonstationary nonlinear effects in optical microspheres. *JOSA B*, 22(2):459–465, 2005.

[73] Thomas J Johnson, Matthew Borselli, and Oskar Painter. Self-induced optical modulation of the transmission through a high-q silicon microdisk resonator. *Optics express*, 14(2):817–831, 2006.

[74] Wolfram HP Pernice, Mo Li, and Hong X Tang. Time-domain measurement of optical transport in silicon micro-ring resonators. *Optics express*, 18(17):18438–18452, 2010.

[75] Daniel Navarro-Urrios, Nestor E Capuj, Jordi Gomis-Bresco, Francesc Alzina, Alessandro Pitanti, Amadeu Griol, Alejandro Martínez, and CM Sotomayor Torres. A self-stabilized coherent phonon source driven by optical forces. *Scientific reports*, 5(1):1–7, 2015.

[76] Maia Brunstein. *Nonlinear Dynamics in III-V Semiconductor Photonic Crystal Nano-cavities*. PhD thesis, Université Paris Sud - Paris XI, 2011.

[77] Maia Brunstein, Alejandro M Yacomotti, Isabel Sagnes, Fabrice Raineri, Laurent Bigot, and Ariel Levenson. Excitability and self-pulsing in a photonic crystal nanocavity. *Physical Review A*, 85(3):031803, 2012.

[78] Masahiro Nomura, Satoshi Iwamoto, Katsuyuki Watanabe, Naoto Kumagai, Yoshiaki Nakata, Satomi Ishida, and Yasuhiko Arakawa. Room temperature continuous-wave lasing in photonic crystal nanocavity. *Optics express*, 14(13):6308–6315, 2006.

[79] Yasutomo Ota, Ryota Katsumi, Katsuyuki Watanabe, Satoshi Iwamoto, and Yasuhiko Arakawa. Topological photonic crystal nanocavity laser. *Communications Physics*, 1(1):1–8, 2018.

[80] Alexander Gondarenko, Jacob S Levy, and Michal Lipson. High confinement micron-scale silicon nitride high q ring resonator. *Optics express*, 17(14):11366–11370, 2009.

[81] Quirin P Unterreithmeier, Thomas Faust, and Jörg P Kotthaus. Damping of nanomechanical resonators. *Physical Review Letters*, 105(2):027205, 2010.

[82] DTH Tan, K Ikeda, PC Sun, and Y Fainman. Group velocity dispersion and self phase modulation in silicon nitride waveguides. *Applied Physics Letters*, 96(6):061101, 2010.

[83] Christophe Baker, Sebastian Stapfner, David Parrain, Sara Ducci, Giuseppe Leo, Eva M Weig, and Ivan Favero. Optical instability and self-pulsing in silicon nitride whispering gallery resonators. *Optics express*, 20(27):29076–29089, 2012.

[84] John Chiaverini, R Brad Blakestad, Joe Britton, John D Jost, Chris Langer, Dietrich Leibfried, Roee Ozeri, and David J Wineland. Surface-electrode architecture for ion-trap quantum information processing. *Quantum Information and Computation*, 5(6):419–439, 2005.

[85] Signe Seidelin, John Chiaverini, Rainer Reichle, John J Bollinger, Didi Leibfried, Joe Britton, JH Wesenberg, RB Blakestad, RJ Epstein, DB Hume, et al. Microfabricated surface-electrode ion trap for scalable quantum information processing. *Physical Review Letters*, 96(25):253003, 2006.

[86] Muir Kumph, Philip Holz, Kirsten Langer, Michael Niedermayr, Michael Brownnutt, and Rainer Blatt. Operation of a planar-electrode ion trap array with adjustable rf electrodes. *New Journal of Physics*, 18:023020, 2016.

[87] Tony Hyun Kim, Peter F. Herskind, Taehyun Kim, Jungsang Kim, and Isaac L. Chuang. Surface-electrode point paul trap. *Physical Review A*, 82(4):043412, 2010.

[88] Muir Kumph, Michael Brownnutt, and Rainer Blatt. Two-dimensional arrays of radio-frequency ion traps with addressable interactions. *New Journal of Physics*, 13(7):073043, 2011.

[89] Utako Tanaka, Kensuke Suzuki, Yuki Ibaraki, and Shinji Urabe. Design of a surface electrode trap for parallel ion strings. *Journal of Physics B: Atomic, Molecular and Optical Physics*, 47:035301, January 2014.

[90] Mark Maurice, Curtis Allen, Dylan Green, Andrew Farr, Timothy Burke, Russell Hilleke, and Robert Clark. Experimental demonstration of a surface-electrode multipole ion trap. *Journal of Applied Physics*, 118(7):074903, 2015.

[91] Irene Alda, Johann Berthelot, Raúl A Rica, and Romain Quidant. Trapping and manipulation of individual nanoparticles in a planar paul trap. *Applied Physics Letters*, 109(16):163105, 2016.

[92] Philip H Jones, Onofrio M Maragò, and Giovanni Volpe. *Optical tweezers: Principles and applications*. Cambridge University Press, 2015.

[93] Javier Alda. Laser and gaussian beam propagation and transformation. *Encyclopedia of optical engineering*, 2013:999–1013, 2003.

[94] Lukas Novotny and Bert Hecht. *Principles of nano-optics*. Cambridge university press, 2012.

[95] Rep Kubo. The fluctuation-dissipation theorem. *Reports on progress in physics*, 29(1):255, 1966.

[96] Linda E Reichl. *A modern course in statistical physics*. American Association of Physics Teachers, 1999.

[97] Wolfgang Paul. Electromagnetic traps for charged and neutral particles. *Reviews of Modern Physics*, 62:531–540, Jul 1990.

[98] LD Landau and EM Lifshitz. *Mechanics Pergamon*. 1960.

[99] DJ Berkeland, JD Miller, James C Bergquist, Wayne M Itano, and David J Wineland. Minimization of ion micromotion in a paul trap. *Journal of applied physics*, 83(10):5025–5033, 1998.

[100] John David Jackson. *Classical electrodynamics*. John Wiley & Sons, 2007.

[101] Milton Abramowitz and Irene A Stegun. *Handbook of mathematical functions with formulas, graphs, and mathematical tables*, volume 55. US Government printing office, 1948.

[102] Daniel A. Steck. *Quantum and Atom Optics*. available online at http://steck.us/teaching, 2006.

[103] Hermann A Haus. *Waves and fields in optoelectronics*. Prentice-Hall,, 1984.

[104] George W Ford, John T Lewis, and RF O'connell. Quantum langevin equation. *Physical Review A*, 37(11):4419, 1988.

[105] Piergiacomo Zucconi Galli Fonseca. *Levitated Optomechanics in a hybrid electro-optical Trap*. PhD thesis, University College London, 2017.

[106] John D Joannopoulos, Robert D Meade, and JN Winn. *Photonic Crystals. Molding the Flow of Light*. Princeton University Press, 2008.

[107] M. Tinkham. *Group Theory and Quantum Mechanics*. Dover Publications, 2003.

[108] Charles Kittel. *Introduction to Solid State Physics*. Wiley John and Sons, 2004.

[109] Kater W Murch, Kevin L Moore, Subhadeep Gupta, and Dan M Stamper-Kurn. Observation of quantum-measurement backaction with an ultracold atomic gas. *Nature Physics*, 4(7):561–564, 2008.

[110] Seán Micheal Meenehan. *Cavity Optomechanics at Millikelvin Temperatures*. PhD thesis, California Institute of Technology, 2015.

[111] Takao Aoki, Barak Dayan, Elizabeth Wilcut, Warwick P Bowen, A Scott Parkins, TJ Kippenberg, KJ Vahala, and HJ Kimble. Observation of strong coupling between one atom and a monolithic microresonator. *Nature*, 443(7112):671–674, 2006.

[112] KP Nayak, PN Melentiev, M Morinaga, Fam Le Kien, VI Balykin, and K Hakuta. Optical nanofiber as an efficient tool for manipulating and probing atomic fluorescence. *Optics Express*, 15(9):5431–5438, 2007.

[113] E Vetsch, D Reitz, G Sagué, R Schmidt, ST Dawkins, and A Rauschenbeutel. Optical interface created by laser-cooled atoms trapped in the evanescent field surrounding an optical nanofiber. *Physical Review Letters*, 104(20):203603, 2010.

[114] Jeffrey Douglas Thompson, TG Tiecke, Nathalie P de Leon, J Feist, AV Akimov, M Gullans, Alexander S Zibrov, V Vuletić, and Mikhail D Lukin. Coupling a single trapped atom to a nanoscale optical cavity. *Science*, 340(6137):1202–1205, 2013.

[115] Jonathan D Hood, Akihisa Goban, Ana Asenjo-Garcia, Mingwu Lu, Su-Peng Yu, Darrick E Chang, and HJ Kimble. Atom–atom interactions around the band edge of a photonic crystal waveguide. *Proceedings of the National Academy of Sciences*, 113(38):10507–10512, 2016.

[116] Lukas Neumeier, Romain Quidant, and Darrick E Chang. Self-induced back-action optical trapping in nanophotonic systems. *New Journal of Physics*, 17(12):123008, 2015.

[117] A. H. Safavi-Naeni. *Quantum optomechanics with silicon nanostructures*. PhD thesis, California Institute of Technology, 2013.

[118] Sylvain Combrié, Alfredo De Rossi, Quynh Vy Tran, and Henri Benisty. Gaas photonic crystal cavity with ultrahigh q: microwatt nonlinearity at 1.55 μm. *Optics letters*, 33(16):1908–1910, 2008.

[119] Hiroshi Sekoguchi, Yasushi Takahashi, Takashi Asano, and Susumu Noda. Photonic crystal nanocavity with a q-factor of˜ 9 million. *Optics express*, 22(1):916–924, 2014.

[120] Lorenzo Magrini, Richard A Norte, Ralf Riedinger, Igor Marinković, David Grass, Uroš Delić, Simon Gröblacher, Sungkun Hong, and Markus Aspelmeyer. Near-field coupling of a levitated nanoparticle to a photonic crystal cavity. *Optica*, 5(12):1597–1602, 2018.

[121] Jan Gieseler. *Dynamics of optically levitated nanoparticles in high vaccum*. PhD thesis, Universitat Politecnica de Catalunya, 2014.

[122] Victor J Cadarso, Andreu Llobera, Mar Puyol, and Helmut Schift. Integrated photonic nanofences: Combining subwavelength waveguides with an enhanced evanescent field for sensing applications. *ACS nano*, 10(1):778–785, 2016.

[123] Leopold B Felsen. Evanescent waves. *JOSA*, 66(8):751–760, 1976.

[124] Manuel Nieto-Vesperinas. *Scattering and diffraction in physical optics*. World Scientific Publishing Company, 2006.

[125] Satoshi Kawata and T Tani. Optically driven mie particles in an evanescent field along a channeled waveguide. *Optics letters*, 21(21):1768–1770, 1996.

[126] E Centeno and D Felbacq. Optical bistability in finite-size nonlinear bidimensional photonic crystals doped by a microcavity. *Physical Review B*, 62(12):R7683, 2000.

[127] Marin Soljačić, Mihai Ibanescu, Steven G Johnson, Yoel Fink, and John D Joannopoulos. Optimal bistable switching in nonlinear photonic crystals. *Physical Review E*, 66(5):055601, 2002.

[128] Alan L Hodgkin and Andrew F Huxley. A quantitative description of membrane current and its application to conduction and excitation in nerve. *The Journal of physiology*, 117(4):500–544, 1952.

[129] Richard FitzHugh. Impulses and physiological states in theoretical models of nerve membrane. *Biophysical journal*, 1(6):445, 1961.

[130] Jinichi Nagumo, Suguru Arimoto, and Shuji Yoshizawa. An active pulse transmission line simulating nerve axon. *Proceedings of the IRE*, 50(10):2061–2070, 1962.

[131] Francesco Marino, Gustau Catalán, Pedro Sánchez, Salvador Balle, and Oreste Piro. Thermo-optical "canard orbits" and excitable limit cycles. *Physical Review Letters*, 92(7):073901, 2004.

[132] Francesco Marino and Salvador Balle. Excitable optical waves in semiconductor microcavities. *Physical Review Letters*, 94(9):094101, 2005.

[133] KJA Ooi, DKT Ng, T Wang, AKL Chee, SK Ng, Q Wang, LK Ang, AM Agarwal, LC Kimerling, and DTH Tan. Pushing the limits of cmos optical parametric amplifiers with usrn: Si 7 n 3 above the two-photon absorption edge. *Nature communications*, 8(1):1–10, 2017.

[134] Amir Arbabi and Lynford L Goddard. Measurements of the refractive indices and thermo-optic coefficients of si3n4 and siox using microring resonances. *Optics letters*, 38(19):3878–3881, 2013.

[135] Ali W Elshaari, Iman Esmaeil Zadeh, Klaus D Jöns, and Val Zwiller. Thermo-optic characterization of silicon nitride resonators for cryogenic photonic circuits. *IEEE Photonics Journal*, 8(3):1–9, 2016.

[136] Chuen-Lin Tien and Tsai-Wei Lin. Thermal expansion coefficient and thermomechanical properties of sin x thin films prepared by plasma-enhanced chemical vapor deposition. *Applied optics*, 51(30):7229–7235, 2012.

[137] A Szöke, V Daneu, J Goldhar, and NA Kurnit. Bistable optical element and its applications. *Applied Physics Letters*, 15(11):376–379, 1969.

[138] HM Gibbs, SL McCall, and TNC Venkatesan. Differential gain and bistability using a sodium-filled fabry-perot interferometer. *Physical Review Letters*, 36(19):1135, 1976.

[139] H. Gibbs. *Optical Bistability: Controlling Light with Light*. Academic Press, 1985.

[140] M Giudici, C Green, G Giacomelli, U Nespolo, and JR Tredicce. Andronov bifurcation and excitability in semiconductor lasers with optical feedback. *Physical Review E*, 55(6):6414, 1997.

[141] Alejandro M Yacomotti, Paul Monnier, Fabrice Raineri, B Ben Bakir, C Seassal, Rama Raj, and Juan Ariel Levenson. Fast thermo-optical excitability in a two-dimensional photonic crystal. *Physical Review Letters*, 97(14):143904, 2006.

[142] Francesco Pedaci, Zhuangxiong Huang, Maarten Van Oene, Stephane Barland, and Nynke H Dekker. Excitable particles in an optical torque wrench. *Nature Physics*, 7(3):259–264, 2011.

[143] Steven A. Prescott. *Excitability: Types I, II, and III. Encyclopedia of Computational Neuroscience*. Springer New York, 2013.

[144] Stéphane Barland, Oreste Piro, Massimo Giudici, Jorge R Tredicce, and Salvador Balle. Experimental evidence of van der pol–fitzhugh–nagumo dynamics in semiconductor optical amplifiers. *Physical Review E*, 68(3):036209, 2003.

[145] Siddharth Tallur, Suresh Sridaran, and Sunil A Bhave. A monolithic radiation-pressure driven, low phase noise silicon nitride opto-mechanical oscillator. *Optics express*, 19(24):24522–24529, 2011.

[146] Dmitry S Bykov, Pau Mestres, Lorenzo Dania, Lisa Schmöger, and Tracy E Northup. Direct loading of nanoparticles under high vacuum into a paul trap for levitodynamical experiments. *Applied Physics Letters*, 115(3):034101, 2019.

[147] AP VanDevender, Yves Colombe, Jason Amini, D Leibfried, and David J Wineland. Efficient fiber optic detection of trapped ion fluorescence. *Physical Review Letters*, 105(2):023001, 2010.

[148] Simon J Gaskell. Electrospray: principles and practice. *Journal of mass spectrometry*, 32(7):677–688, 1997.

[149] Markus Gregor, Alexander Kuhlicke, and Oliver Benson. Soft-landing and optical characterization of a preselected single fluorescent particle on a tapered optical fiber. *Optics express*, 17(26):24234–24243, 2009.

[150] Janus H Wesenberg. Electrostatics of surface-electrode ion traps. *Physical Review A*, 78(6):063410, 2008.

[151] Gerard P Conangla, Dwight Nwaigwe, Jan Wehr, and Raúl A Rica. Overdamped dynamics of a brownian particle levitated in a paul trap. *arXiv preprint arXiv:1912.11317*, 2019.

[152] Alexander F Izmailov, Stephen Arnold, Stephen Holler, and Allan S Myerson. Microparticle driven by parametric and random forces: Theory and experiment. *Physical Review E*, 52(2):1325, 1995.

[153] William B Whitten, Peter TA Reilly, and J Michael Ramsey. High-pressure ion trap mass spectrometry. *Rapid communications in mass spectrometry*, 18(15):1749–1752, 2004.

[154] Simon F Tolić-Nørrelykke, Erik Schäffer, Jonathon Howard, Francesco S Pavone, Frank Jülicher, and Henrik Flyvbjerg. Calibration of optical tweezers with positional detection in the back focal plane. *Review of scientific instruments*, 77(10):103101, 2006.

[155] G. P. Conangla. In preparation. 2020.

[156] GI Stegeman, RF Wallis, and AA Maradudin. Excitation of surface polaritons by end-fire coupling. *Optics letters*, 8(7):386–388, 1983.

[157] DJ Ripin and L Goldberg. High efficiency side-coupling of light into optical fibres using imbedded v-grooves. *Electronics Letters*, 31(25):2204–2205, 1995.

[158] Minhao Pu, Liu Liu, Haiyan Ou, Kresten Yvind, and Jørn M Hvam. Ultra-low-loss inverted taper coupler for silicon-on-insulator ridge waveguide. *Optics Communications*, 283(19):3678–3682, 2010.

[159] Dror Sarid, Paul J Cressman, and Robert L Holman. High-efficiency prism coupler for optical waveguides. *Applied Physics Letters*, 33(6):514–515, 1978.

[160] Andrei Faraon, Ilya Fushman, Dirk Englund, Nick Stoltz, Pierre Petroff, and Jelena Vučković. Dipole induced transparency in waveguide coupled photonic crystal cavities. *Optics express*, 16(16):12154–12162, 2008.

[161] Yunpeng Zhu, Jie Wang, Weiqiang Xie, Bin Tian, Yanlu Li, Edouard Brainis, Yuqing Jiao, and Dries Van Thourhout. Ultra-compact silicon nitride grating coupler for microscopy systems. *Optics express*, 25(26):33297–33304, 2017.

[162] K. R. Harper. Theory, design, and fabrication of diffractive grating coupler for slab waveguide. Master's thesis, Bringham Young University, 2003.

[163] Carlo Barth, Janik Wolters, Andreas W Schell, Jürgen Probst, Max Schoengen, Bernd Löchel, Stefan Kowarik, and Oliver Benson. Miniaturized bragg-grating couplers for sin-photonic crystal slabs. *Optics express*, 23(8):9803–9811, 2015.

[164] Frederik Van Laere, Günther Roelkens, Melanie Ayre, Jonathan Schrauwen, Dirk Taillaert, Dries Van Thourhout, Thomas F Krauss, and Roel Baets. Compact and highly efficient grating couplers between optical fiber and nanophotonic waveguides. *Journal of lightwave technology*, 25(1):151–156, 2007.

[165] A. Cuadrado. Comsol simulations. Private comunication, February 2020.

[166] Olivier Arcizet. *Mesure optique ultrasensible et refroidissement par pression de radiation d´ un micro-résonateur mécanique*. PhD thesis, 2006.

[167] Alexander Cuadrado, Javier Alda, and Francisco J Gonzalez. Distributed bolometric effect in optical antennas and resonant structures. *Journal of Nanophotonics*, 6(1):063512, 2012.

[168] Yuguang Zhang, Penghao Liu, Senlin Zhang, Weixi Liu, Jingye Chen, and Yaocheng Shi. High sensitivity temperature sensor based on cascaded silicon photonic crystal nanobeam cavities. *Optics express*, 24(20):23037–23043, 2016.

[169] C-H Dong, L He, Y-F Xiao, VR Gaddam, SK Ozdemir, Z-F Han, G-C Guo, and L Yang. Fabrication of high-q polydimethylsiloxane optical microspheres for thermal sensing. *Applied Physics letters*, 94(23):231119, 2009.

[170] Linhua Xu, Xuefeng Jiang, Guangming Zhao, Ding Ma, Hu Tao, Zhiwen Liu, Fiorenzo G Omenetto, and Lan Yang. High-q silk fibroin whispering gallery microresonator. *Optics express*, 24(18):20825–20830, 2016.

[171] Tal Carmon, Tobias J Kippenberg, Lan Yang, Hosein Rokhsari, Sean Spillane, and Kerry J Vahala. Feedback control of ultra-high-q microcavities: application to micro-raman lasers and micro-parametric oscillators. *Optics express*, 13(9):3558–3566, 2005.

[172] TG McRae, Kwam H Lee, M McGovern, D Gwyther, and WP Bowen. Thermo-optic locking of a semiconductor laser to a microcavity resonance. *Optics express*, 17(24):21977–21985, 2009.

[173] Ivan Grudinin, Hansuek Lee, Tong Chen, and Kerry Vahala. Compensation of thermal nonlinearity effect in optical resonators. *Optics express*, 19(8):7365–7372, 2011.

[174] Hubert Pascal Seigneur, Matthew Weed, Michael Niklaus Leuenberger, and Winston Vaughan Schoenfeld. Controlled on-chip single-photon transfer using photonic crystal coupled-cavity waveguides. *Advances in OptoElectronics*, 2011, 2011.

[175] Mohammad Soltani, Qing Li, Siva Yegnanarayanan, and Ali Adibi. Improvement of thermal properties of ultra-high q silicon microdisk resonators. *Optics express*, 15(25):17305–17312, 2007.

[176] E. W. Weisstein. Pearson mode skewness. MathWorld–A Wolfram Web Resource.

[177] Rozenn Diehl, Erik Hebestreit, René Reimann, Felix Tebbenjohanns, Martin Frimmer, and Lukas Novotny. Optical levitation and feedback cooling of a nanoparticle at subwavelength distances from a membrane. *Physical Review A*, 98(1):013851, 2018.

[178] ML Gorodetksy, Albert Schliesser, Georg Anetsberger, Samuel Deleglise, and Tobias J Kippenberg. Determination of the vacuum optomechanical coupling rate using frequency noise calibration. *Optics express*, 18(22):23236–23246, 2010.